Memoria de Tesis
presentada en la Universidad de Granada
para obtener el grado de Doctor en Física y Matemáticas

The Nature of the Radio Emission from Stellar Winds in Wolf-Rayet Binary Stars

Gabriela Montes

Directores de tesis:
Miguel Angel Pérez Torres (Instituto de Astrofísica de Andalucía, CSIC)
Ricardo F. González Domínguez (Centro de Radioastronomía y Astrofísica, UNAM)
Antonio Alberdi Odriozola (Instituto de Astrofísica de Andalucía, CSIC)

Instituto de Astrofísica de Andalucía (CSIC)
Granada, España
Octubre 2011

Editor: Editorial de la Universidad de Granada
Autor: Gabriela Montes
D.L.: GR 2324-2012
ISBN: 978-84-9028-212-0

To my family

Soy hombre: duro poco
y es enorme la noche.
Pero miro hacia arriba:
las estrellas escriben.
Sin entender comprendo:
también soy escritura
y en este mismo instante
alguien me deletrea.

Octavio Paz
Hermandad

Agradecimientos

Esto se torna complicado, así que comenzaré agradeciendo a los principales responsables, y primeros colaboradores del trabajo que aquí presento. Agradezco a Antxon, Miguel y Ricardo, mis directores, por toda la ayuda y todo lo que me han permitido aprender de ellos, pero en especial por todo el apoyo y la confianza que me han demostrado. Ha sido un largo camino, y además de la ayuda académica, su calidez humana ha hecho que andarlo fuera menos complicado.

I also want to thank Julian Pittard for his help and hospitality during my stay in Leeds.

Gracias a Jorge Cantó por su contribución a parte del trabajo presentado en esta Tesis.

Agradezco a Josep Martí, Ute Lisenfeld, Guillem Anglada, Laurent Loinard, Frank Wilkin, Martín Guerrero y Eduardo Battaner, por haber aceptado formar parte del tribunal que evaluará este trabajo.

Gracias a la gente que me ha ayudado durante mi estancia en el IAA, a Francisco Tapia, María Ángeles Cortés, y a Paco.

Quiero agradecer también, y ante el temor de dejarme algún nombre, a todos los profesores del CRyA (UNAM) que me enseñaron y ayudaron durante los primeros pasos de mi formación en Astrofísica. En particular quiero agradecer a Maru (Contreras), porque fue de ella de quién por primera vez escuché hablar de un "stellar wind". Recuerdo el día que me sentó frente a su computadora para mostrarme que AIPS no mordía.

Gracias también a mis compañeros de clase y amigos de la maestría, Daniel, Martín, Ramiro, Rosy, Alfonso y Edgar, ¡qué días aquellos! Gracias a Daniel por compartir y contagiarme su entusiasmo por la Astronomía. A Martin por las reflexiones. A Ramiro por la ayuda. A Karlita y Vicente. A Jesús, que es buena gente aunque lo niegue. A mis "roommates" Rosota y Roberto por salvarme la vida. Gracias Rosota, por la compañía, por el apoyo y por tu amistad, que alegría el día que llegó una niña nueva al CRyA, justo cuando más necesitaba una amiga. Gracias Roberto (¡Changa!), es toda una aventura conocerte.

Gracias también a todos los amigos que he hecho en mi paso por Granada. A Omaira, por su recibimiento, por su amistad y por su contagiosa carcajada. Gracias a Dani, Darío, Martiña, al Miguel, y al Toni, me confieso afortunada de haber coincidido en la vida con tan únicos y entrañables personajes. A la Yolis, que me ha supuesto una fuente de inspiración, gracias por todas esas tardes de despacho. A la Ampari (Tere), por su alegría y por su cariño. A Cris, por su valentía, aunque diga que no. A Moni, por su sensillez. Al 547 entero, Vicent, Yolis, Darío, Tere, Domi, y Ginevra (bienvenida). ¡Qué equipazo!

Agradezco a mi familia, a toda. A los Montes y a los García. A Don Juan y a Doña Petra.

A pá Beto y a má Luz. Las raíces de mi árbol. A mis amigas de toda la vida, Maggie, Carola (Yuyis), Andrea, Nelly, Laura, Chelys y Rosy, que me apoyan y me alegran la vida. Muchas gracias también a Mari, Carlos, Patri y María, por su cariño, por adoptarme y hacerme sentir en familia estando tan lejos de la mía.

Quiero agradecer de forma especial a Charly, por ser la persona en quién mis sentimientos y mi razón han convergido. Gracias por todo el apoyo, amor y certeza que has traído a mi vida. Esto apenas comienza...

Por último quiero agradecer a mis padres, Ernesto y Evangelina (Gloria). Me siento afortunada y orgullosa de ser su hija. Gracias por su incondicional apoyo y amor. Gracias por todo lo que me han dado, nada de lo que he hecho en mi vida sería posible sin ustedes. Y gracias por venir hasta acá.

Gabriela
Granada, España
Octubre 2011

Index

Summary

The radio flux density of stellar winds is expected to grow with frequency with a standard spectral index $\alpha \approx 0.6$ ($S_\nu \propto \nu^\alpha$; Wright & Barlow 1975 and Panagia & Felli 1975). Multi-frequency observations have allowed to characterize the stellar wind spectrum through the determination of spectral indices that are compared with those from theoretical models (e.g. Abbott et al. 1986, Litherer et al. 1997, Chapman et al. 1999). In binary systems, the standard spectrum from a single stellar wind has been observed to be affected by the contribution of an extra component of emission from a wind-wind collision region (WCR; e.g. WR 140 William et al. 1990). At present, observational evidences of such contribution have been mainly inferred by negative (or flat; $\alpha \sim 0.0$) spectral indices, which are related to a non-thermal (synchrotron) component of emission arising from the WCR (Eichler & Usov 1993, and more recently Pittard et al. 2006). Thus, the combination of observational and theoretical efforts have not only allowed the study of the stellar wind itself, but also the study of the emission from the WCR, constraining and deriving both stellar and orbital parameters in WR+OB binary systems (e.g. Dougherty et al. 2003, Pittard et al. 2006). Such studies have been focused on the non-thermal component of emission in wide binary systems, while in close systems ($P < 1$ year) the non-thermal component is unlikely to be detected due to the strong absorption of the WR wind (Dougherty & Williams 2000). For close systems, the radio spectrum is thought to be composed only by the thermal emission from the unshocked winds, loosing in this way any impact from its binarity. However, theoretical studies suggest that the free-free thermal emission from the WCR may also affect the total radio spectrum, becoming more important as the stars become closer (Stevens 1995, Pittard et al. 2006, Pittard 2010). Therefore, in close binaries, where the non-thermal emission is expected to be absorbed, its binarity may also have an influence on the spectrum, this time from entirely thermal processes. Furthermore, observations of WR stars suggest that for some close systems (e.g. γ^2 Vel, with $P = 78.5$ days; Chapman et al. 1999), the non-thermal emission could be able to escape the absorption, contributing to a composite spectrum with a flat spectral index, at least at certain orbital phases.

The main goal of this work is to determine the possible effect of a WCR contribution on the radio spectrum of close WR systems, being thermal and/or non-thermal (partially absorbed). The thermal WCR contribution, and its effect over the total spectrum, is expected to be highly dependent on the physical conditions of the material within the WCR (Pittard 2010). Such conditions are determined by the nature of the shocks forming the WCR, being either adiabatic or highly radiative, and depending as well on the stellar wind and the orbital parameters of

the system (Stevens et al. 1992). From an adiabatic WCR in a WR+O system, the hot gas within the WCR was found to remain optically thin, with a thermal component of emission with an spectral index $\alpha \sim -0.1$, and scaling with the binary separation between the stars as D^{-1} (Pittard et al. 2006). On the other hand, from radiative shocks in O+O type systems the thermal emission from the material was found optically thick with spectral indices up to $\sim$1.5 for frequencies between 100 and 250 GHz (Pittard 2010). The stellar wind parameters of WR stars are expected to favor the radiative cooling for close WR+OB systems (Parkin & Pittard 2008); however, studies regarding the effect of a thermal contribution on the radio spectrum for this kind of systems have not been performed at the moment.

In this work, we present a semi-analytic model for computing the free-free thermal radio-continuum emission from radiative shocks within colliding wind binaries (CWBs). Through this model, we investigate the effect of the binary separation and the stellar wind parameters on the total spectrum of systems with typical WR+O parameters. We found that most of the emission from the shocks arises from the optically thick region, with its flux density growing with frequency with a spectral index ~ 1.1. In this way, the total spectrum shows a standard stellar wind behavior at low frequencies with a spectral index ≈ 0.6, changing to one dominated by the shock at high frequencies. The impact of the WCR over the total spectrum is then seen as an excess of emission at high frequencies, with respect to that expected for a single stellar wind spectrum. From our model, we also found that the flux density of the WCR scales with the binary separation as $D^{4/5}$.

At the moment, there is a lack of multi-frequency observations of close WR binary systems that allow a proper determination and analysis of their spectra. In this work, we also present radio observations of a sample of 14 WR stars for a wide range of frequencies, from 1 to 250 GHz. Since a variable contribution from the WCR may be associated with orbital motion of the system, we look for variability and spectral indices that may indicate such influence. Thus, in this thesis, we have made use of three different instruments: the Giant Metrewave Radio Telescope (GMRT) at 1.4 GHz, the Very Large Array (VLA) at 5, 8.4, and 23 GHz, and the IRAM 30-m radio telescope at 250 GHz. First, we discuss the information obtained from the VLA and GMRT observations (centimeter wavelengths), and then we discuss the results from our high frequency observations (millimeter wavelengths). Indications of an excess of emission are inferred from the millimeter observations for WR 98 and WR 139 which we interpreted as observational evidence of our theoretical results. On the other hand, our observations also indicate that a non-thermal contribution is likely to be detectable in close systems, at least at certain orbital phases. This is the case of WR 98, 113, 141, and 156.

In this way, from our work we conclude that a WCR will have a significant effect on the radio spectra observed for WR stars, even for close binary systems with orbital periods $P <$ 1 year. Such effect could be detectable at centimeter wavelengths, as a non-thermal and/or an optically thin thermal contribution, and/or at millimeter wavelengths, in the form of an optically thick contribution detectable as an excess of emission. Furthermore, the strong absorption in these close systems may translate the effect of the non-thermal contribution to intermediate frequencies, between 20 and 50 GHz (2 cm and 7 mm). Thus, our results indicate that in close systems the WCR is likely to have a significant impact in different ranges of the radio spectrum.

This represents a more complex scenario for the case of close systems, in comparison with wide binaries, for which the binary effect essentially results from the non-thermal emission, which mainly contributes at low frequencies ($\lesssim$ 10 GHz).

Summarizing, our results provide evidence of the contribution from the WCR even for close WR systems, for which it uses to be discarded due to the strong absorption from the WR wind. We propose to search for periodic variability (in flux density and/or α), as a method to unambiguously confirm the WCR contribution being the reason of the deviations found in the spectrum of our sources. This kind of study will confirm both the WCR effect at centimeter and millimeter wavelengths. Furthermore, a statistical study is required in order to corroborate and generally determine the impact of the WCR over the radio flux determined from observations of this kind of systems. This is important for example to quantify the possible overestimation of mass loss rates inferred from radio observations due to the WCR contribution in close systems. Furthermore, theoretical models of radio emission of close WR systems have not been performed yet, and this study shows that detailed models are required in order to study the WCR influence in such systems.

1

Introduction

The purpose of this thesis is the study of the radio emission from stellar winds of Wolf-Rayet stars, with a special interest in the effect of the binarity over the total radio spectrum. In Wolf-Rayet binary stars, the strong stellar winds of the stellar components interact, resulting in a wind-wind collision region (WCR) that contributes to the total radio emission. In this chapter, we describe the origin and nature of Wolf-Rayet stars, as well as the main process that gives them as a result: the high mass loss of massive stars in the form of stellar winds. We describe the properties and observational evidence of such stellar winds centering in the studies at radio frequencies. We discuss how the WCR modifies the spectrum at all frequency bands of the electromagnetic spectrum with respect to that expected for a single star. Finally, we focus on the effect at radio frequencies, which is expected to result from an extra contribution of emission arising from the WCR. Thus, we describe the origin and nature of such extra component of emission, and its different effects on the total resulting radio spectrum.

1.1 Stellar Winds from Massive Stars

The evolution and final destiny of a star is mainly determined by its initial mass. Massive stars, with an initial mass higher than $10\,M_{\odot}$, are the hottest and most luminous stars, with effective temperatures $T_{eff} \gtrsim 15\,000\,K$, and stellar luminosities, $L_{\star}$, between $10^4 - 10^6\,L_{\odot}$. As main sequence stars, they are classified into the spectral types O and B. Due to their high luminosities, these stars suffer a high loss of material via *stellar winds*. For stars of initial masses exceeding $\sim 25\ M_{\odot}$, the high mass-loss suffered during the main-sequence phase strips out the external layers of the star, leaving their cores exposed, which are now mainly composed by Helium. These objects are known as Wolf-Rayet (WR) stars. During this stage of evolution, these stars continue losing material via strong winds that reach densities up to 10 times those of their early-type progenitors. In this way, stellar winds play an important role along the course of the stellar evolution. Furthermore, they are an important source of the chemical enrichment of the interstellar medium of the galaxy, injecting both mass and kinetic energy to the medium. In this section, we describe the main parameters that characterize a stellar wind, followed by a review of the basic physics governing the drive of the stellar winds from massive stars. We

mainly focus in the studies regarding WR stars, with special emphasis on those performed at radio frequencies.

1.1.1 Stellar Wind Parameters

Stellar winds are defined as the continuum outflow of material from stars. Two main parameters characterize the stellar winds: the *mass loss rate* $\dot{M}$, usually expressed in units of solar masses per year ($M_\odot\,\mathrm{yr}^{-1}$), and the *terminal velocity* v_∞, which is defined as the maximum velocity reached by the wind at large distances from the star.

All stars display some kind of stellar wind. The characteristics of the wind, and hence, its impact over the evolution of the star, will be highly dependent on the initial stellar mass. For example, our Sun presents a stellar wind with $\dot{M} \approx 10^{-14}\,M_\odot\,\mathrm{yr}^{-1}$ and $v_\infty \approx 700\,\mathrm{km\,s}^{-1}$. Thus, along its entire life ($\sim$ 10 billion years), the Sun will loss only 0.01% of its initial mass, which will not have a significant impact over its evolution (although it is enough to have a strong impact over its surroundings, including the Earth). On the other hand, for massive stars, the stellar wind parameters may reach values up to $\dot{M} \sim 10^{-5}\,M_\odot\,\mathrm{yr}^{-1}$, and $v_\infty \sim 3000\,\mathrm{km\,s}^{-1}$, which implies a loss of several solar masses during their comparative short lifetime ($\sim$ million years).

We assume a star with a spherically symmetric and stationary wind. From the equation of mass continuity

$$\frac{\partial \rho}{\partial t} + \nabla \cdot (\rho v) = 0, \tag{1.1}$$

we obtain that the mass loss rate $\dot{M}$ is related to the mass density and velocity of the wind, ρ and v respectively, as

$$\dot{M} = 4\pi r^2 \rho(r) v(r), \tag{1.2}$$

where r is the distance from the center of the star.

The gas escapes from the outer layers of the star, being accelerated from low velocities at small radii, to high velocities at large distances from the star. For a large distance r, the velocity approaches asymptotically a maximum value. In this way, we can define the terminal velocity as $v_\infty = v(r \to \infty)$. The distribution of velocities $v(r)$ is known as the *velocity law*, and it is usually described by a *β-law*,

$$v(r) \simeq v_0 + (v_\infty - v_0)\Big(1 - \frac{R_\star}{r}\Big)^\beta, \tag{1.3}$$

where $R_\star$ is the radius of the star, and $v_0 = v(R_\star)$. The parameter β determines how fast the velocity increases with r. For example, for the stellar winds of massive stars, $\beta \approx 0.8$, reaching $\sim 80\,\%$ of their terminal velocity at a few stellar radii (Lamers & Cassinelli, 1999).

1.1.2 Radiatively Driven Winds

The process from which the wind is originated, as well as its parameters, depends on the mass of the star. In a star with a relatively low mass and temperature, like our Sun, the sub-surface convective layer mechanically heats the corona to a million degrees, and the wind is then driven

by gas pressure. On the other hand, in massive stars, there is not such convective layer, and the temperature of the winds remains comparable to those of the stellar surface ($10^4 - 10^5$ K). Thus, in this case, the star lacks the high gas pressure required to drive the wind out against the star's gravity. In this case, the high temperatures of massive stars imply a high radiative flux that results in a high radiation pressure that drives out the wind material. Here, we present a summary of the theory and equations, as well as the main approximations developed for the study of the radiatively driven winds, which are the object of our study. Here, we mainly follow the description presented in Owocki (2004). A detailed analysis can also be found in Lamers & Cassinelli (1999) and Madura (2010).

Radiative Acceleration

Using mass conservation (equation 1.2), and from the ideal gas law,

$$P = \rho a^2, \tag{1.4}$$

where P and ρ are the pressure and density of the gas, and a is the sound speed. The equation of motion for a spherically symmetric and steady wind can be written as

$$\left(1 - \frac{a^2}{v^2}\right) v \frac{dv}{dr} = -\frac{GM}{r^2} + \frac{2a^2}{r} + \frac{da^2}{dr} + g_r, \tag{1.5}$$

where G is the gravitation constant, M is the mass of the star, and g_r represents an external acceleration term. For hot stars, this term is related to the absorption and scattering of the stellar radiation. In order to obtain an outflow with a net acceleration, the right hand side of equation (1.5) must be positive. For Sun-like stars, the sound speed terms are responsible for overcoming the gravity term, but in the case of massive stars it is the g_r term which plays the relevant role. In general, this term can be written as $g_r = g_e + g_L$, in which both contributions to the scattering of the continuum photons from the free electrons, g_e, and from the spectral lines, g_L, are considered.

Eddington Limit

The free electron scattering has not any dependence with frequency, hence it does not alter the total luminosity of the star L_*, and the radiative energy flux at any radius r can be written as $F = L_*/4\pi\, r^2$. Thus, the radiative momentum flux is given by $F/c = L_*/4\pi\, r^2 c$, where c is the speed of light. For a point-like radiation source, the opacity due to electron scattering is a constant given by $\kappa_e = \sigma_e/\mu_e$, where σ_e is the classical Thompson cross-section, and $\mu_e = 2m_H/(1+X)$ is the mean atomic mass fraction of hydrogen, with m_H and X being the mass and the mass fraction of hydrogen, respectively. In this way, the product of the opacity and the radiative momentum flux results in the radiative acceleration from free electron scattering

$$g_e(r) = \frac{\kappa_e L_*}{4\pi r^2 c}. \tag{1.6}$$

In order to compare radiative (g_e) and gravity (g) accelerations we define the Eddington parameter

$$\Gamma_e = \frac{g_e}{g} = \frac{\kappa_e L_*}{4\pi G M_* c}. \tag{1.7}$$

The limit $\Gamma_e \to 1$ is known as the Eddington limit, at which the radiation of the star would overcome the gravitational force, and the star would become gravitationally unbound. Hot stars with strong stellar winds are only a factor of two or so below this limit, which suggest that only a slight increase in the opacity would break the hydrostatic equilibrium of the star. However, it is important to realize that a stellar wind represents the outer envelope outflow from a nearly static, gravitationally bound base, and as such it is not consistent with the entire star exceeding the Eddington limit (Owocki 2004). Actually, the requirement for a wind is a driving force which is increasing naturally from being smaller to larger than gravity at some radius near the stellar surface.

Line Scattering

As we described above, free (continuum) electron scattering alone is not enough to account for the strong stellar winds displayed by massive hot stars. Thus, line scattering is the ideal method to drive the winds in such stars. When an electron is bound to one of the discrete levels of an atom, it absorbs a photon of just the energy required for the electron to change to another discrete level. The photon is then re-emitted by the desexcitation of the atom to a lower or to the ground energy level. This is known as line scattering, and it often results in the observed lines in the spectrum of stars. However, the photon is absorbed only by the atoms in resonance with it. Thus, in this simple way this process will be inefficient, since the atoms would interact only with a small fraction of the stellar flux. Furthermore, the photons will be absorbed or scattered only by atoms in the lower layers of the atmosphere, and the outer layers will not receive the photons at such line frequency. As a consequence, the acceleration in the outer layers due to spectral lines would be strongly diminished. However, if the outer layers of the atmosphere are moving outwards, the local line resonance frequency is red-shifted by the Doppler effect, desaturating the lines. In this way, the atoms are now able to absorb photons that in a static case would be at higher frequencies. A broader range of the stellar flux spectrum is now contributing to the radiative acceleration force, which allows it to overcome the gravity and accelerate the outflow material to the high speeds observed in massive stars.

Line Driven Winds

A photon emitted by the stellar photosphere can be absorbed by a line transition in only a narrow region of the wind. The geometric width of the interaction region is defined by the frequency width of the profile function of the line $\phi(\Delta\nu)$. A narrow absorption profile will mean a narrow interaction region (Lamers & Cassinelli 1999). For the usual case of the thermal broadening of the line, the geometric width of the interaction is about the so called *Sobolev length*, $l_s \equiv v_{th}/(dv/dr)$, with v_{th} being the thermal speed of the ions. Thus, a large gradient dv/dr will also result in a narrow interaction region. In a supersonic flow, the Sobolev length is of order v_{th}/v ($\ll 1$) smaller than a typical flow variation scale, for example the density/velocity

scale length $H \equiv |\rho/(d\rho/dr)| \approx v/(dv/dr)$ (Owocki 2004). In the limit when the interaction region is very narrow, the function $\phi(\Delta\nu)$ can be approximated by a delta function, and the radiative transfer problem is then reduced to local conditions of a point called the *Sobolev point*. This approximation is known as the *Sobolev approximation*.

Under the Sobolev approximation, the key parameters of the line can now be described in terms of the local conditions at any radius. In particular, for a point-like radiation source, the single line force is

$$g_L = \frac{\kappa v_{th} \nu L_\nu}{4\pi r^2 c^2} \left(\frac{1 - e^{\tau_S}}{\tau_S} \right), \tag{1.8}$$

where κ is the opacity near the line center, ν is the central frequency of the line, L_ν is the luminosity spectrum, and the Sobolev optical depth can be written as

$$\tau_S = \rho \kappa l_{Sob} = \frac{\rho \kappa v_{th}}{dv/dr}. \tag{1.9}$$

In reality, the radiative force is composed by the contribution of a large number of lines within a range of frequencies. Castor, Abbott and Klein (1975) introduced a formalism for computing the cumulative line acceleration from a parametrized ensemble of lines (better known as the CAK theory). For this, they assumed an spectral distribution with individual lines nearly independent. The total line force (g_{Ls}) due to all the spectral lines can be expressed in terms of g_e (equation 1.6) as

$$g_{Ls} = g_e(r)\, M(t) = \frac{\kappa_e L_*}{4\pi r^2 c}\, M(t), \tag{1.10}$$

where $M(t)$ is called the *force multiplier* defined as

$$M(t) = k\, t^{-\alpha}, \tag{1.11}$$

where k is a constant of normalization related with the overall strength of the lines, and α determines the fraction of optically thick lines (Madura 2010). This equation introduces the dimensionless electron optical depth parameter $t \equiv \kappa_e \rho v_{th}/(dv/dr)$ (Lamer & Cassinelli 1999).

The above description assumes single line scattering. This is reasonable in the case of only a few atomic transitions producing the acceleration, or a lot of transitions but with widely spaced spectral lines. The reason is that in general, the photons scattered by a spectral line cannot be absorbed again by the same spectral line at any region of the wind. However, such a single scattering formalism seems inadequate for the much stronger winds of WR stars. Overall, observations indicate that WR winds are especially strong, and even optically thick to continuum scattering by electrons. For WR stars it is necessary to account for the absorption of photons by multiple scattering between overlapping thick lines.

1.1.3 Wolf-Rayet Stars

As we mentioned above, WR stars are understood as evolved objects resulting from the high mass loss of early O-type stars with masses higher than $\sim$25 $M_\odot$. This evolutionary scenario was first described by Conti (1976). During its early-type phase, the star loses most of its H-rich atmosphere, leaving exposed their nuclei mostly composed by He. In this way, the star continues

losing material, forming an expanding and dense envelope composed by He and the subsequent products of He burning (N, C, and O). Therefore, WR spectra are characterized by strong and broad emission lines of atoms of these products. The spectral classification of WR stars result in two main subtypes:

- *WN subtypes*, which show strong lines of He and N. These spectral subtypes follow a scheme involving line ratios of N_{III-IV} and He_{I-II}, ranging from WN2 to WN5 for early (WNE) stars, and WN7 to WN9 for late WN (WNL) stars (WN6 stars can be either early or late type). An "h" suffix may be used to indicate the presence of emission lines due to H (Smith, Sara & Moffat 1996).

- *WC subtypes*, with lines of He, C and O. These subtypes depend on the line ratios of C_{III} and C_{IV} lines along with the appearance of O_{III-V}, spanning WC4 to WC9 subtypes, for which WC4-6 stars are early (WCE) and WC7-9 are late (WCL).

Rare O-rich WO stars form an extension of the WCE sequence. A third subtype of WN/C stars are indeed considered to be at an intermediate evolutionary phase between WN and WC (see Crowther 2007).

Typically, WR stars have masses of 10-25 $M_\odot$. However, its evolution, and thus its final mass, is highly dependent on the initial mass of its star progenitor. Some WR stars are post-red supergiants (RGS) within a fairly limited mass range of probably $\sim$ 40-75 $M_\odot$. The evolution proceeds via an intermediate Luminous Blue Variable phase (LBV) phase above 30 $M_\odot$ (Crowther 2007). Crowther (2007) summarized the possible evolutionary tracks for a WR star according with its initial mass. For stars initially most massive than $\sim 70\,M_\odot$:

$$\text{O} \rightarrow \text{WN(H-rich)} \rightarrow \text{LBV} \rightarrow \text{WN(H-poor)} \rightarrow \text{WC} \rightarrow \text{SNIc},$$

stars of initial mass from $\sim 40 - 75\,M_\odot$,

$$\text{O} \rightarrow \text{LBV} \rightarrow \text{WN(H-poor)} \rightarrow \text{WC} \rightarrow \text{SNIc},$$

and for stars of initial mass in the range $\sim 25 - 40\,M_\odot$,

$$\text{O} \rightarrow \text{LBV/RSG} \rightarrow \text{WN(H-poor)} \rightarrow \text{WC} \rightarrow \text{SNIc}.$$

Indeed, these scenarios are not entirely settled, for instance, the role of the LBV phase is not yet established (see Crowther 2007 for details).

In general, WR stellar winds are a factor of $\sim$ 10 denser than those from their O-type progenitors, with $\dot{M}$ of the order of $\sim 10^{-5}\,M_\odot\,\mathrm{yr}^{-1}$, and v_∞ of $\sim 10^3\,\mathrm{km\,s}^{-1}$. In WR stars, winds normally reach a significant fraction of their terminal velocity before they become optically thin in the continuum, just at a few stellar radii (Section 1.1.1). The stellar and wind parameters depend on the spectral subtype. In Figure 1.1 we present a table from Crowther (2007) where the characteristic values of the main physical parameters of WR stars (within the Milky Way) for each spectral subtype are displayed.

Sp	T_*	log L	$\dot{M}$	v_∞	log N(LyC)	M_v	Example
Type	kK	$L_\odot$	$M_\odot$ yr^{-1}	km s^{-1}	ph s^{-1}	mag	
WN stars							
3-w	85	5.34	–5.3	2200	49.2	–3.1	WR3
4-s	85	5.3	–4.9	1800	49.2	–4.0	WR6
5-w	60	5.2	–5.2	1500	49.0	–4.0	WR61
6-s	70	5.2	–4.8	1800	49.1	–4.1	WR134
7	50	5.54	–4.8	1300	49.4	–5.4	WR84
8	45	5.38	–4.7	1000	49.1	–5.5	WR40
9	32	5.7	–4.8	700	48.9	–6.7	WR105
WNha stars							
6ha	45	6.18	–5.0	2500	49.9	–6.8	WR24
9ha	35	5.86	–4.8	1300	49.4	–7.1	WR108
WC and WO stars							
(WO)	(150)	(5.22)	(–5.0)	(4100)	(49.0)	(–2.8)	(BAT123)
(4)	(90)	(5.54)	(–4.6)	(2750)	(49.4)	(–4.5)	(BAT52)
5	85	5.1	–4.9	2200	48.9	–3.6	WR111
6	80	5.06	–4.9	2200	48.9	–3.6	WR154
7	75	5.34	–4.7	2200	49.1	–4.5	WR90
8	65	5.14	–5.0	1700	49.0	–4.0	WR135
9	50	4.94	–5.0	1200	48.6	–4.6	WR103

Figure 1.1 Physical and wind parameters of Milky Way WR stars (Large Magellanic Cloud in parenthesis) taken form Crowther 2007. Note: Data adapted from Heral, Hillier & Schulte-Ladbeck (2001) nd Hamann, Gräfener & Liermann (2006) for WN stars; and from Barniske, Hamann & Gräfener (2006) and Crowther et al. (2002, 2006a, and references therein) for WC stars. Abundances are shown by mass fraction in percent. Mass-loss rates assume a volume filling factor of $f = 0.1$.

1.2 Radio Emission from Stellar Winds

The stellar winds in hot massive stars are ionized by the strong radiation of the star. Thus, the free electrons interact with the ions, resulting in free-free thermal emission detectable from IR to radio frequencies. The thermal emission (ε_ν) and absorption (α_ν) coefficients at a frequency ν are given by (Rybicki & Lighthman 1979),

$$\varepsilon_\nu = 6.8 \times 10^{-38}\, Z^2\, n_e n_i\, T^{-1/2} e^{-h\nu/kT}\, g_\nu(T), \tag{1.12}$$

$$\alpha_\nu = 3.7 \times 10^{8} T^{-1/2} Z^2\, n_e n_i \nu^{-3} (1 - e^{-h\nu/kT})\, g_\nu(T), \tag{1.13}$$

where Z is the ionic charge, n_e and n_i are the electron and ion number densities, T is the temperature of the gas, and $g_\nu(T)$ is the Gaunt factor. In this way, at radio frequencies, the ionized-expanding envelope produces a spectrum characterized by an excess of emission, with respect to that resulting from the photosphere of a star with no wind at all. Wright & Barlow (1975) and Panagia & Felli (1975) presented a model for deriving the radio and IR spectrum resulting from the free-free emission of ionized stellar winds. In this section, we explain this model and present the equations derived by these authors relating the flux density S_ν with the stellar wind parameters.

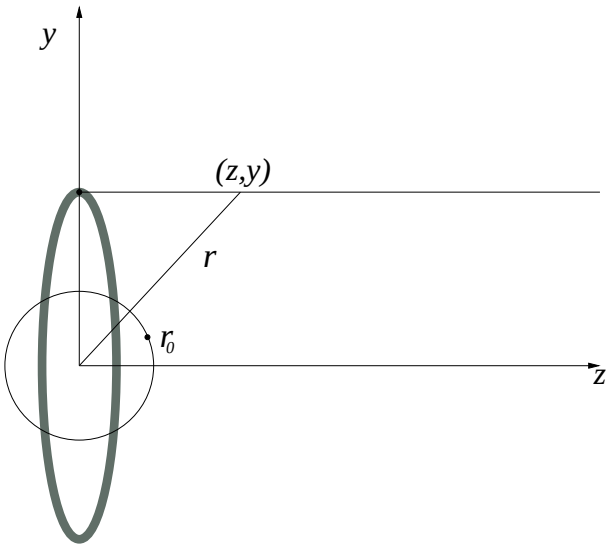

Figure 1.2 Reference frame for computing the optical depth at each impact parameter $\tau(y)$. The observer is located in the plane along the z-axis. The gray ring represents an infinitesimal ring of the nebula defined by the impact parameter y.

1.2.1 The Radio Spectrum of Stellar Winds

Consider an homogeneous flow of completely ionized gas with a constant electron temperature T_e, ejected at a radius r_0, with a uniform mass loss rate $\dot{M}$ and a constant velocity v_w. Assuming the resulting nebula to be spherically symmetric, from equation (1.2), the number electron density at a radius r from the center of the star can be written as

$$n_e = \frac{\dot{M}}{4\pi r^2 v_\infty \mu_e m_H}, \tag{1.14}$$

where μ_e is the mean atomic weight per electron, and m_H is the mass of the H atom. Now, let's consider a reference frame with the star in the origin, and the line of sight along the z-axis (see Figure 1.2). For simplicity, we use all lengths in units of r_0. Then we have $r^2 = z^2 + y^2$ from which we can write

$$n(z) = \frac{n_0}{z^2 + y^2}, \tag{1.15}$$

where n_0 is the value of the electron density at r_0. The intensity of the radiation emerging from the shell at an impact parameter y is obtained by the solution to the radiative transfer problem,

$$I_\nu(y) = \int_0^{\tau(y)} B_\nu(T_e)\, e^{-\tau} d\tau = B_\nu(T_e)(1 - e^{-\tau(y)}), \tag{1.16}$$

where

$$B_\nu(T_e) = 2k\, T_e\, \nu^2/c^2 \tag{1.17}$$

is the Planck function in the Rayleigh-Jeans approximation and k is the Boltzmann's constant. Assuming the ion number density $n_i = n_e = n$, the the absorption coefficient (equation [1.13])

can be written as $\alpha_\nu = n^2(z)\kappa_\nu$, where

$$\kappa_\nu = 8.44 \times 10^{-28} \left[\frac{\nu}{10\,\mathrm{GHz}}\right]^{-2.1} \left[\frac{T_e}{10^4\,\mathrm{K}}\right]^{-1.35} a_\nu(T_e), \tag{1.18}$$

for which we will take $a_\nu(T_e) = 1$. Thus, the free-free optical depth is obtained by integrating the absorption coefficient along the line of sight, which can be written as

$$\tau(y) = 2\int_0^\infty n^2(z)\,\kappa(\nu)\,\mathrm{d}z = \frac{\pi}{2y^3} n_0^2\,\kappa_\nu\,r_0, \tag{1.19}$$

for $y \geq 1$. The flux density received from an infinitesimal ring of the nebula, defined by the impact parameter y (see Figure 1.2), can be written as $dS_\nu(y) = [I_\nu(y)/L^2]\,2\pi r_0\,ydy$, where L is the distance from the observer. Thus, by substituting equation (1.16) and integrating along the impact parameter, we obtain that the total flux density is given by

$$S_\nu = \frac{B_\nu(T_e)}{L^2}\int_0^\infty \left(1 - e^{\tau(y)}\right) 2\pi r_0^2\,ydy. \tag{1.20}$$

This equation cannot be analytically solved in the general case, but a simple approximation allows an easy and satisfactory estimate of it. Let us define a critical distance $y_c(\geq 1)$ such that the optical depth along a line of sight is high, thus from equation (1.19)

$$\tau_c = \frac{\pi}{2y_c^3} n_0^2\,\kappa(\nu)\,r_0 \gg 1. \tag{1.21}$$

With this definition y_c is now a function of ν. Note that for every value of $y < y_c$, $\tau(y) > \tau_c$. Then, the term $e^{\tau(y)}$ in equation (1.20) can be neglected, and this equation can be written as

$$S_\nu \approx \frac{\pi r_0^2\,B_\nu(T_w)}{L^2}\left[2\int_0^{y_c} y\,\mathrm{d}y + 2\int_{y_c}^\infty (1 - e^{-\tau(y)})\,y\;\mathrm{d}y\right]. \tag{1.22}$$

Expanding the exponential of the second term in a Taylor series, we obtain

$$S_\nu \approx \frac{\pi r_0^2\,B_\nu(T_w)\,y_c^2}{L^2}\left[1 + 2\sum_{n=1}^\infty \frac{(-1)^{n+1}}{n!}\,\frac{\tau_c^n}{(3n-2)}\right]. \tag{1.23}$$

The first term in brackets in the equation is related with the optically thick region of the wind, and the second term with the extended region of the envelope. Although the series require to be evaluated numerically, this will be only a constant term, while the frequency dependence is in the product $B_\nu(T_e)y_c^2$.

Since $\tau_c >> 1$, the equation (1.23) is not sensitive to the particular value of τ_c. For example, adopting $\tau_c = 3$, the series can be evaluated to give a value of 4.572. Thus, the value of the series shows that most of the emission is actually coming from the extended region of the wind. On the other hand, as we mentioned before, the dependence of S_ν with frequency is in the product $B_\nu(T_e)y_c^2$; thus, from equations (1.18) and (1.21) it can be seen that $y_c^2 \propto \nu^{-1.4}T_e^{-0.9}$. Therefore, from equations (1.23) and (1.17) we conclude that $S_\nu \propto \nu^{0.6}$. Defining the *spectral index*, α, as the slope of a power-law determining the dependence of flux density with frequency, such that

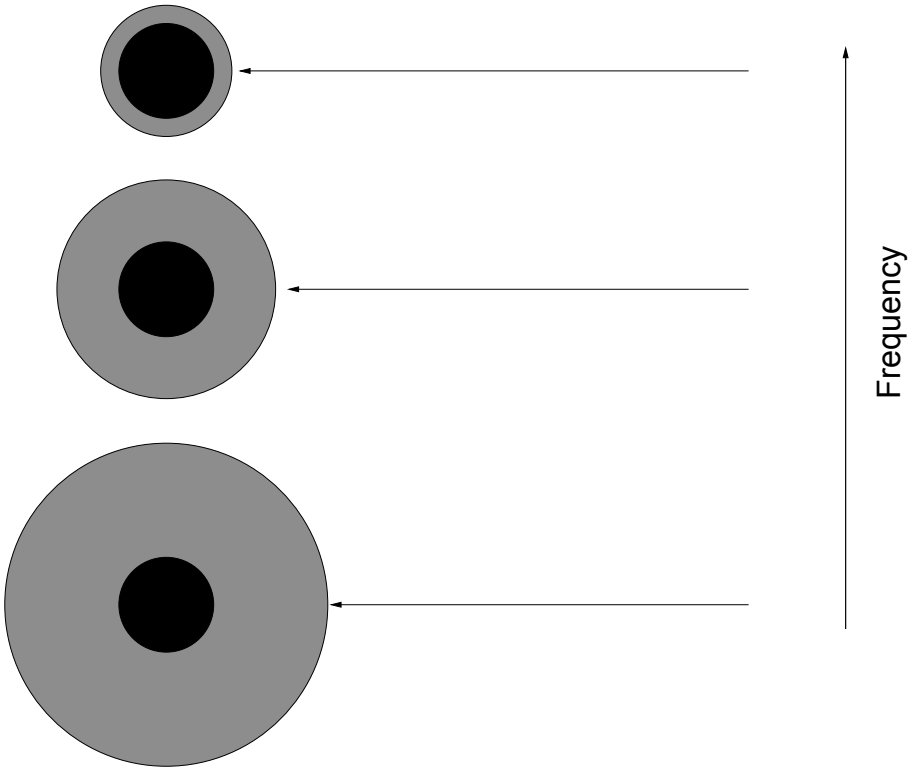

Figure 1.3 A schematic representation of the radio emitting region (gray) resulting in the radio excess of emission from the stellar wind, with respect to the emission from the stellar photosphere (black). The effective radius of the radio-photosphere, defined by $\tau \approx 1/3$, increases to higher frequencies (from bottom to top).

$S_\nu \propto \nu^\alpha$, we have $\alpha = 0.6$ as the characteristic value for a *standard wind spectrum*. This value is taken as reference in order to compare and disentangle the nature of the emission that is been detected from observations of stellar winds.

Finally, after some manipulations of equation (1.23), and substituting equation (1.14), the flux density at radio frequencies arising from the stellar wind is given by

$$\begin{aligned} S_\nu =& 5.12 \left[\frac{\nu}{10\,\mathrm{GHz}}\right]^{0.6} \left[\frac{T_e}{10^4\,\mathrm{K}}\right]^{0.1} \left[\frac{\dot{M}}{10^{-5}\,\mathrm{M_\odot\,yr^{-1}}}\right]^{4/3} \\ & \times \left[\frac{\mu}{1.2}\right]^{-4/3} \left[\frac{v_\infty}{10^3\,\mathrm{km\,s^{-1}}}\right]^{-4/3} \left[\frac{d}{\mathrm{kpc}}\right]^{-2} \bar{Z}^{2/3}\ \mathrm{mJy}, \end{aligned} \tag{1.24}$$

where $\bar{Z}$ is the average ionic charge that comes from replacing $n_i = \bar{Z}\, n$. This equation allows to relate the mass loss rate $\dot{M}$ with the flux density S_ν. Thus, trough radio continuum observations it is possible to determine $\dot{M}$.

It is also of interest to define a representative radius R_ν for the emitting region at each frequency. We define this radio as the distance within which half of the emission is produced. We find that it corresponds to a $\bar{y}$ such that $\tau(\bar{y}) = 0.399$. Thus, combining equations (1.19)

and (1.18) we obtain

$$R_\nu = 6.23 \times 10^{14} \left[\frac{\nu}{10\,\mathrm{GHz}}\right]^{-0.7} \left[\frac{T_e}{10^4\,\mathrm{K}}\right]^{-0.45} \left[\frac{\dot{M}}{10^{-5}\,\mathrm{M_\odot\,yr^{-1}}}\right]^{2/3} \times \left[\frac{\mu}{1.2}\right]^{-2/3} \left[\frac{v_\infty}{10^3\,\mathrm{km\,s^{-1}}}\right]^{-2/3} \bar{Z}^{1/3}\,\mathrm{cm}. \tag{1.25}$$

This equation establishes the inverse dependence, $R_\nu \propto \nu^{-0.7}$. In this way, the higher the observing frequency, the smaller the size of the source. In other words, as the observing frequency increases, the emission is arising from progressively the inner regions of the wind. This is schematically shown in Figure 1.3.

The previous description for the radio spectrum results essentially from the assumed number density profile, $n \propto r^{-2}$. In a general case, with a density profile $n \propto r^{-\delta}$, solving the problem in a similar way as in the particular case of $\delta = 2$ gives the relation $S_\nu \propto \nu^{(4\delta-6.2)/(2\delta-1)}$, valid for $\delta \geq 1.5$ (Wright & Barlow 1975). This relation clearly predicts a change in the spectral index for values of $\delta \neq 2$. For a (physical reasonable case of) non-spherical geometry, the total gas number density is expected to fall with $\delta < 2$, producing a flatter radio spectrum. Thus, spectral indices greater than 0.6 are unlikely to result from a non-spherical geometry. Wright & Barlow (1975) analyzed whether the absorption of all the available photons, changing the dependence with the radius of the ionized fraction and steepening the numeric density profile, could be able to explain a value of α higher than 0.6. They concluded that such process is unlikely to affect the spectral index in the radio region. However, they did not discard that instabilities could occur in the winds, leading to neutral condensations of much higher density than the ambient one, also resulting in an ionized structure that depends on the radius and, thus, affecting the spectrum at the radio emitting regions.

Radio Observations of Massive Stars

In the last years, radio continuum observations have been very successful for the detection of the stellar wind emission from massive stars. Multiwavelength observations have been used to determine spectral indices and, in this way, characterize their radio spectra. Furthermore, the relatively simple relation described by equation (1.20), has allowed to determine mass loss rates directly from these radio observations. Here, we mainly focus in the observations and results presented for WR stars.

The first detections of stellar winds from radio continuum observations were presented in the seventies (e.g. Altenhoff et al. 1973, Barlow 1979). Wright & Barlow (1975) analyzed the spectrum from radio to IR, and compared them with their results from the model previously reviewed here. Although they found the observations to be in general agreement with their predictions for the spectral index, they remarked the occurrence of deviations in some cases (e.g. V1016 Cyg; see Figure 1.4). In the last decades, the improvement in sensitivity of new instruments, as the Very Large Array (VLA) and the Australian Telescope Compact Array (ATCA), have allowed to increase the sample of detected massive stars. Abbott et al. (1986) presented and summarized previous observations (from Bieging et al. 1982, Hogg 1982, 1984,

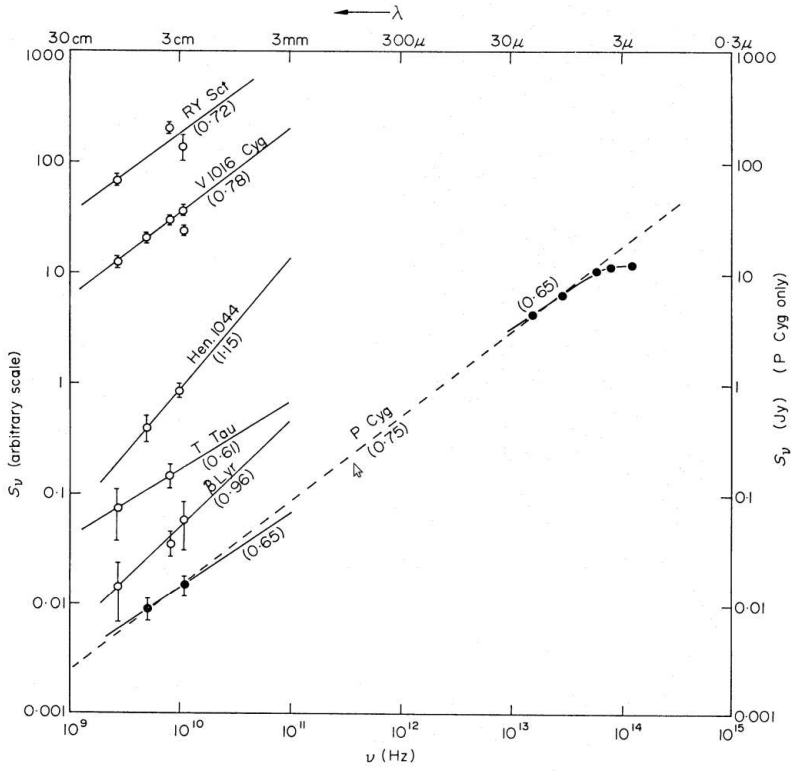

Figure 1.4 Plot of S_ν vs. ν (in Hz) and wavelength λ for a sample of six radio stars taken from Wirght & Barlow (1975). The left-hand ordinate S_ν is on an arbitrary scale and the right-hand ordinate is S_ν in Jy, applicable to P Cyg only. References used in constructing the radio spectra were Althenhoff et al. (1973), Hjellming, Blankenship & Balick (1973), Hughes & Woodsworth (1973), Purton et al. (1973), Seaquist & Gregory (1973), Wright et al. (1974), and the infrared spectrum of P Cyg was derived from Gehrz et al. (1974). The numbers in parentheses indicate the spectral index for each star.

1985, Dickel et al. 1980, Florkowski 1982, Becker & White 1985) completing a total sample of 26 WR stars detected at least at one radio frequency (4.8 GHz). By determining spectral indices, and/or comparing with IR and/or optical observations, they characterized the spectrum of the detected stars. Bieging et al. (1989) presented observations of a sample of early O-type and B-type stars (here in after referred as OB stars). Since for OB stars mass loss rates are in general one order of magnitude lower that for WR stars, stellar winds from early type stars become more difficult to be detected. Thus, these authors detected only those with the higher luminosity of a sample of 88 stars, characterizing the spectrum of 25 OB stars. Leitherer et al. (1995), (1997) and Chapman et al. (1999) presented observations at 1.4, 2, 4.8 and 8.4 GHz of a sample of 36 southern WR stars, from which 20 were detected at least at one frequency. More recently Cappa et al. (2004) presented observations at 8.4 GHz of a sample of 34 WR stars with 15 detections, some of them already previously detected. Furthermore, other WR stars have been also detected by individual observations (e.g. WR 140 by Williams et al. 1987, 1990; WR 146 Moran et al. 1989, 1997), or as part of smaller samples (Leitherer & Robert 1991, Setia Gunawan et al. 2001, Contreras et al. 1996, Contreras et al. 2004, Monier et al. 2002).

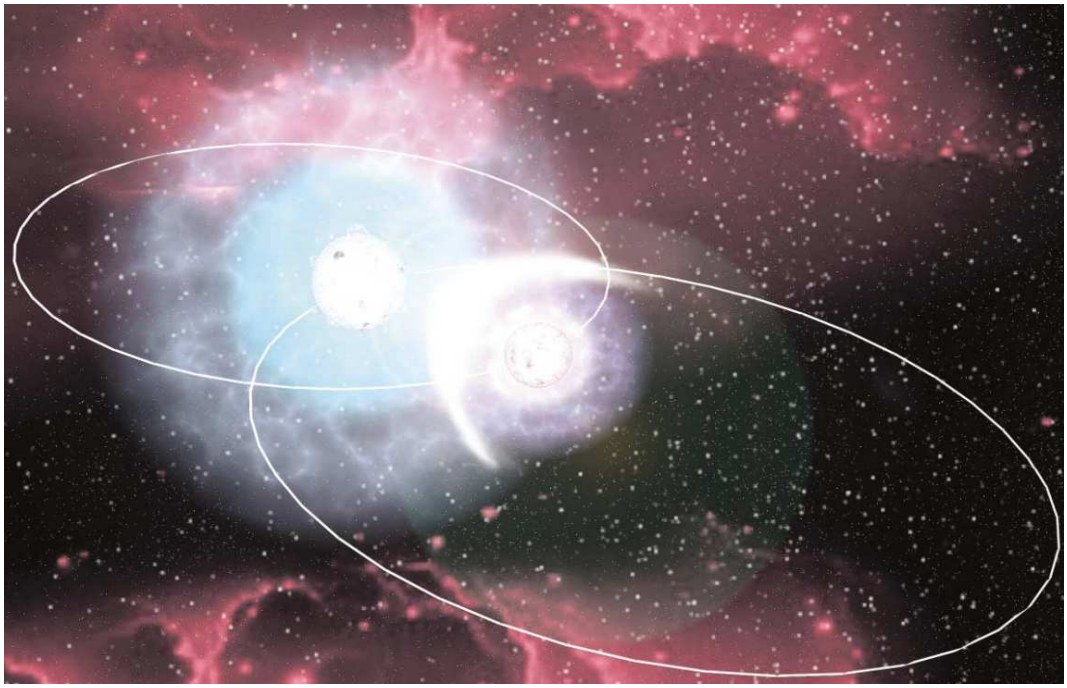

Figure 1.5 Artistic impression of a colliding wind binary (CWB). The bow-shock structure forming the wind-wind collision region (WCR) between the stars can be seen (Credit Andre Viera, IAG-USP Brazil; Pittard 2003).

1.3 Colliding Wind Binaries

In massive binary systems, the strong stellar winds of the two individual stars collide, forming a dense structure of material at the interacting region. The strong shocks resulting from this interaction modify the physical conditions of the interacting material, increasing its density and temperature up to several orders of magnitude compared to those from the unshocked material. For unequal winds, the stronger wind (defined to come from the primary star) will sweep the material from the weaker wind (arising from the secondary star), forming a bow-shock structure facing the secondary star (Figure 1.5). In this way, the wind-wind collision region (WCR) within a colliding wind binary (CWB) is expected to affect the emission of the system at all frequency bands of the spectrum, from radio to γ-ray energies (e.g. Pittard & Dougherty 2006). The influence of the region over the resulting emission is expected to be highly variable due to the nature of the orbit, changing in a timescale related to the orbital period of the system P. Variability may result from changes in the intrinsic emission and in the column density between the interacting region and the observer. The intrinsic emission may change due to the variability in the binary separation due to an eccentric orbit, and/or intrinsic variability of the individual winds. On the other hand, absorption effects resulting from the orbital motion are highly dependent on the orbit inclination angle, i . Colliding stellar winds have also been detected in O+O type systems (Contreras & Rodriguez 1995, Van Loo et al. 2008, Blomme et al. 2010). However, since this thesis is centered in the study of WR winds, in the following we mainly focus in the description and studies of CWBs composed of a WR star and an OB star (WR+OB).

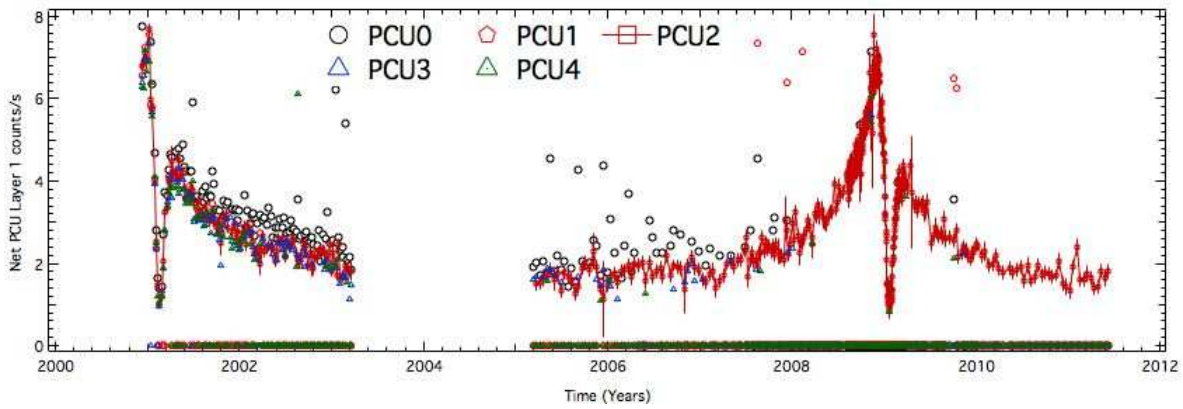

Figure 1.6 The update X-ray (RXTE) light curve of WR 140 from December 2000 to 2011, taken from http://asd.gsfc.nasa.gov.

1.3.1 Observational Evidence of CWB

Due to the high densities and temperatures reached by the shocked material, CWBs (WR+OB) were first proposed to be detected at X-ray energies (Prilutskii & Usov 1976, Cherepashchuk 1976). Pollock (1987) presented X-ray observations with the Einstein Observatory of a sample of 48 WR stars, finding that WR binaries appear significantly brighter than single stars. The high temperatures reached in the shocks are expected to result in hard X-rays emission (1-10 keV), contributing to the soft component from the unshocked stellar winds ($\lesssim$ 1 keV; De Becker 2007). This has been confirmed for several WR binaries: X-ray light curves obtained with EXOSAT for WR 140 (WC7+O4-5; $P = 7.94$ years; see Figure 1.6) indicate anomalous extinction at the time of periastron passage, resulting from the motion of the X-ray source deep into the WR wind (Williams et al. 1990). These authors also determine CNO abundances of the WR wind responsible for the X-ray extinction. Subsequent observations have performed new X-ray studies of this binary, deriving other abundances (Skinner et al. 1995 using ASCA observations), and improving the analysis of the X-ray light curves (Pollock et al. 2005). Similar studies have been performed for γ^2 Vel (WC8+O9I; $P = 78.5$ days) from observations with the satellite ROSAT (Willis et al. 1995), extending the spectrum to energies >2.5 keV with ASCA (Stevens et al. 1996, Rauw et al. 2000), and more recently with Chandra (Skinner et al. 2001, Henley 2005). Another example is the short period system V444 Cyg (WR 139; WN5+O6;P = 4.2 days). Corcoran (1996; from ROSAT observations) found this source to be weaker than predicted, due to the inappropriate assumption of instantaneous terminal wind velocity (Stevens et al. 1992), but nevertheless in agreement with a wind-wind colliding origin for the X-ray emission. Later ASCA observations reinforced this view (Maeda et al. 1998, Pittard 2010).

At Ultraviolet wavelengths (UV), the spectrum is dominated by the strong emission lines from the unshocked wind itself, which makes difficult to disentangle the influence of the interacting region. However, it has been possible to detect its influence over the absorption component of P Cygni profiles, which show a decrease in the blue-shift edge when the WR star is in front. This was interpreted as the WCR being located within the wind acceleration region of the O-star, thus preventing the wind to reach its terminal velocity (St-Louis et al. 1993). Such behavior has also been observed in the UV spectra from IUE observations of γ^2 Vel (St-Louis et

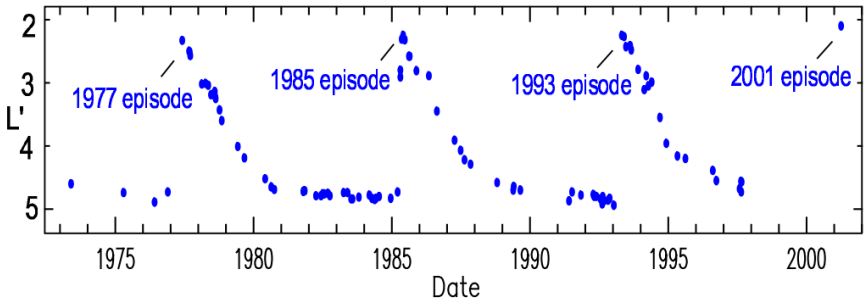

Figure 1.7 Light curve of WR 140 at 3.8 μm, showing dust formation episodes recurring with a period of 7.94 years (Williams 2008).

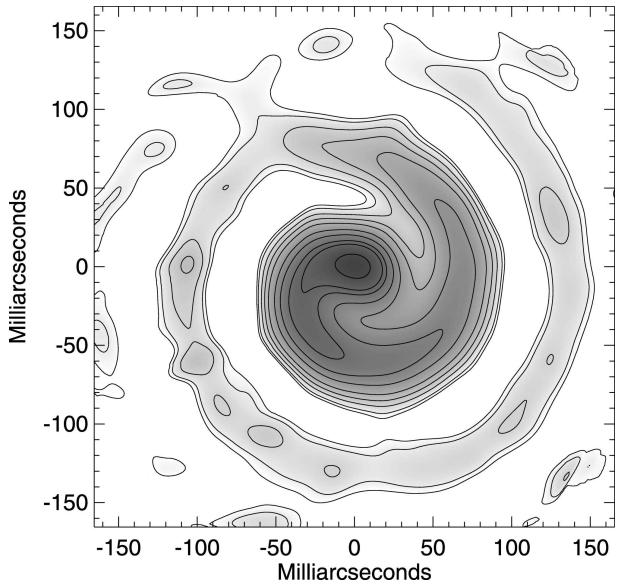

Figure 1.8 WR 104 pinwheel nebulae at 2.3μm taken from Tuthill et al. 2008. Stacked composite image of all epochs presented in this work. Contour levels are 0.1, 0.2, 0.5, 1, 2, 5, 10, 20, 30, and 70% of the peak.

al. 1993), V444 Cyg (Shore & Brown 1988), and WR 140 (Setia Gunawan et al. 2001). Models of the effect of the WCR over the P Cygni profiles actually predict an influence over both the absorption and the emission components of the P Cygni lines (Stevens 1993, Georgiev & Koenigsberger 2004). At optical wavelengths, the variability in the structure of the peak profile of the emission line C III λ5696 for WR 79 (WC7+O6; P = 8.8 days) was explained within a wind-wind interaction context (Lürs 1997). A similar feature in the same line was also observed in the WR 133 spectrum by Underhill & Hill (1996), who discuss colliding winds as a hypothesis to explain the occurrence of such line profile.

Infrared (IR) observations of WR indicate the formation of dust in WCL stars (van der Hucht 2001). Although dust emission has been detected in single WC stars (Williams et al. 1987), the high densities reached at the colliding zone seem to favor the dust formation in WC+OB binaries (Williams 2008). Episodic dust formation associated with the orbital period (P =7.94 year), and coincident with the periastron passage was found for WR 140 (Williams 1990; see Figure 1.7 for an update version this work). A similar behavior has also been found

in systems like WR 48a and WR 137 (Williams et al. 19987). Tuthill et al. (2003) presented images of WR 104 at six epochs, which show rotation of the system with a period ∼243.5 days and with a constant dust formation rate. This is probably a consequence of its circular orbit (with a low inclination angle), and hence a constant separation between the components, in contrast with the high eccentric orbit of WR 140. The spatial distribution of the dust follows that of the high-density material within the interaction region, which is twisted into a spiral structure due to the constant orbital motion (see Figure 1.8). These spiral structures are better known as *pinwheel nebula* and has also been discovered in WR 98a (Monnier et al. 199), and WR 112 (Tuthill et al. 2003).

At radio frequencies, the influence of the wind-wind interacting region has been mainly inferred by the detection of negative and flat ($\alpha \sim 0$) spectral indices. These sources also show high brightness temperatures ($\sim 10^6 - 10^7$ K), in comparison with those expected for thermal stellar winds ($\sim 10^4$ K). This behavior has been associated with the presence of a non-thermal emission component arising from the colliding zone. Variability in both the spectral index and in the radio flux density supports the presence of such an extra component, with periodic maximum in the light curve (e.g. WR 140 see Figure 1.10). The spectra characterization revealed that ∼40% of the WR stars show hints of a non-thermal spectrum (Abbott et al. 1986, Bieging et al. Chapman et al. 1999, Cappa et al. 2004). In the next section we will describe in detail the origin of the non-thermal emission, and other possible effects of the WCR over the radio spectrum of WR stars.

1.3.2 Radio Emission of Colliding Wind Binaries

As we previously described in Section 1.2.1, the stellar winds of WR stars emit free-free thermal emission detectable at radio frequencies and characterized by a positive spectral index, $\alpha \approx 0.6$. However, negative and flat spectral indices, suggesting the presence of non-thermal emission, have also been reported from radio observations. The non-thermal radio emission was proposed to be synchrotron emission produced by relativistic electrons being accelerated either in strong shocks within the stellar wind, for single stars (White 1985), or in a WCR between the stellar components for binary systems (Usov 1992, Eichler & Usov 1993). Recently, Van Loo et al. (2006) demonstrated that the observed non-thermal radio emission from O-stars cannot be explained by current models of internal shocks within a single stellar wind, therefore lending strong support to the binary scenario for the non-thermal radio emission from massive stars (De Becker 2007).

In this way, the total spectrum of these sources is thought to be composed by a thermal component of emission arising from the stellar winds, plus a non-thermal component with a negative spectral index (~ -0.5; Eichler & Usov, 1993; see Figure 1.9). The negative spectral indices observed occurs when the non-thermal component dominates the thermal one, usually at frequencies $\lesssim 8$ GHz (e.g. Chapman et al. 1999). On the other hand, a thermal spectrum is seen when the non-thermal emission is diminished by the free-free absorption of the unshocked winds. Thus, similarly to the X-ray emission, the non-thermal contribution from the WCR is expected to be modulated by the orbital motion, resulting in flux density variability with time-scales of the order of the orbital period (Figure 1.10).

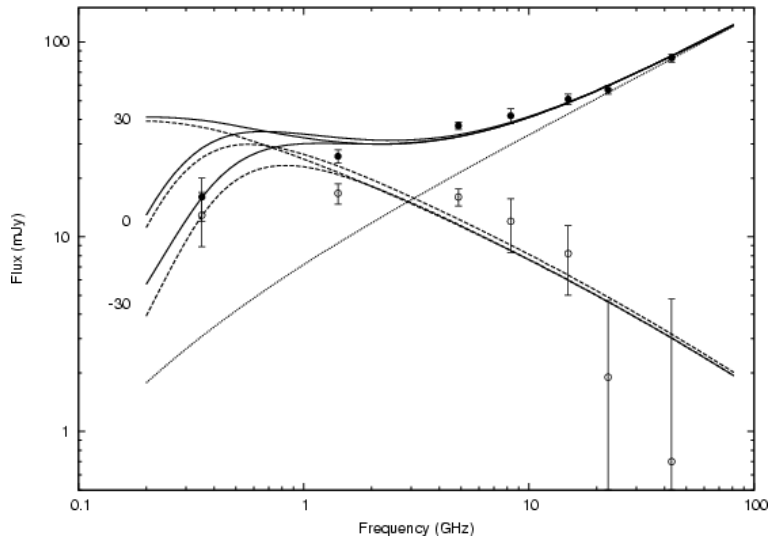

Figure 1.9 Fitted spectrum for WR 147, including total (solid line), synchrotron (dashed line), and thermal (dotted line) flux. The open circles are synchrotron fluxes estimated by subtracting a thermal component to the total observed fluxes (Pittard et al. 2006).

As mentioned above, variability may result from changes in the intrinsic emission and/or absorption effects due to changes in the column density owing to the orbital motion. Thus, the main characteristics of the non-thermal radio emission are:

- Negative and flat spectral indices.
- Brightness temperatures much higher ($\sim 10^6 - 10^7$ K) than that expected for the thermal emission ($\sim 10^4$K).
- Variability in the flux density and/or the spectral index (de Becker 2007).

The binary scenario for the origin of the non-thermal emission has also been confirmed by

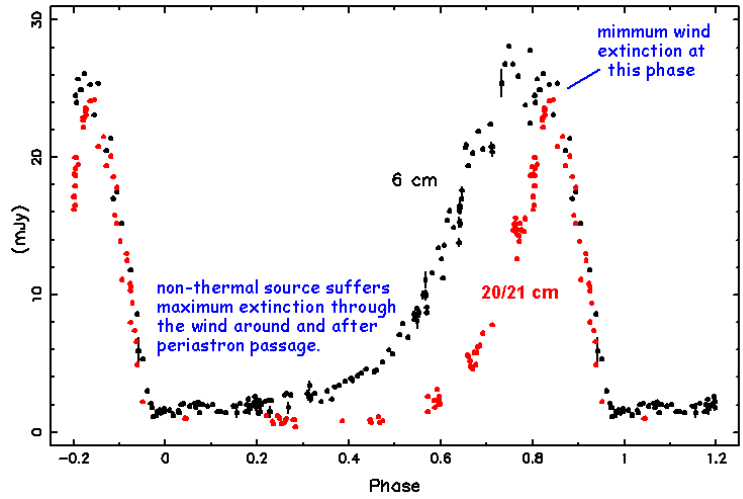

Figure 1.10 Radio light curve of WR 140 at 6 cm and 20 cm. Variability is related to the change of the WCR position with respect to the optically thick region of the WR wind (Credits Peredur Williams; see also Williams et al. 1994)

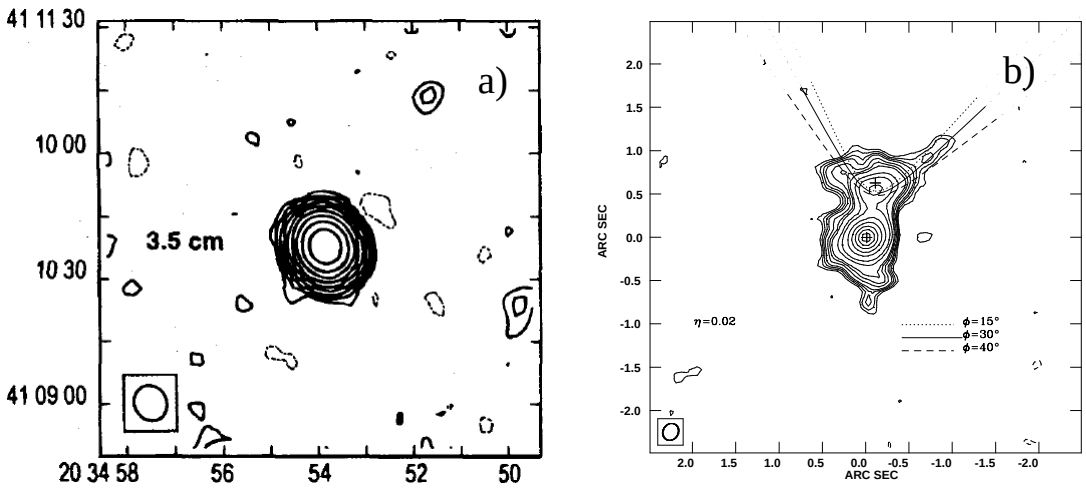

Figure 1.11 Left: VLA (D configuration) at 3.5 with an angular resolution ~ 7" (Contreras & Rodríguez, (1996). Right: VLA (A configuration) at 3.5 cm with an angular resolution $\sim 0.05''$ (Contreras et al. 2004).

radio observations with high angular resolution. For example, Contreras et al. (1996) presented multi-frequency observations of WR 147 using the VLA in its compact configuration, reaching an angular resolution $\sim 7''$ (Figure 1.11-a), and inferred a spectral index $\alpha \approx 0.3$ between 8.4 and 4.8 GHz. Later observations at a higher angular resolution ($\sim 0.06''$; Williams et al. 1997) revealed two sources of emission, one at the south, coincident with the optical position of the WR star, and one non-thermal at ~ 0.6 arcsec to the north, related with the WCR (see also Contreras & Rodriguez 1999 and Contreras et al. 2004). More recently, VLBA observations of WR 140 resolved the WCR (with a resolution $\sim$2 mas; Dougherty et al. 2005), showing a bow-shaped arc that rotates as the orbit progresses.

Dougherty & Williams (2000) examined the radio spectral indices of 23 WR stars to characterize the nature of their radio emission. They noticed that seven of the nine stars with hints of non-thermal emission had an OB star companion. Their results support the hypothesis that a massive companion is a prerequisite for the appearance of non-thermal emission in WR stars. Furthermore, they found that four of the 11 known binary systems examined had a thermal spectrum. These are short period systems with $P \lesssim 1$ year, for which the WCR would be within the opaque region of the stellar wind of the WR star, thus fully absorbing the synchrotron emission from the WCR. These authors presented a plot of the spectral index against the orbital period, which shows that systems whit $P \lesssim 1$ year display a thermal spectrum, and those with longer periods show a non-thermal one (Figure 1.13). This result is consistent with the synchrotron emission being absorbed in short period systems.

Stevens (1995) pointed out that an additional thermal component from the WCR is also expected to contribute to the total spectrum. He investigated the thermal contribution resulting from the hot gas structure created by the wind collision in wide binaries. This contribution is expected to result in an excess of emission which depends on the wind parameters. In the case of comparable winds, the thermal emission can be increased by 50% or more compared to that of

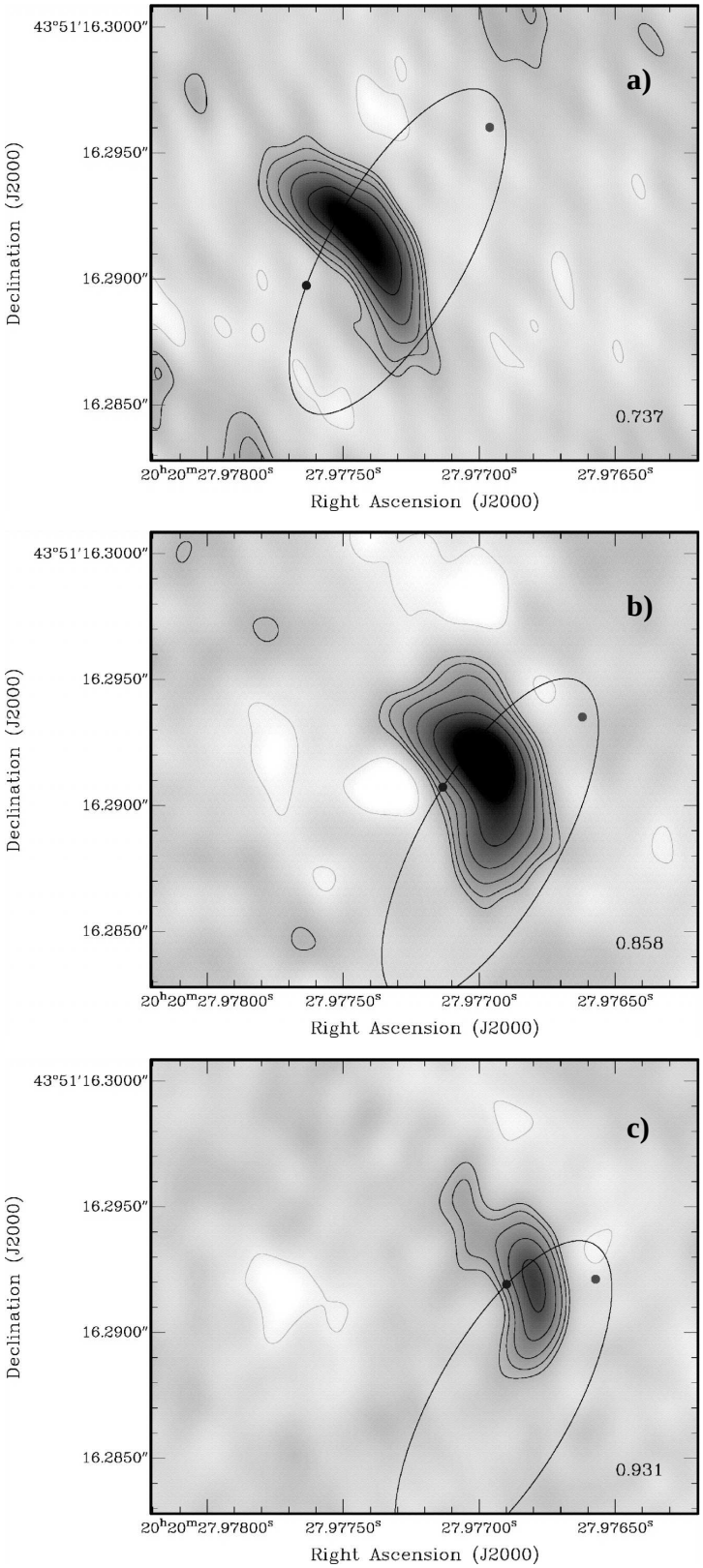

Figure 1.12 Orbit of WR 140 on the plane of the sky with the WCR resolved at orbital phases 0.737 (a), 0.858 (b), and 0.931 (c) overlaid on the VLBA 8.4 GHz images. The WR star is to the west (right) of the WCR at these phases. The proper motion and the rotation of the WCR as the orbit progresses are clearly shown (Dougherty et al. 2005).

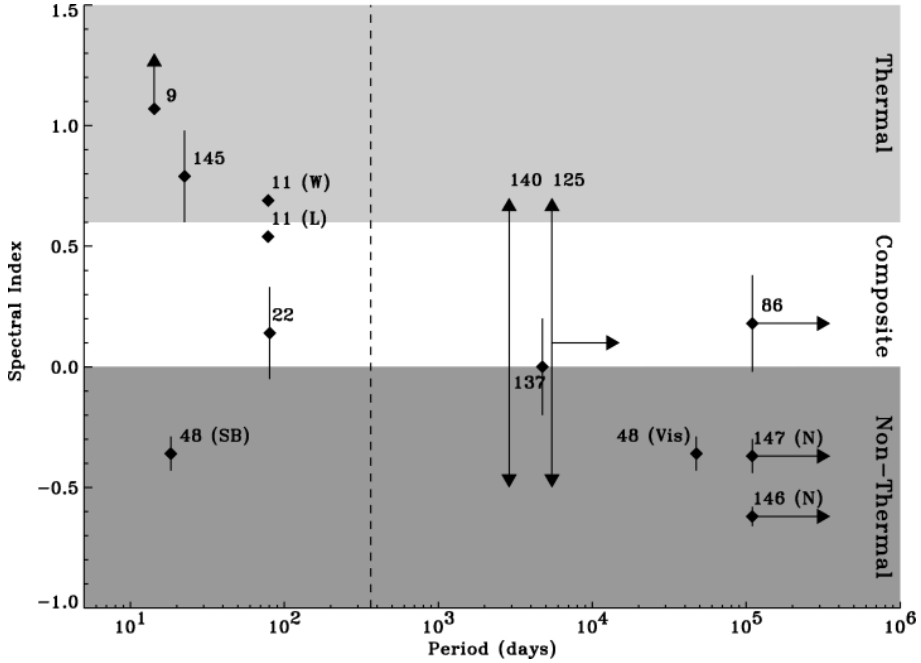

Figure 1.13 Radio spectral index against orbital period for the sample of WR+OB binary systems analyzed by Dougherty & Williams (2000). The two gray-scale regions represent thermal (upper) and non-thermal (lower) values of spectral index, and the white region is the "composite" spectra region. The vertical dash line denotes a period of 1 year. A clear tendency to a thermal spectrum can be seen for the systems with orbital periods $P < 1$ year.

the unshocked winds. This author pointed out that this effect is expected to be higher in close binaries than in wide systems. In summary, the WCR is expected to alter the total spectrum contributing with both non-thermal and thermal emission. The non-thermal emission is expected to be more significant in wide systems, while in close systems the non-thermal emission would be absorbed, and the WCR influence is expected to come from its thermal emission.

1.4 The Physics of Colliding Wind Binaries

The WCR structure that results from the interaction of two stellar winds is formed by two oppositely faced shocks, separated by a contact discontinuity. This is schematically shown in Figure 1.14 for a system with a binary separation D. For two identical winds, the contact discontinuity is a plane equidistant between the two stars, coincident with the surface of momentum balance of the winds. On the other hand, for two unequal winds, the intersection of the contact discontinuity and the line of center of the stars (the stagnation point) can be found using a one-dimensional pressure balance, $\rho_1 \, v_1^2 = \rho_2 \, v_2^2$, where ρ_1 and v_1, and ρ_2 and v_2 are the density and velocity of the stellar winds from the stars 1 and 2 respectively (see Figure 1.14). Assuming that the stellar winds have reached their terminal velocity, the distances to the stagnation point from stars 1 and 2 are given by

$$R_1 = \frac{\eta^{1/2}}{1+\eta^{1/2}} \, D, \qquad R_2 = \frac{1}{1+\eta^{1/2}} \, D \tag{1.26}$$

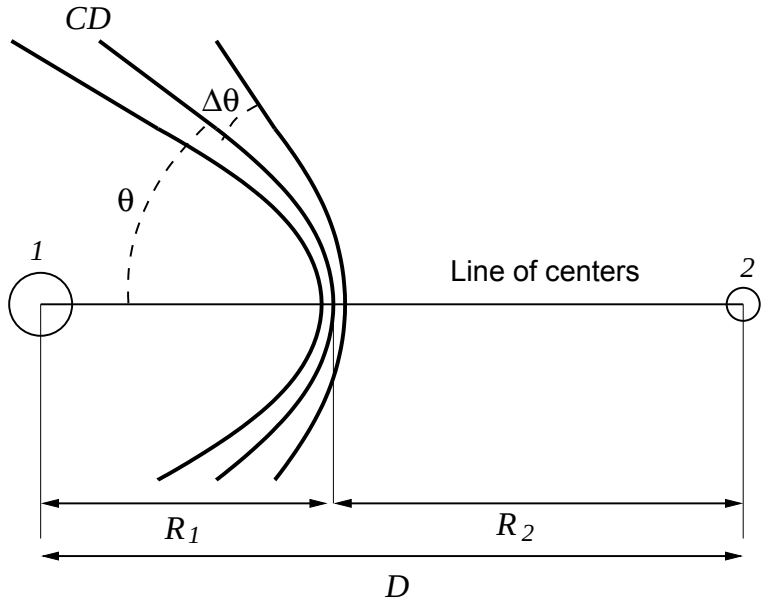

Figure 1.14 Schematic diagram of shocks resulting from the interaction of two stellar winds of stars 1 and 2 separated by a distance D. R_1 and R_2 are the distance to the stagnation point from stars 1 and 2, respectively. θ represents the aperture angle of the bow-shock, and $\Delta\theta$ the angle between the shock front and the contact discontinuity (CD). The line of centers is also represented. For this particular case, the stronger wind is ejected from the star 2.

where $\eta = (\dot{M}_2\, v_2)/(\dot{M}_1\, v_1)$ is the momentum ratio (Eichler & Usov 1993, Stevens et al. 1992). In this case, the contact discontinuity is no longer a plane, but a bow shock facing the star with the weaker wind. The post shock material flows out of the system along the contact discontinuity, straightening it out as a consequence of the centrifugal force of the material (Kallrath 1991). Thus, although in general the shock will straddle the surface of momentum balance, this will be no longer coincident with the contact discontinuity (left panel in Figure 1.15).

The physical conditions of the material within the shocks will depend on the conditions of the preshock wind. We can assume the immediate postshock density, velocity, and temperature to be given by the Rankine-Hugoniot shock conditions for a gas with an adiabatic index $\gamma = 5/3$,

$$\rho_s = 4\rho_w, \quad v_s = v_w/4, \quad T_s = 3\bar{m}\, v_w^2/16\, k, \tag{1.27}$$

where ρ_w and v_w are the density and velocity of the wind, ρ_s and T_s are the density and temperature of the shocked material, and $\bar{m}$ is the average mass per particle (see also Stevens et al. 1992). The stellar winds of massive stars are generally accelerated to terminal winds speed of order of $\sim 10^3\,\mathrm{km\,s^{-1}}$, and their temperatures are regulated by the photospheric temperatures of the stars, typically $\sim (2-4)\times 10^4$ K. Hence, assuming solar abundances ($\bar{m} = 10^{-24}$ g), from equations (1.27) it can be shown that the post shock temperature is of the order of $1.36\times 10^7\, v_3^2\,\mathrm{K}$ ($= 1.17\, v_3^2$ keV) where v_3^2 is the preshock velocity in units of $10^3\,\mathrm{km\,s^{-1}}$. Note that the post shock temperature will be higher for the hydrogen deficient winds of WR stars due to larger values of $\bar{m}$.

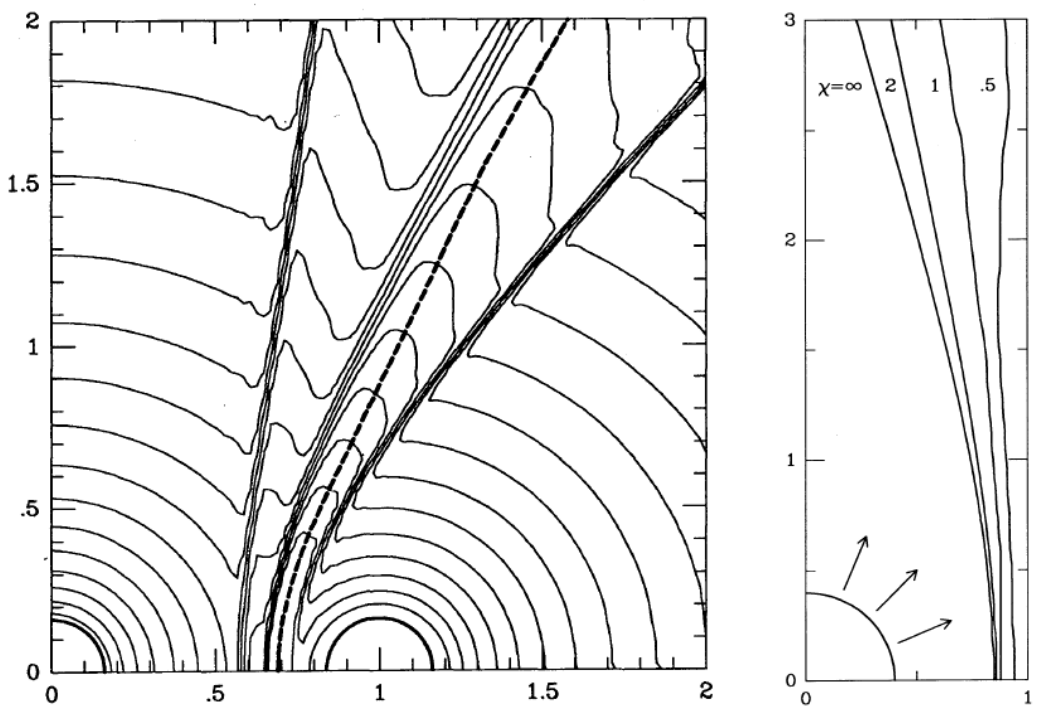

Figure 1.15 Left: Hydrodynamic simulation of two adiabatic colliding winds with $\beta = 0.45$. The heavy dashed line is the surface of momentum balance, and the converging density contour lines in between the two wind shocks are the contact discontinuity in the simulation. Right: Location of the wind shock in a system with two identical stellar winds (i.e. the right-hand wall is a reflecting boundary). The wind properties are held constant, while the separation is changed in order to vary the cooling parameter χ defined in the text. For panels are taken from Stevens et al. (1992).

Radiative Cooling

The post shock material could be radiatively cooled, thus introducing an additional scale length into the system, determined by the cooling time t_{cool} and the flow velocity of the material along the shocked region v_s, $l_{cool} = t_{cool}\, v_s$. In order to quantify the cooling of a system, Stevens et al. (1992) introduced the parameter χ defined as the ratio of the cooling time of the shocked gas to the escape time from the intershock region. The radiative cooling is usually expressed by the cooling function $\Lambda(T)$, which is essentially the energy lost by the material per unit of time, normalized to the number density. Thus, the cooling time is given approximately by

$$t_{cool} = \frac{kT_s}{4\, n_w \Lambda(T_s)}. \tag{1.28}$$

The time-scale for the material to escape from the shocked region near the line of centers can be approximated by

$$t_{esc} = \frac{d}{c_s}, \tag{1.29}$$

where d is the distance from the star to the contact discontinuity and c_s is the postshock sound speed along the line of centers. At the CWBs temperatures, the cooling function $\Lambda(T)$ lies near a local minimum, and we can approximate the function locally with a constant value (see Stevens

et al. 1992). Thus,

$$\chi = \frac{t_{cool}}{t_{esc}} \approx \frac{v_3^4\, d_{12}}{\dot{M}_{-7}}, \tag{1.30}$$

where v_3 is the wind velocity in units of $10^3\,\mathrm{km\,s^{-1}}$, d_{12} is the distance to the contact discontinuity in units of $10^{12}\,\mathrm{cm}$, and $\dot{M}_{-7}$ is the mass loss rate in units of $10^{-7}\,M_{\odot}\mathrm{yr}^{-1}$. The different wind abundances can vary this equation by a factor of order 2. Furthermore, the velocity dependence in this equation is not entirely realistic because the temperature (and hence velocity) dependence of $\Lambda(T)$ is neglected. Typically, v_3 will be between 1 and 2, which is a sufficiently narrow range for this equation to remain valid. The cooling parameter should be considered only as a characteristic measure of the importance of cooling. For systems with unequal winds, the cooling of both shocks at each side of the WCR must be characterized by its corresponding stellar wind parameters. Thus, for

- $\chi \gtrsim 1$ the radiative cooling of the WCR will not be important, and the shock can be consider *adiabatic*.
- $\chi \ll 1$ the radiative cooling is expected to be important, and the shock can be consider *isothermal*, with the shocked material cooled to the preshock temperature of the wind.

In the right panel of Figure 1.15 it can be seen that as the shocks become radiative, the opening angle of the shocks decreases, and the two-shock structure approaches the contact discontinuity. Radiative cooling can also be important in systems for which χ is greater than unity if the wind shocks at a relatively oblique angle. This is due to the fact that in case the total cooling rate increases rapidly shortward of $10^7\,\mathrm{K}$, the postshock cooling time decreases as a high power of the shock velocity for $v_w < 10^3\,\mathrm{km\,s^{-1}}$. Thus, if a stellar wind shocks at an oblique angle such that the normal shock velocity is much less than $10^3\,\mathrm{km\,s^{-1}}$, cooling will be much more important than estimated in equation (1.30), even for $\chi \gg 1$. In practice, the shock becomes oblique as the distance from the line of centers increases, especially for systems with unequal winds, where the shocked region becomes a curved surface instead of a plane.

Radiative Systems

From equation (1.30) we see that $\chi \propto d$, and consequently it is proportional to the binary separation D, and to the orbital period as $\chi \propto P^{2/3}$. Thus, for fixed the stellar wind parameters,*the shorter the period, the more radiative the shocked region will be.* However, the precise point at which systems change over from being radiative to adiabatic depends strongly on the other wind parameters (i.e. $\dot{M}$ and v_w). Thus, since the winds of WR stars are typically an order of magnitude denser,*WR binaries will generally be radiative for shorter periods than O-type systems.* Recently, Parkin & Pittard (2008) studied the dependence of χ with the orbital period for two set of parameters corresponding to an O+O and a WR+O system, using two-dimensional hydrodynamical simulations. They found that the O+O system are largely adiabatic even down to an orbital period of 10 days (for shorter period systems, the stars are close enough that acceleration/deceleration of the winds needs to be considered). On the other hand, for the WR+O system, the cooling is important for orbital periods $\lesssim 1$ year and up to several years if the WR star is a WC subtype, since the cooling is more important for such abundances.

1.4.1 Non-thermal Radio Emission

The strong shocks resulting from the interaction between the two ionized stellar winds in CWBs are expected to accelerate charged particles to high energies. When the particles reach relativistic energies, their interaction with the magnetic field of the stars results in *synchrotron emission* detectable at radio frequencies. The particles within the WCR are expected to be accelerated trough the *Diffusive Shock Acceleration* (DSA) mechanism (the first order Fermi acceleration mechanism; e.g. Blandford & Eichler 1987). For strong shocks ($\rho_w \ll \rho_s$) , which is a good approximation for the shocks in CWBs, the DSA predicts a power-law energy distribution for the relativistic particles

$$N(E) \propto E^{-p}, \tag{1.31}$$

with an electron index $p \approx 2$. This mechanism is believed to be also responsible for the production of cosmic rays, probably at least partly accelerated in supernova remnants (de Becker 2007). For a power law distribution of electrons, the radiation flux at a frequency ν is given by (Rybicki & Ligthman 1979)

$$S_\nu \propto \nu^{-(p-1)/2}. \tag{1.32}$$

Thus, the spectral index for the intrinsic synchrotron emission from CWBs will be $\alpha \approx -0.5$.

The intrinsic non-thermal emission is expected to be affected by several absorption processes that will change the resulting shape of the non-thermal spectrum. The combined action of the free-free absorption from the surrounding material, the Razin effect due to the surrounding plasma reducing the energy of the relativistic particles, and the synchrotron self-absorption are the responsible for the low frequency absorption[1] (see Figure 1.9; detailed models can be found in Dougherty & Pittard 2003). Thus, the non-thermal flux density is expected to grow with frequency from a turn-over frequency (likely to occur at a fraction of GHz in the case of wide systems; De Becker 2007) before reaching a maximum at a frequency of the order of a few GHz. The turn-over frequency, and hence the maximum, is strongly dependent on the absorption process and the physical parameters of the system that is considered. Recent models and observations seem to favor free-free absorption as the dominant absorption factor, at least in the case of WR 140 (De Becker et al. 2007b).

Non-thermal Systems

The observational properties of the non-thermal emission depend on the grade of absorption that it is suffering. Hereinafter we will consider the free-free opacity as the dominant absorption mechanism in the system. As we described in Section 1.2.1, the stellar winds become opaque at a characteristic radius R_ν described by equation (1.25). In WR+OB systems the main source of absorption is expected to come from the WR stellar wind (denser than the OB wind), and hence, the observational properties of the non-thermal wind will depend on the ratio between the radio photosphere of the WR and the distance from the star to the WCR, $R_{\nu,WR}/(R_2) \approx R_{\nu,WR}/D$. In other words, it depends on the fact that the WCR lies or not within the opaque region of the

[1]Inverse Compton scattering may contribute to the cooling of the relativistic particles in the WCR, affecting the spectrum at high frequencies (X-ray and γ-ray energies; see Pittard et al. 2006 for details).

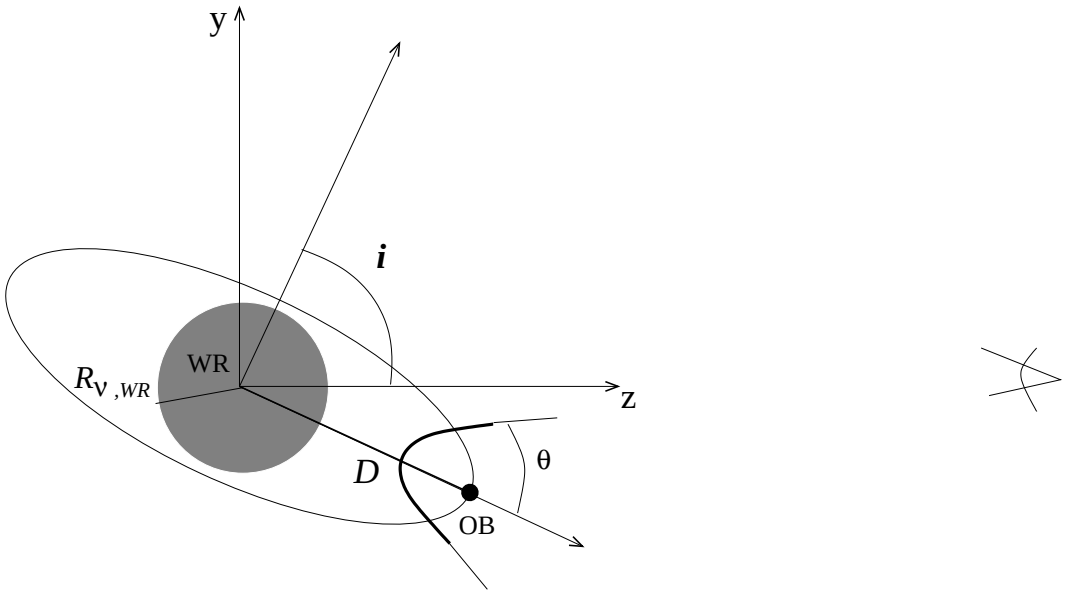

Figure 1.16 Schematic diagram of a systems with an inclinations angle i. The WR and O stars separated by the distance D are represented. The gray region represents the radio photosphere of the WR star with a radius $R_{\nu,WR}$.

WR stellar wind (Eichler & Usov 1993, Dougherty & Williams 2000).

Let's Consider the case of a circular orbit,

- For $R_{\nu,WR}/D \ll 1$, the WCR lies out of the optically thick region of the WR wind and the observational properties of the non-thermal emission will be now dependent on the inclination of the orbit defined by the angle i (see Figure 1.16). If the angle between the line of sight and the orbital plane $(\pi/2 - i)$ is small enough, the flux of non-thermal radio emission will be modulated because of the eclipse of the WCR by the stellar winds. Otherwise, the non-thermal flux practically does not vary if the gas outflow from the WR and OB stars remains stationary.

- For $R_{\nu,WR}/D \gtrsim 1$, the WCR is inside the radius of the radio photosphere of the WR star. Thus, the non-thermal source may be observed at the frequency ν only if the time scale at which the outflow from the stellar winds reach the radio photosphere of the WR stars, $R_{\nu,WR}/v_{\infty,WR}$, is smaller than the time necessary for the WR+OB binary to turn on the angle of aperture of the bowshock, which could be approximated by $2\theta + \Delta\theta \simeq 3\theta$ (see Figure 1.14)

$$\frac{R_{\nu,WR}}{v_{\infty,WR}} \lesssim \frac{3\theta}{2\pi} P \tag{1.33}$$

  or $P \gtrsim P_{cr}$, where $P_{cr} = (2\pi/3\theta)(R_{\nu,WR}/v_{\infty,WR})$. Thus, the shorter the period of the system is, the higher the frequency at which the non-thermal emission could escape the free-free absorption will be. This can also be understood as a consequence of the inverse dependence of $R_{\nu,WR}$ with frequency, which at some frequency may become smaller than the distance from the WR star to the WCR (R_2).

In the later case, for typical values of a WR+OB system, the value of P_{cr} is of order of a month

when the observing frequency is a few GHz. Thus, if $P < P_{cr}$ the non-thermal radio emission from the WCR will be almost completely absorbed by the WR wind. On the other hand, in the case of $P \gtrsim P_{cr}$, the non-thermal emission may be detected if the angle between the line of sight and the orbital plane $(\pi/2 - i)$ is smaller than $3\theta/2$. Finally, if the orbital eccentricity of the WR+OB binary is high, the radios $R_{\nu,WR}/R_2$ and $R_{\nu,WR}/R_2$ vary along the orbit. Thus, the WR binary changes from one kind of non-thermal radio source to another as consequence of the orbital motion (see Eichler & Usov 1993 for details).

1.4.2 Thermal Radio Emission

Stevens (1995) investigated the effect of the binarity on the thermal radio emission from massive binary systems. In their studies, they only considered wide and adiabatic systems. They found that besides the non-thermal, free-free thermal emission can also contribute significantly to the total radio emission of the system.

In Figure 1.17 of Stevens (1995), he showed a comparison between a single stellar wind model and a binary model for a variety of parameters related to thermal radio emission. For the stellar winds, he made the same assumptions we did in Section 1.2.1: spherical symmetric, steady, and isothermal winds. The parameters assumed for the model correspond to an O+O-type system and are given in the figure.

- *The density and temperature profiles* show an enhancement in both density ($4\,n_w$) and temperature ($T_s \sim$ few times 10^7 K; see equations [1.27]), at the position corresponding to the WCR (which lies along the z-axis at $\sim 10^{14}$ cm).

- For *the optical depth profiles*, the hot region is effectively transparent to free-free emission ($\kappa_\nu \propto T^{-1.35}$; equation [1.18]), which results in a small plateau centered at the WCR position. Thus, even when the density increases in the WCR, the integrated optical depth, $\tau(q)$, is usually lower in the binary case than in the single star case, due to the hot shocked material.

- *The integrand of the intensity of emission* (which integrated with respect to z gives the intensity of the emission as a function of the impact parameter q, $I(q)$), shows that in the binary case, hot shocked gas shows some enhancement of the emission, indicating that *the hot gas within the WCR will make a non-negligible contribution to the radio flux.*

The total thermal radio flux for this model at $\nu = 15$ GHz is $S_\nu = 1.12$ mJy for the single star case, and $S_\nu = 1.24$ mJy for the binary case. This represents only an increase of around 10% for the binary flux compared to the single star case. In contrast, the effect of having two winds instead of just a single one was also quantified, finding an increase of around a 50% in the case of two equal winds. On the other hand, Stevens (1995) also calculated the thermal emission for a WR+O binary, pointing out that a major effect is observed for stars with different wind abundances. Furthermore, he also found variability related to the relative position of the stars (by comparing the emission at two orbital phases, 0.0 with WR star in front, and 0.5 with O star in front), with the binary effect being diminishing when the dense WR wind is in facing the observer due to the absorption of the emission from the O star and the WCR .

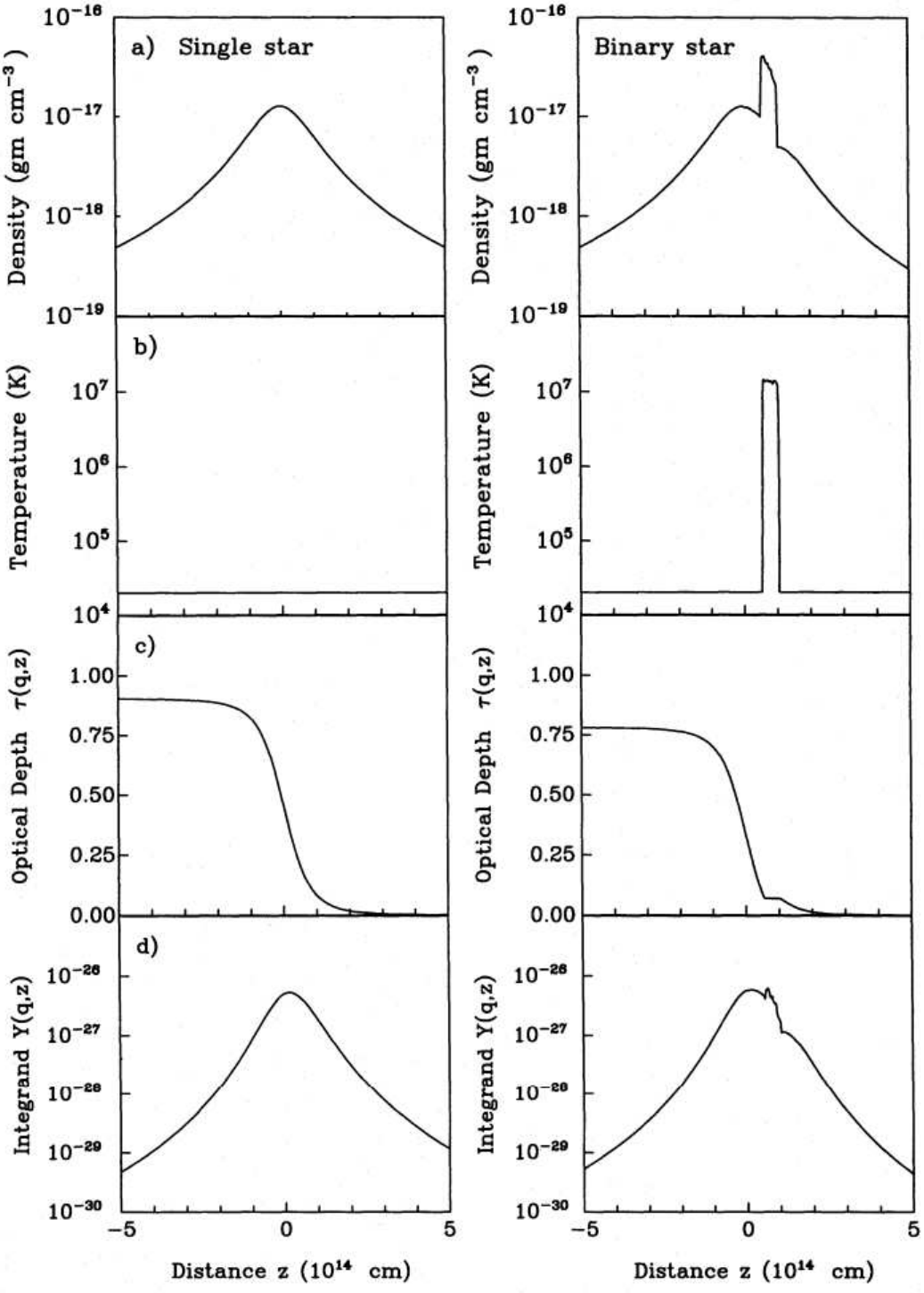

Figure 1.17 Comparison between results for a single stellar wind model and a CWB model. The results are all shown for an impact parameter $q = 10^4$ cm and are plotted as a function of z, and are cross sections through the wind. The results in the left hand column are for a single star with $\dot{M}_1 = 5 \times 10^{-6}\,\mathrm{M_\odot yr^{-1}}$ and $v_1 = 2000\,\mathrm{km\,s^{-1}}$, while the right-hand column is for a binary model with $\dot{M}_1 = 5 \times 10^{-6}\,\mathrm{M_\odot yr^{-1}}$, $\dot{M}_2 = 2 \times 10^{-6}\,\mathrm{M_\odot yr^{-1}}$ and $v_1 = v_2 = 2000\,\mathrm{km\,s^{-1}}$. In both models a temperature $T_w = 2 \times 10^4\,\mathrm{K}$ was assumed for the stellar winds. (a) The density profile $\rho(q, z)$; (b) the temperature profile $T(q, z)$; (c) the free-free optical depth $\tau(z, q)$;(d) the intensity integrand defined as $Y(q, z) = B_\nu[T(q, z)]\, e^{\tau(z,q)}\, \kappa_\nu$, where κ_ν is defined by equation (1.18).

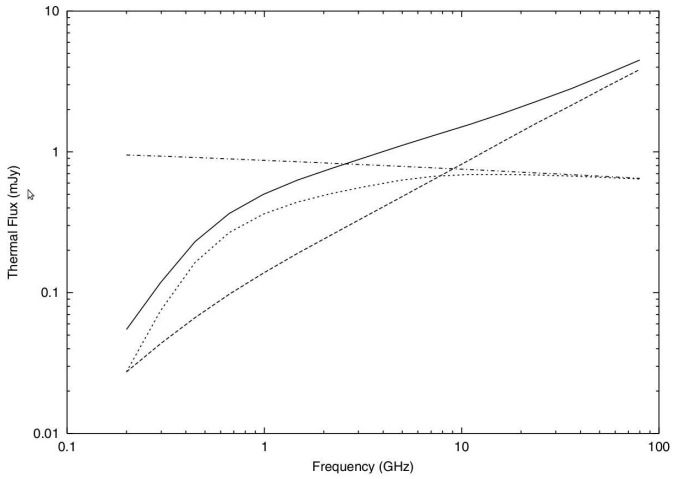

Figure 1.18 The thermal spectrum for a WR+O binary with a binary separation of 2×10^{14} cm, and a viewing angle corresponding to an inclination angle $i = 0$ in Figure 1.16. The thermal emission from the unshocked winds (dashed), the WCR (dotted), and the total thermal emission (solid) are shown. The intrinsic thermal emission from the WCR (before free-free absorption) is shown by the dot-dashed line (Pittard et al. 2006).

The Adiabatic Case

Pittard et al. (2006) investigated the relative contribution of the WCR to the total thermal spectrum of an adiabatic WR+O system (Figure 1.18). They found that the WCR component was consistent with optically thin thermal emission with a spectral index ~ -0.1, in contrast with the component from the unshocked winds corresponding to a standard wind spectrum ($\alpha \sim 0.6$). The intrinsic thermal emission from the WCR is affected by free-free absorption from the unshocked winds, diminishing its contribution at low frequencies. Pittard et al. (2006) found that a substantial fraction of this emission can be observed at certain viewing angles, and pointed out that a *composite-like spectrum (thermal plus non-thermal), often presumed to be evidence for non-thermal emission, can result entirely from thermal processes* (Figure 1.18).

Furthermore, it was also found that the thermal emission from the WCR increases as the binary separation (D) decreases, while the thermal emission from the unshocked winds remains broadly the same. Since the free-free emissivity depends on density (see equation [1.12]) as $\varepsilon_\nu \propto \rho^2 \propto D^{-4}$ and the volume of the WCR scales as D^{-3}, *the thermal emission from the WCR is expected to scale as* D^{-1}. As in the case of the non-thermal, the thermal contribution depends on the WCR position with respect to the radio-photosphere of the WR wind. At wide separations, when the WCR is outside the WR radio-photosphere, its intrinsic thermal emission may become negligible, since it scales as D^{-1}. On the other hand, Pittard et al (2006) found that in closer systems, with the WCR being within the radio-photosphere of each wind, it may remove part of the wind material, and hence, a segment of their emission. However, the resulting reduction in flux from the unshocked winds may become more than compensated by the increase in thermal emission from the WCR. Therefore, the total thermal emission can considerably exceed that expected from the two stellar winds. The excess could be considerably higher at smaller separations and lower frequencies.

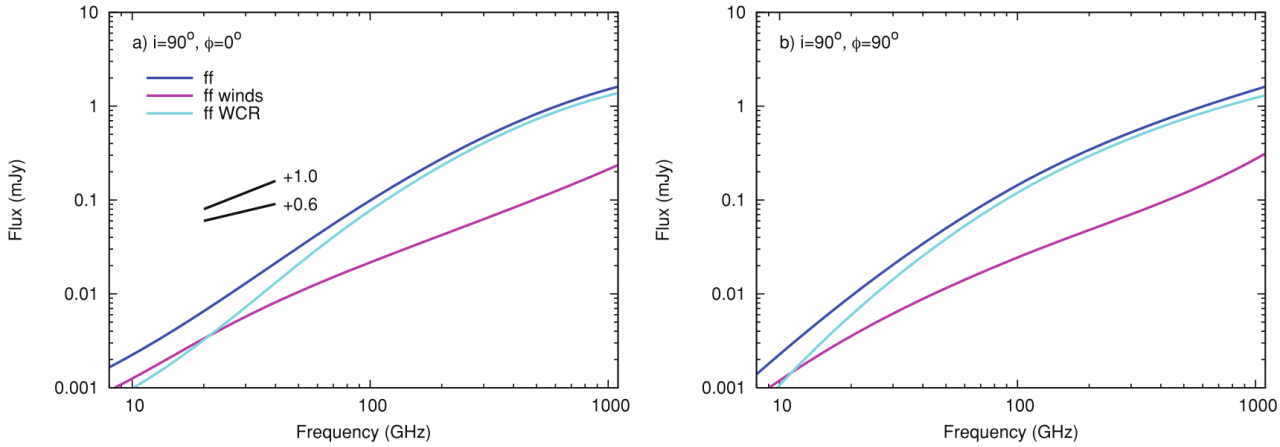

Figure 1.19 Free-free thermal radio spectra for the radiative ($\chi \sim 0.34$) O+O type system modeled by Pittard (2010). Panel (a) $i = 90°$, $\phi = 0°$ and (b) $i = 90°$, $\phi = 90°$. In each case, the contributions of free-free emission from the unshocked winds and the WCR to the total thermal emission are shown. There is likely a significant loss of flux in the models at the lowest frequencies due to the finite size of the numerical grid (Pittard 2010).

The Radiative Case

More recently, Pittard (2010) investigated the thermal emission from centimeter to sum-millimeter wavelengths for close O+O type binaries (orbital periods $P \sim$days). He found that *the thermal emission from the WCR is strongly dependent on its density and temperature, being optically thick in radiative systems and optically thin in adiabatic systems.* As we see from equation (1.30), the cooling is expected to be more efficient as the stars become closer. Furthermore, when the winds collide at only a fraction of their terminal velocities, lower postshock temperatures and higher post-shock densities result, favoring the radiative cooling of the postshock material. This is the case of one of his models, for which the WCR occurs near the star within their accelerating wind region (the parameters assumed were $\dot{M} = 2 \times 10^{-7}\,\mathrm{M_\odot yr^{-1}}$ and $v_s = 730\,\mathrm{km\,s^{-1}}$ for the mass-loss rate and velocity of the winds at the stagnation point, respectively, and an orbital period $P = 3$ days). They investigated the spectrum and its variability as a function of the orbital phase for several inclination angles of the orbit (i). Figures 1.19 and 1.20 illustrate the results found for this radiative system ($\chi \sim 0.34$). *The thermal emission from the WCR regions was found to be optically thick with a spectral index higher than the 0.6 expected for a single wind, reaching values of* ~ 1.5 *between 100 and 250 GHz* (at $i = 90°$ and $\phi = 0°$ corresponding to an orbital phase 0.0; where ϕ is defined as an azimuthal viewing angle). Figure 1.20 shows flux density variability due to the WCR thermal contribution changing along the orbit. The light-curves show symmetry about the orbital phases corresponding to both stars aligned with the line of sight (0.0, 0.5; conjunction), and in quadratures (0.25, 0.75). Slightly deviations for the maximum and minimum of emission can be seen respectively for both star configurations, owing to hydrodynamical instabilities or/and orbital effects expected for such close systems. This study was focused on O+O-type binaries, and, although the behavior of the emission is not expected to change significantly, it is not straight forward to predict how these results would scale to WR+OB systems. For example, the differences between the conditions for an effec-

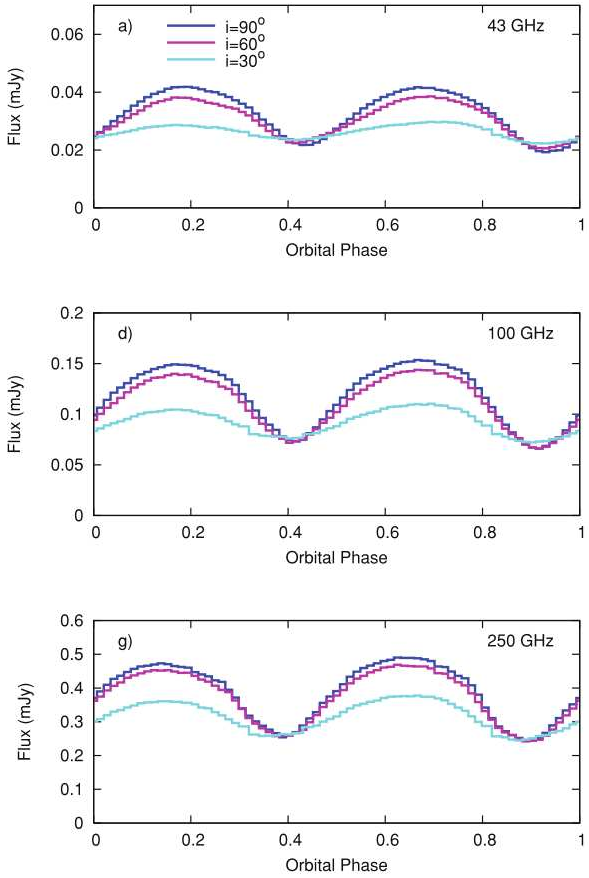

Figure 1.20 Radio light curves of the total thermal emission from a radiative system (parameters are given in the text) at 43 (top), 100, and 250 GHz (bottom) for inclination angles $i = 30°$, $60°$, and $90°$. In all the cases the observer is located along a direction vector specified by $\phi = 0°$. The stars are at conjunction at phases 0.0 and 0.5, and quadrature at phases 0.25 and 0.75. Note that the flux scales are different in each panel. (Pittard 2010).

tive radiative cooling and the relative sizes of the radio photospheres may change the observing properties of WR binaries (Pittard 2010).

1.5 Motivation, Methodology and Thesis Outline

As discussed in previous sections, radio observations have been very successful in the detection and characterization of the emission from stellar winds in WR stars. Radio observations have not only allowed the study of the stellar wind itself, but also the study of the structures resulting from the wind-wind interaction in WR+OB binary systems. The combination of observational and theoretical efforts have also allowed to constrain and derive both stellar and orbital parameters from the study of the WCR emission. Up to now such studies have been focused on the non-thermal component of emission in wide binary systems. However, as discussed above, such non-thermal component is unlikely to be detected in close binaries with orbital periods $P \lesssim 1$ year. In contrast, theoretical studies indicate that thermal emission from the WCR may also contribute significantly to the observed spectrum, being more important for such close systems. Moreover,

this thermal contribution is expected to affect at different wavelength ranges depending on the physical conditions of the shocked material. Thus, by studying the thermal component it is possible to obtain the physical parameters in the shocked material even for close binary systems. However, at the moment there are no observational studies addressed to the detection of the thermal WCR component. In addition, it is also important to either discard, or corroborate, the detection of a non-thermal component in close systems.

The main goal of this thesis is the detailed study of the WCR in the global spectrum of close WR systems. In order to reach this goal, we present both, the development of a semi-analytical model aimed to quantify the thermal contribution from a radiative WCR, and an observational study of a sample of WR stars, covering the radio spectrum from centimeter to millimeter wavelengths. Thus, this thesis is divided in two main chapters where we present our results from both studies. In Chapter 2, we present a semi-analytic model that allows to quantify the free-free thermal radio emission from radiative WCR within a binary system. We discuss and compare our results with observations of WR stars; in particular, we apply the model to one of the WR stars of our sample. In Chapter 3, we present observations of a small sample of 14 WR stars, covering a wide frequency range, from 1.4 to 250 GHz. Two of these stars were also observed with the GMRT at 1.4 GHz, 13 stars with the VLA at 4.8, 8.4, and 23 GHz, and six with the IRAM 30 m telescope at 250 GHz. We combine our observations in order to search for a potential variability.We discuss the properties of the spectrum in a binary context ascertaining whether a WCR is compatible with the spectrum found for each source. In particular we look for observational evidence that allow us to confirm the theoretical results presented in Chapter 2. Finally, we present a discussion of our results in a general context, pointing out the importance of properly characterize the spectrum and discern between its different contributions for this kind of stars.

2

Thermal Radio Emission from Radiative Shocks in Colliding Stellar Winds

In massive binary systems, the interaction of the strong stellar winds results in a wind-wind collision region (WCR) between the stars. Such WCR is expected to contribute to the total radio emission with a non-thermal and/or a thermal component, which may modify the expected spectrum from a single stellar wind. In close systems, the free-free thermal contribution from the WCR may become significant, being highly dependent on the physical conditions of the shocked material. In this chapter we present a semi-analytic model for computing the free-free thermal radio-continuum emission from radiative shocks within colliding wind binaries (CWBs). Assuming that the WCR is composed of two isothermal shocks (thin-shell approximation), which is expected to occur in highly radiative systems, we obtain the emission measure of the shell. Then, we compute the total optical depth along each line of sight to obtain the total thermal emission for the system. We find that the emission from the shocks arises mainly from the optically thick material, with the flux density increasing with frequency as $\nu^{1.1}$, and scaling with the binary separation as $D^{4/5}$. We compare our results with the radio spectra obtained from observations of WR systems. In particular, we apply the model to the binary system WR 98 and compare our results with observations of this source. Finally, we point out the relevance of taking into account this contribution for the correct interpretation of the observations, and the accuracy of the parameters derived from them.

2.1 Introduction

Massive stars of OB and Wolf-Rayet (WR) spectral types lose a great amount of mass in form of strong stellar winds (with $\dot{M} \sim [10^{-5} - 10^{-6}]\,\mathrm{M_\odot\,yr^{-1}}$ and $v_\infty \sim 10^3\,\mathrm{km\,s^{-1}}$). These winds form a dense, expanding envelope that is ionized by the hot central star, which emits free-free thermal emission detectable from centimeter up to millimeter wavelengths (for example Abbott et al. 1986, Leitherer et al. 1991, Contreras et al. 1996). Under the assumptions of a spherically symmetric, isothermal and stationary wind, the flux density at radio frequencies was found to grow with frequency with a spectral index $\alpha \approx 0.6$ ($S_\nu \propto \nu^\alpha$; Panagia & Felli 1975; Wright &

Barlow 1975; hereinafter this wind is referred as standard wind).

Observational studies have confirmed the thermal growing spectrum expected for stellar winds; however, spectral indices with negative, flat (~ 0.0), and steeper (> 0.6) values have also been found (for example Abbott et al. 1986, Leitherer et al. 1995, Chapman et al. 1999, Montes et al. 2009). Spectral indices higher than 0.6 have been mainly explained as result of deviations in the wind conditions from those assumed for the standard wind. In particular, shock structures resulting from changes in the wind parameters (González & Cantó 2008), and/or clumps affecting the ionization state at the regions where the radio emission is produced (Leitherer & Roberts 1991, Nugis et al. 1998) may result in such high spectral index values. On the other hand, negative and flat spectral indices have been related to a non-thermal component of emission arising from a wind-wind collision region (WCR) between the stars in binary systems (Eichler & Usov 1993). Thus, the detection of a non-thermal spectrum seems to be closely related to the binary condition of the star (Dougherty & Williams 2000, and Van Loo et al. 2006).

Dougherty & Williams (2000) found that WR binaries with orbital periods $P \lesssim 1$ year exhibit a thermal spectrum, and those with longer periods are usually non-thermal sources. For such close binary systems, the WCR lies within the optically thick region of the winds, and hence, the non-thermal emission is diminished by the free-free absorption of the winds. Thus, in these systems, only the free-free thermal emission from the unshocked winds is expected to be detected. Nevertheless, theoretical studies suggest that the free-free thermal emission from the WCR may also affect the total radio spectrum, being more important as the stars become closer (Steven 1995, Pittard et al. 2006, Pittard 2010). Thus, in close binaries, where the non-thermal emission is expected to be absorbed, its binarity may also impact the spectrum, this time from entirely thermal processes.

Stevens (1995) investigated the effect of binarity on the thermal radio emission from O and WR-type binary systems. He found that for wide binaries, the increase of density and temperature of the gas within the shocks of the WCR may increase the total thermal radio emission up to $\sim 50\,\%$ that of a single star. Stevens also pointed out that the WCR contribution may play an even more significantly role in close systems. Pittard et al. (2006) carried out numerical simulations for computing the thermal radio emission from an adiabatic WCR in a specific colliding wind binary. They found that the thermal contribution from the WCR clearly affects the total spectrum. The hot gas within the WCR was found to be optically thin, with an intrinsic emission of spectral index ~ -0.1. These authors also investigated the dependence of the flux density from the WCR with the binary separation, D, and found that it scales as D^{-1}. As a consequence, they remark that a composite-like spectrum (thermal plus non-thermal emission), often interpreted as evidence of a non-thermal contribution, can result entirely from thermal processes. More recently, Pittard (2010) investigated the thermal emission from a highly radiative WCR in an O+O type system, and analyzed its spectrum from radio to submillimeter wavelengths (see also Pittard 2009). He found that for such radiative systems the thermal emission remains optically thick with spectral indices up to $\sim$1.5 at frequencies between 100 and 250 GHz. In this way, the spectrum and the relative significance of the thermal WCR contribution to the unshocked wind emission, are expected to be highly dependent on the physical conditions of the material within the WCR (Pittard 2010). Such conditions are

determined by the nature of the shocks forming the WCR, being either adiabatic or highly radiative, and that depends as well on the stellar wind and the orbital parameters of the system (Stevens et al. 1992).

Cantó et al. (1996) developed a formalism based on linear and angular momentum conservation for solving steady thin-shell problems, which is applicable to the interaction of two non-accelerated flows. In particular, these authors found analytic solutions for the case of two colliding isotropic stellar winds. Assuming that the postshock fluid is well mixed across the contact discontinuity formed between the shocks that bound the WCR, they obtained the shape of the thin shell, its mass surface density, and the velocity along the layer. In other work, Cantó et al. (2005) presented a model for calculating the emission measure from thin-shell flow problems. In particular, these authors applied the results obtained by Wilkin (1996; 2000) and Cantó et al. (1996) for a stellar wind interacting with an impinging ambient flow with a density stratification.

In this chapter, we study the interaction of two spherically symmetric stellar winds. Following the formalism developed by Cantó et al. (1996), (2005), we present a semi-analytical model for calculating the free-free emission from a radiative WCR in binary systems, from which the total thermal spectrum of the binary can be obtained. In Section 2.2, we present the model. In section 2.3, we analyze the behavior of the emission for the particular case of a binary system with two identical stellar winds. The dependence of the spectrum with the binary separation and the stellar wind parameters is investigated in Section 2.4. We establish the restrictions and applicability of the model to real systems in Section 2.5. In Section 2.6, we apply our model to the binary system WR 98 comparing with centimeter and millimeter observations reported for this source. Finally, we present the summary and conclusions in Section 2.7.

2.2 The Analytical Model

2.2.1 The Two-Wind Interaction Problem

In massive binary systems the two powerful stellar winds interact to form a two-shock wave structure between the stars (Stevens et al. 1992, Eichler & Usov 1993). The shocked gas is heated to high temperatures ($10^6 - 10^7$ K), and flows along the WCR near the contact surface between the shocks. The physical conditions of the material within the WCR can be inferred by the nature of the shocks, which can be quantified from the cooling parameter, defined as the ratio of the cooling time of the shocked gas to the escape time from the intershock region,

$$\chi \approx 0.15 \left[\frac{v_w}{10^3\,\mathrm{km\,s^{-1}}}\right]^4 \left[\frac{d}{1\,\mathrm{AU}}\right] \left[\frac{\dot{M}_w}{10^{-5}\,\mathrm{M_\odot\,yr^{-1}}}\right]^{-1}, \tag{2.1}$$

where v_w and $\dot{M}_w$ are the velocity and mass loss rate of the wind, respectively, and d is the distance from the star to the shock front (Stevens et al. 1992; see Section 1.4). In this way, for $\chi \geq 1$, the postshock flow can be assumed to be adiabatic, while for $\chi \ll 1$ it is highly radiative. For systems with different stellar winds, the nature of the shocks that confine the WCR will be determined by the flow parameters of each component.

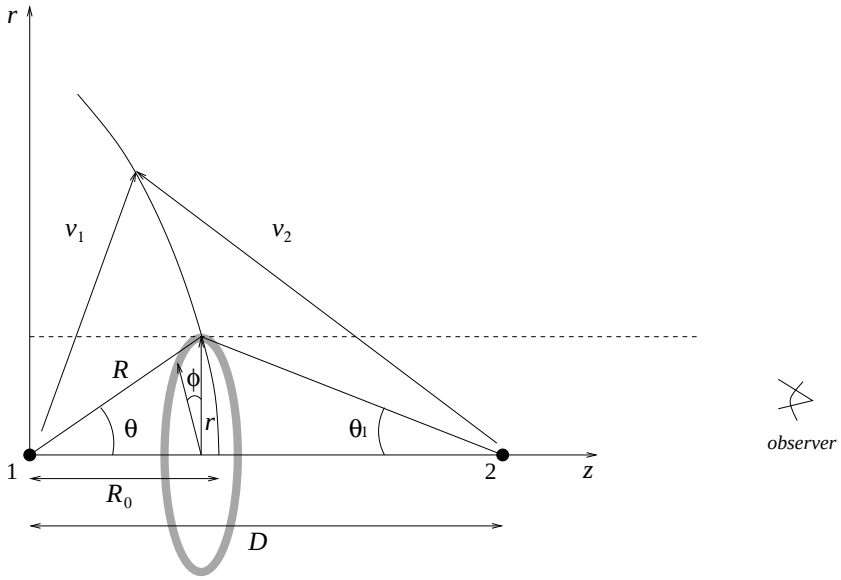

Figure 2.1 Schematic diagram showing the interaction of two spherical winds that move radially away from the stars. The wind source 1 with velocity v_1 is located at the origin of the coordinate system, and the second wind source 2 with velocity v_2 at a distance D along the symmetry axis. The shape of the layer where the winds collide (at R_0 along the symmetry axis) is given by the curve $R(\theta)$. The angles θ and θ_1 are measured from the positions of the stars to the intersection point between a line of sight, with impact parameter r, and the layer. We assume cylindrical symmetry (no dependence on angle ϕ). The observer is located in the orbital plane along the z-axis of symmetry.

When the shocks are highly radiative, the shocks structure collapses onto the contact surface, forming a thin shell confined by two isothermal shocks (see Stevens et al. 1992; Figure 1.15). The shape of the shell can then be approximated by the surface of momentum balance between the winds. An analytic solution for the two-wind interaction problem under the thin-shell approximation was obtained by Cantó et al. (1996). Here, we derive the solution for the shape and the physical properties of the shell, based on the analysis presented by these authors.

Let us consider two steady, hypersonic, and spherical winds, which collide, forming a thin shell composed of two radiative shocks, which may in principle be separated by a contact discontinuity. This situation is shown schematically in the diagram of Figure 2.1. Let us assume that the system has cylindrical symmetry and the material has no azimuthal velocity component. The locus of the thin shell can therefore be described as $R(\theta)$, where R is the spherical radius of the layer and θ is the polar angle. Let $\dot{m}_1$ and v_1 be the mass loss rate and the velocity of the wind from the star 1, located at the origin of the spherical coordinate system (R, θ, ϕ), and $\dot{m}_2$ and v_2 the corresponding quantities of the wind from the star 2 located at a distance D (see Figure 2.1). The rates of mass, r and z momentum, and angular momentum around the origin, incorporating into the shell from the star 1 are given by

$$\dot{M}_1 = \frac{\dot{m}_1}{2}(1 - \cos\theta), \tag{2.2}$$

$$\dot{\Pi}_{z1} = \frac{\dot{m}_1\, v_1}{4}\sin^2\theta,$$

$$\dot{\Pi}_{r1} = \frac{\dot{m}_1\, v_1}{4}(\theta - \sin\theta\cos\theta),$$

$$\dot{J}_1 = 0,$$

respectively. Analogously, the rates from star 2 are given by

$$\dot{M}_2 = \frac{\dot{m}_2}{2}(1 - \cos\theta_1), \tag{2.3}$$

$$\dot{\Pi}_{z2} = -\frac{\dot{m}_2\, v_2}{4}\sin^2\theta_1,$$

$$\dot{\Pi}_{r2} = \frac{\dot{m}_2\, v_2}{4}(\theta_1 - \sin\theta_1\cos\theta_1),$$

$$\dot{J}_2 = \frac{\dot{m}_2\, v_2}{4}(\theta_1 - \sin\theta_1\cos\theta_1)D.$$

Assuming that the flow in the thin shell is well mixed, it has the single flow velocity

$$\bar{v} = v_r\,\hat{r} + v_z\,\hat{z}, \tag{2.4}$$

where $\hat{r}$ and $\hat{z}$ are the unit vectors measured along the directions of the cylindrical radius and symmetry axis, respectively. The steady state assumption requires that the rates of mass, and linear and angular momentum through the control line, must be equal to those injected by the two winds between the direction of the symmetry axis and the angle θ. Thus, these quantities denoted by $\dot{M}(\theta)$, $\dot{\Pi}_r(\theta)$, $\dot{\Pi}_z(\theta)$, and $\dot{J}(\theta)$, are given by

$$\dot{M}(\theta) = \dot{M}_1 + \dot{M}_2, \tag{2.5}$$

$$\dot{\Pi}_r(\theta) = \dot{\Pi}_{r1} + \dot{\Pi}_{r2} = \dot{M}(\theta)\, v_r,$$

$$\dot{\Pi}_z(\theta) = \dot{\Pi}_{z1} + \dot{\Pi}_{z2} = \dot{M}(\theta)\, v_z$$

$$\dot{J} = \dot{J}_1 + \dot{J}_2 = \dot{M}(\theta)\, v_\theta\, R(\theta),$$

being $v_\theta = v_r\,\cos\theta - v_z\,\sin\theta$.

Substituting equations (2.2) and (2.3) into equations (2.5), and combining the resulting equations we obtain,

$$R = D\sin\theta\,\csc(\theta + \theta_1), \tag{2.6}$$

and

$$\theta_1\cot\theta_1 = 1 + \beta(\theta\cot\theta - 1), \tag{2.7}$$

where $\beta = (\dot{m}_1 v_1)/(\dot{m}_2 v_2)$ is the wind momentum ratio. In this way, the shape of the thin shell is highly dependent on the parameter β. In Figure 2.2, we present the locus of the thin shell, for several values of β.

The stagnation point radius R_0 follows directly from the pressure balance condition and is

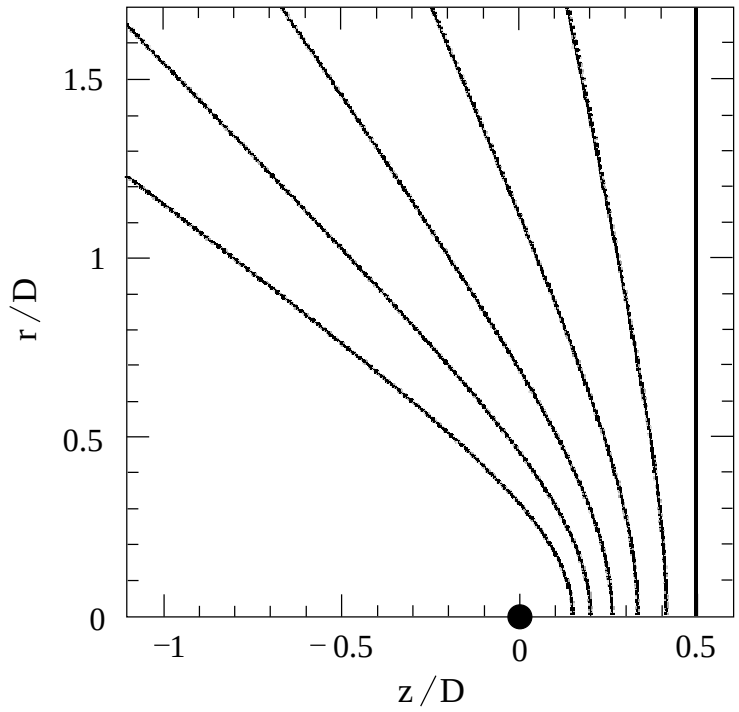

Figure 2.2 Graph showing the curve obtained from the solution $R(\theta)$. The locus of the thin shell is shown for different values of wind momentum ratio β: $\beta = 1$ (vertical line), 0.5, 0.25, 0.125, 0.0625, 0.03125 (inner and more highly curved line). The position of the source located at the origin is indicated with the filled circle, and the second wind source is located at $z/D = 1$, outside the plot toward the right (Cantó et al. 1996).

given by,

$$R_0 = \frac{\beta^{1/2}\, D}{1 + \beta^{1/2}} \tag{2.8}$$

Furthermore, the asymptotic angle θ_∞ of the bow shock wing (corresponding to $R \to \infty$) can be found from the equation (2.6) using the condition $\theta_\infty + \theta_{1\infty} = \pi$, which yields

$$\theta_\infty - \tan\theta_\infty = \frac{\pi}{1-\beta}. \tag{2.9}$$

2.2.2 The Emission Measure of the Thin Shell

The flow within the thin shell is confined by the front shocks of the two stellar winds. Let h be the position-dependent thickness of the thin shell, and l the longitude-coordinate measured inwards from the wind shock of the star 2, and perpendicular to the thin shell. Then, the shock fronts from the sources 1 and 2 are located at $l = 0$ and $l = h$, respectively (see Figure 2.3). Assuming isothermal shocks, the pressure within the shell just behind each shock front can be written as,

$$P_1 = P(l = h) = \rho_1\, v_{n,1}^2, \tag{2.10}$$

$$P_2 = P(l = 0) = \rho_2\, v_{n,2}^2, \tag{2.11}$$

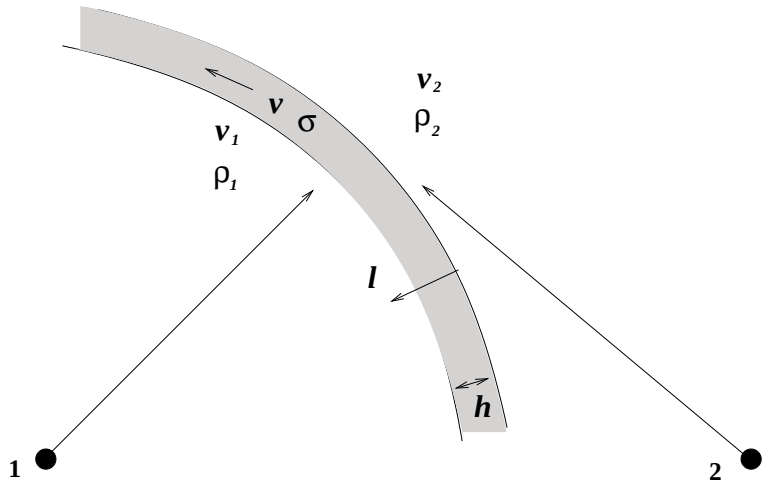

Figure 2.3 Schematic diagram showing a thin shell, limited by two shock fronts, resulting from the interaction of two stellar winds. The shocked gas flows along the shell at a velocity v and has a surface density σ. The coordinate l is measured inwards from the wind shock of source 2, normal to the locus of the thin shell.

where ρ_1 and ρ_2 are the pre-shock densities, and $v_{n,1}^2$ and $v_{n,2}^2$ are the velocity components normal to the shell of the winds 1 and 2, respectively.

Assuming that the flow within the shell is photoionized by an external source, it can be approximated as an isothermal flow. Then, the pressure as a function of the parameter l can be obtained by the hydrostatic equation,

$$\frac{dP}{dl} = -\rho\, g\,, \tag{2.12}$$

where $P = \rho\, c_s^2$ (being c_s the isothermal sound speed), and the centrifugal acceleration $g = v^2/R_c$, with R_c the radius of curvature of the thin shell. Integrating equation (2.12) with the boundary condition given by equation (2.11), we obtain

$$P(l) = \rho(l)\, c_s^2 = P_2\, \mathrm{e}^{-l/H}, \tag{2.13}$$

where $H = c_s^2/g$ is the scale height parameter of pressure (or density). On the other hand, from equations (2.10) and (2.13) we found the relation between P_1 and P_2 for the thin shell

$$P_1 = P_2\, e^{-h/H}. \tag{2.14}$$

Using equations (2.13) and (2.14), we can now calculate the surface density,

$$\sigma = \int_0^h \rho(l)\, dl = \frac{H}{c_s^2}\,(P_2 - P_1), \tag{2.15}$$

and the emission measure of the thin shell

$$EM = \int_0^h (\rho/\bar{m})^2\, dl = \frac{\sigma}{2\bar{m}^2 c_s^2}\,(P_2 + P_1)\,, \tag{2.16}$$

where $\bar{m} = \mu m_p$ is the average mass per particle of the photoionized gas with μ the mean atomic weight per electron, and m_p the mass of the proton.

2.2.3 The Flow Velocity and the Surface Density of the Shell

Equation (2.16) gives the emission measure of the thin shell in terms of its surface density. Next, we must obtain the surface density as a function of position on the shell. We first note that the shocked gas can be described as a flow of streamlines with constant azimuthal angle ϕ. The mixing of the two shocked winds is assumed to be instantaneous so that the flow has a unique flow velocity v (see equation 2.4) at any location within the shell. The mass rate $\dot{M}$ flowing along a ring of radius $r(= R\,\sin\theta)$ of the layer is then given by

$$\dot{M} = 2\pi\, R \sin\theta\, \sigma v\,. \tag{2.17}$$

On the other hand, the normal vector to the surface of the shell $\hat{n}$ can be obtained from the gradient of the function $F = r' - R(\theta)$, where r' is the radial coordinate, and the bow shock is described by $F = 0$. Thus, $\hat{n} = \nabla F / \mid \nabla F \mid$, where ∇ denotes the vector differential operator gradient in spherical coordinates (see Wilkin 1997). For cylindrical symmetry $\partial R/\partial\phi = 0$, and then

$$\hat{n} = \frac{\hat{R} - 1/R\,(\partial R/\partial\theta)\,\hat{\theta}}{\sqrt{(1 + 1/R^2\,(\partial R/\partial\theta)^2)}}\,, \tag{2.18}$$

where $\hat{R}$ and $\hat{\theta}$ are unit vectors measured along the directions R and θ, respectively. The velocity vectors of the winds 1 and 2 are given by

$$\bar{v_1} = v_1 \hat{R}, \tag{2.19}$$

$$\bar{v_2} = -v_2 \cos(\theta + \theta_1)\hat{R} + v_2 \sin(\theta + \theta_1)\hat{\theta}, \tag{2.20}$$

respectively. From equations (2.18), (2.19), and (2.20), we calculate the normal components of the pre-shock velocities at every point (R,θ) of the stellar winds,

$$v_{1,n} = v_1\, \frac{R}{\sqrt{R^2 + (\partial R/\partial\theta)^2}}\,, \tag{2.21}$$

$$v_{2,n} = -v_2\, \frac{R\cos(\theta + \theta_1) + (\partial R/\partial\theta)\sin(\theta + \theta_1)}{\sqrt{R^2 + (\partial R/\partial\theta)^2}}\,. \tag{2.22}$$

Therefore, from equations (2.10) and (2.11), the pressure within the thin shell just behind each shock front can be written as

$$P_1 = \rho_{1,0}\, v_{1,0}^2\, f_{w,1}\,(\theta, \theta_1)\,, \tag{2.23}$$

and

$$P_2 = \rho_{1,0}\, v_{1,0}^2\, f_{w,2}\,(\theta, \theta_1)\,, \tag{2.24}$$

where we use the density and velocity of the wind from the star 1 , $\rho_{1,0}$ and $v_{1,0}$, at the stagnation point R_0, to nondimensionalize the equations, and,

$$f_{w,1}\,(\theta, \theta_1) = \left(\frac{\rho_1\, v_1^2}{\rho_{1,0}\, v_{1,0}^2}\right) \frac{R^2}{R^2 + (\partial R/\partial\theta)^2}, \tag{2.25}$$

and

$$f_{w,2}\,(\theta, \theta_1) = \left(\frac{\rho_2\, v_2^2}{\rho_{1,0}\, v_{1,0}^2}\right) \frac{\left[R\cos\left(\theta + \theta_1\right) + (\partial R/\partial\theta)\sin\left(\theta + \theta_1\right)\right]^2}{R^2 + (\partial R/\partial\theta)^2}\,. \tag{2.26}$$

We now write equations (2.5) in the form

$$\dot{M} = \frac{\dot{m}_1}{2}\, f_m(\theta, \theta_1), \tag{2.27}$$

$$\dot{\Pi}_r = \frac{\dot{m}_1\, v_1}{2}\, f_r(\theta, \theta_1) = \dot{M}\, v_r,$$

$$\dot{\Pi}_z = \frac{\dot{m}_1\, v_1}{2}\, f_z(\theta, \theta_1) = \dot{M}\, v_z,$$

where,

$$f_m(\theta, \theta_1) = 1 - \cos\theta + \frac{v_1}{\beta\, v_2}(1 - \cos\theta_1), \tag{2.28}$$

$$f_r(\theta, \theta_1) = \frac{1}{2}\left[\theta - \sin\theta\cos\theta + \frac{1}{\beta}\left(\theta_1 - \sin\theta_1\cos\theta_1\right)\right],$$

$$f_z(\theta, \theta_1) = \frac{1}{2}\left[\sin^2\theta\, - \frac{1}{\beta}\sin^2\theta_1\,\right].$$

From equations (2.27) and (2.28) and equation (2.4), the tangential velocity along the thin shell is then given by,

$$v = v_1 \frac{\sqrt{f_r^2\,(\theta, \theta_1) + f_z^2\,(\theta, \theta_1)}}{f_m(\theta, \theta_1)}\,, \tag{2.29}$$

Substitution of equations (2.6) and (2.29) into equation (2.17) gives the surface density,

$$\sigma = \sigma_0\, f_\sigma(\theta, \theta_1)\,, \tag{2.30}$$

where $\sigma_0 = \dot{m}_1/(2\pi\beta D v_1)$ and

$$f_\sigma(\theta, \theta_1) = \frac{\beta}{2}\sin\left(\theta + \theta_1\right)\csc\theta_1\csc\theta\, \frac{f_m^2(\theta, \theta_1)}{\sqrt{f_r^2(\theta, \theta_1) + f_z^2(\theta, \theta_1)}}\,. \tag{2.31}$$

Finally, it follows from equation (2.16) that the emission measure of the thin shell is given

by,

$$EM(\theta,\theta_1) = EM_0\, f_\sigma(\theta,\theta_1)\,[f_{w,1}\,(\theta,\theta_1) + f_{w,2}\,(\theta,\theta_1)]\,, \tag{2.32}$$

with $EM_0 = \sigma_0\,\rho_{1,0}\,v_{1,0}^2/(2\bar{m}^2 c_s^2)$.

2.2.4 Predicted Thermal Radio-continuum Emission from Radiative Systems

In order to calculate the radio-continuum emission from the whole system, it is necessary to compute the total optical depth along each line of sight, which will have the contribution from both the stellar winds and the thin shell. Then, we have to estimate the intensity emerging from each direction and, finally, calculate the flux by integrating the intensity over the solid angle.

The optical depth perpendicular to the shell is given by

$$\tau_{WCR,\perp}(\theta,\theta_1) = EM(\theta,\theta_1)\,\chi(\nu) \tag{2.33}$$

where EM is given by the equation (2.32) and $\chi(\nu) = 8.436\times10^{-7}\,\nu^{-2.1}$ with the frequency ν in Hz, assuming an electron temperature $T_e = 10^4\,\mathrm{K}$. By defining a critical frequency ν_c, such that

$$\left(\frac{\nu}{\nu_c}\right)^{-2.1} = \left(\frac{\dot{m}_1}{4\pi\bar{m}v_{1,0}^2}\right)^2 \frac{\chi(\nu)}{R_0^3}\,, \tag{2.34}$$

it can be shown from equation (2.32) that

$$\tau_{WCR,\perp}(\theta,\theta_1) = \left(\frac{\nu}{\nu_c}\right)^{-2.1}\left(\frac{v_{1,0}}{c_s}\right)^2\left(\frac{1}{\beta\tilde{D}}\right) f_\sigma(\theta,\theta_1)\,[f_{w,1}\,(\theta,\theta_1) + f_{w,2}\,(\theta,\theta_1)]\,, \tag{2.35}$$

where $\tilde{D} = D/R_0$. Hereinafter tilde variables are defined in units of R_0.

The optical depth of the shell intersected by a given line of sight is $\tau_{WCR} = \tau_{WCR,\perp}\,\cos^{-1}\varphi$, where φ is the angle between the vector normal to the surface of the shell $\hat{n}$ (equation [2.18]), and the unit vector $\hat{z}$ ($= \cos\theta\,\hat{R} - \sin\theta\,\hat{\theta}$; see Figure 2.4). Then, we obtain

$$\tau_{WCR}(\theta,\theta_1) = \tau_{WCR,\perp}(\theta,\theta_1)\frac{\sqrt{\tilde{R}^2 + (\partial\tilde{R}/\partial\theta)^2}}{\tilde{R}\cos\theta + \sin\theta\,(\partial\tilde{R}/\partial\theta)}\,. \tag{2.36}$$

Let us now calculate the contribution of the unshocked stellar winds to the total optical depth. Consider a line of sight that intersects the thin shell at a point $(\tilde{z},\tilde{r})$, with $\tilde{z} = \tilde{r}\,\cot\varphi$ (see Figure 2.4). According to Panagia & Felli (1975) and Wright & Barlow (1975), the optical depth along the line of sight of the wind source 1 is obtained by (see also Section 1.2.1)

$$\tau_{w,1}(\theta) = \int_{-\infty}^{\tilde{r}\,\cot\theta} n_{w,1}^2(\tilde{z})\,\chi(\nu)\,d\tilde{z}\,, \tag{2.37}$$

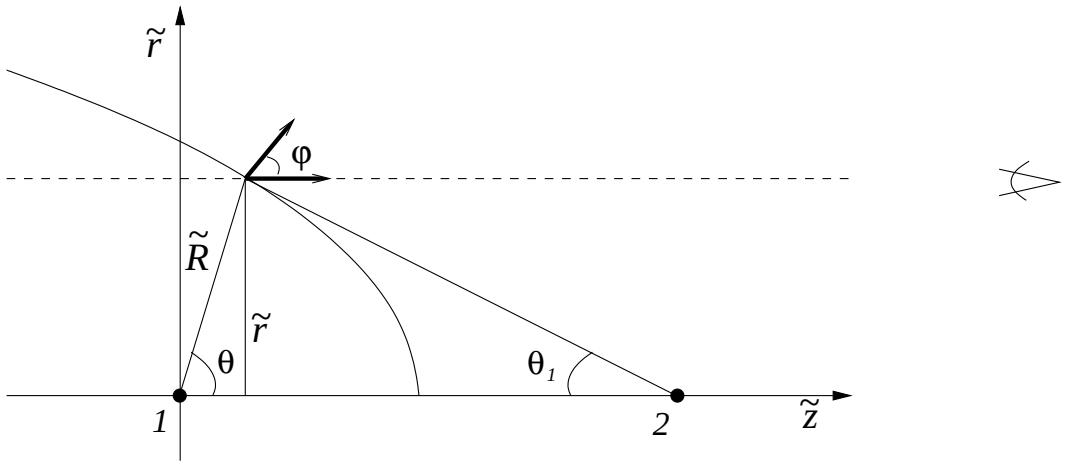

Figure 2.4 Schematic diagram illustrating the thin shell from the interaction of two wind sources. The normal vector to the surface of the shell $\hat{n}$, the unit vector $\hat{z}$, and the angle φ between them are shown. The point at which the line of sight intersects the shell is given by the coordinates $(\tilde{z}, \tilde{r})$.

where

$$n_{w,1}(\tilde{z}) = n_{1,0}\,\frac{1}{\tilde{z}^2+\tilde{r}^2}\,, \tag{2.38}$$

where $n_{1,0} = \rho_{1,0}/\bar{m}$ $(= \dot{m}_1/4\pi\bar{m}v_{1,0}R_0^2$) is the number density of the flow at the stagnation point. Solving the equation (2.37) and using (2.34) and (2.38), it follows that

$$\tau_{w,1}(\theta) = \left(\frac{\nu}{\nu_c}\right)^{-2.1} I_{w,1}(\theta)\,, \tag{2.39}$$

with

$$I_{w,1}(\theta) = \frac{1}{2\tilde{r}^3}\left[\frac{\pi}{2} + \frac{\cot\theta}{\cot^2\theta+1} + \theta\right].$$

Analogously, the optical depth of the wind source 2, located at $\tilde{z} = \tilde{D}$, is obtained by

$$\tau_{w,2}(\theta) = \int_{\tilde{r}\cot\theta}^{\infty} n_{w,2}^2(\tilde{z})\,\chi(\nu)\,d\tilde{z}\,, \tag{2.40}$$

where

$$n_{w,2}(\tilde{z}) = n_{2,0}\,\frac{1}{[\tilde{z}-\tilde{D}]^2+\tilde{r}^2}\,, \tag{2.41}$$

where $n_{2,0} = \rho_{2,0}/\bar{m}$ $(= \dot{m}_2/4\pi\bar{m}v_{2,0}R_0^2)$ is the number density of the wind at the stagnation point. Substitution of equations (2.34) and (2.41) into equation (2.40) gives,

$$\tau_{w,2}(\theta) = \left(\frac{\nu}{\nu_c}\right)^{-2.1} I_{w,2}(\theta)\,, \tag{2.42}$$

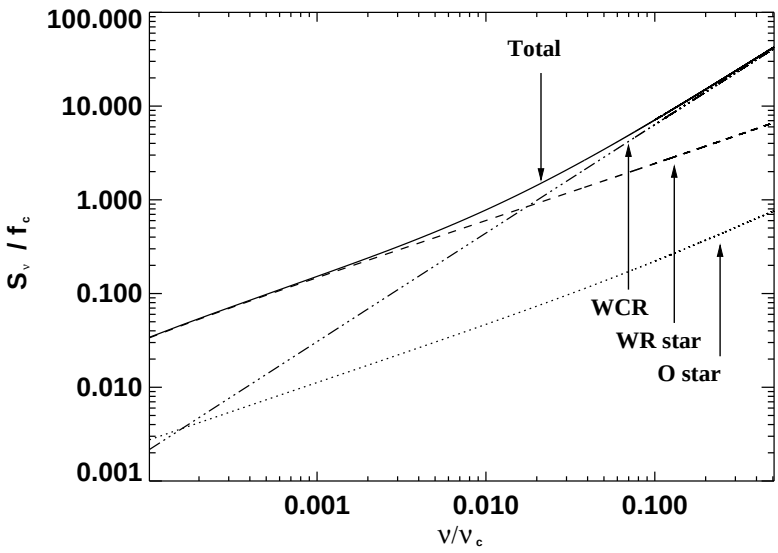

Figure 2.5 Predicted free-free emission from a colliding wind binary. We adopted the parameters $v_1 = 10^3$ km s^{-1}, $\dot{m}_1 = 1.25 \times 10^{-5}$ M$_\odot$ yr^{-1}, and $v_2 = 10^3$ km s^{-1}, $\dot{m}_2 = 5 \times 10^{-5}$ M$_\odot$ yr^{-1} for the wind sources. The binary separation is set to $D = 4$ AU. The dotted and dashed lines represent the fluxes ($\propto \nu^{0.6}$) from the wind sources 1 and 2 (see also Figure 1), respectively. The intrinsic thermal emission from the WCR (dot-dashed line) and the total emission (solid line) from the binary system are also shown. The behavior of the curves is described in the main text.

with

$$I_{w,2}(\theta) = \left(\frac{\dot{m}_2\, v_1}{\dot{m}_1\, v_2}\right)^2 \frac{1}{2\tilde{r}^3} \left[\frac{\pi}{2} - \frac{(\tilde{r}\cot\theta - \tilde{D})\,\tilde{r}}{\tilde{r}^2 + (\tilde{r}\cot\theta - \tilde{D})^2} - \mathrm{arcot}\left(\frac{\tilde{r}\cot\theta - \tilde{D}}{\tilde{r}}\right)\right]. \tag{2.43}$$

Assuming that the distance L from the observer to the system is large enough ($D \ll L$), the lines of sight intersecting the central stars can be ignored. Then, the radio-continuum flux density from the colliding wind binary can be calculated by

$$S_\nu = 2\pi B_\nu \left(\frac{R_0}{L}\right)^2 \int_0^{\tilde{r}(\theta_\infty)} [1 - \mathrm{e}^{-\tau(\theta,\theta_1)}]\,\tilde{r}\,d\tilde{r}, \tag{2.44}$$

where $\tau(\theta,\theta_1) = \tau_{WCR}(\theta,\theta_1) + \tau_{w,1}(\theta) + \tau_{w,2}(\theta)$ is the total optical depth along the line of sight, B_ν ($= 2kT\nu^2/c^2$; with k the Boltzmann's constant, c the light speed) is the Planck function in the Rayleigh-Jeans approximation, and $\tilde{r}(\theta_\infty)$ is the impact parameter at the asymptotic angle θ_∞ given by equation (2.9).

Defining the parameter $f_c = 4\pi kT(R_0/cL)^2\nu_c^2$, we finally obtain

$$S_\nu = f_c \left(\frac{\nu}{\nu_c}\right)^2 \left[\int_0^{\theta_\infty} (1 - \mathrm{e}^{-\tau(\theta,\theta_1)})\,(\tilde{R}^2(\theta)\sin\theta\cos\theta\,d\theta + \tilde{R}(\theta)\sin^2\theta\,(\partial\tilde{R}/\partial\theta)\,d\theta)\right]. \tag{2.45}$$

This equation represents a self-similar solution for the thermal free-free emission from colliding wind binaries with a radiative WCR.

We compute the emission from a colliding wind binary with stellar wind parameters $v_1 = 10^3\,\mathrm{km\,s^{-1}}$ and $\dot{m}_1 = 1.25\times10^{-5}\,\mathrm{M_\odot\,yr^{-1}}$, and $v_2 = 10^3\,\mathrm{km\,s^{-1}}$ and $\dot{m}_2 = 5\times10^{-5}\,\mathrm{M_\odot\,yr^{-1}}$. We assume $D = 4$ AU as the binary separation between the stars. These stellar wind parameters are similar to those of a typical WR+O system and, together with the binary separation, are in agreement with the assumption of a radiative WCR ($\chi \sim 0.06$, see equation [2.1]).

In Figure 2.5, we plot the contributions to the total radio emission of the two unshocked stellar winds and the WCR. As expected from the standard wind assumptions, the flux densities from the stellar winds show spectral indices ~ 0.6. However, for the wind source 1, the spectral index presents at high frequencies a slight deviation from the expected value of 0.6. This is likely to result from the presence of the WCR inside the optically thick region of the wind. The intrinsic flux density from the WCR shows a spectral index, $\alpha_{wcr} \sim 1.1$, which is consistent with the results predicted from numerical models (in massive O+O type binary stars) developed by Pittard (2010) for radiative systems. Note that as ν increases the emission from the WCR becomes more important. At low frequencies, the total flux density grows as $S_\nu \propto \nu^{0.6}$, approaching the emission from the strongest wind. On the other hand, at higher frequencies, the radio spectrum from the system approaches the flux density from the WCR as $S_\nu \propto \nu^{1.1}$.

2.3 The Particular Case of Two Identical Winds

In this section, we consider two stars with identical winds, which are assumed to be spherically symmetric, steady, and completely ionized. Let $v_1 = v_2$ and $\dot{m}_1 = \dot{m}_2$ be the velocity and mass loss rate of the winds. In this particular case, the wind momentum ratio of the interacting winds $\beta = 1$, the stagnation point radius $R_0 = D/2$, and the angle $\theta = \theta_1$ (see equations [2.6] and [2.7], and Figure 2.1).

First, we estimate the emission measure of the shocked layer as follows. From equations (2.28)

$$f_m(\theta) = 2\,(1 - \cos\theta)\,, \tag{2.46}$$

$$f_r(\theta) = \theta - \sin\theta\cos\theta\,, \tag{2.47}$$

and,

$$f_z(\theta) = 0\,. \tag{2.48}$$

Substitution of equations (2.46), (2.47), and (2.48) into equation (2.29) gives the velocity along the shell,

$$v = \frac{v_1}{2}\left(\frac{\theta - \sin\theta\cos\theta}{1 - \cos\theta}\right), \tag{2.49}$$

and the mass injection rate (into a solid angle defined by θ) of the stellar winds is given by,

$$\dot{M} = \dot{m}_1 \, (1 - \cos\theta) \, . \tag{2.50}$$

Combining equations (2.17), (2.49), and (2.50), we obtain for the surface density of the shell

$$\sigma = \frac{\dot{m}_1 \, (1 - \cos\theta)^2}{\pi \, v_1 \, R \sin\theta \, (\theta - \sin\theta \cos\theta)} \, , \tag{2.51}$$

In this simple case $R = R_0 / \cos\theta$, and the normal component of the preshock velocity of the stellar wind $v_{1,n} = v_1 \cos\theta$. Therefore, the pressure $P_1 = \rho_1 \, v_{1,n}^2$ within the thin shell just behind the shock front can be written as

$$P_1 = \frac{\dot{m}_1 \, v_1}{4\pi \, R_0^2} \cos^4\theta \, . \tag{2.52}$$

Note that, in this particular case, $P_1 = P_2$.

On the other hand, from equation (2.16), it follows that the emission measure of the shell is $EM_s = \sigma \, P_1 / \bar{m}^2 \, c_s^2$. Using equations (2.51) and (2.52), it can be shown that,

$$EM_s = \frac{\dot{m}_1^2}{4\pi^2 \bar{m}^2 c_s^2 R_0^3} \left[\frac{\cos^5\theta \, (1 - \cos\theta)^2}{\sin\theta \, (\theta - \sin\theta \cos\theta)} \right] . \tag{2.53}$$

Let us now calculate the emission measure of the stellar winds. Since the winds have the same parameters, the emission measure is

$$EM_w = 2 \int_{-\infty}^{R_0} n_w^2 dz \, = 2 \left(\frac{\dot{m}_1}{4\pi \, \bar{m} v_1} \right)^2 \int_{-\infty}^{R_0} \frac{dz}{(r^2 + z^2)^2}, \tag{2.54}$$

and integrating one obtains,

$$EM_w = \frac{\dot{m}_1^2}{16\pi^2 \, \bar{m}^2 v_1^2 r^3} \left[\frac{\pi}{2} + \frac{(r/R_0)}{1 + (r/R_0)^2} + \operatorname{arcot}\left(\frac{R_0}{r} \right) \right] . \tag{2.55}$$

Thus, the total emission measure is given by $EM = EM_s + EM_w$.

2.3.1 The Emission Measure EM as a Function of the Stagnation Point R_0

Here we keep the impact parameter r constant, in order to investigate the behavior of the emission measure EM as function of the stagnation point radius R_0. The total emission measure along a given line of sight can be written as

$$EM = \frac{\dot{m}_1^2}{4\pi^2 \, \bar{m}^2 c_s^2 r^3}, \left(f_s + f_w \right) , \tag{2.56}$$

where

$$f_s = \left(\frac{r}{R_0} \right)^3 \left[\frac{\cos^5\theta \, (1 - \cos\theta)^2}{\sin\theta \, (\theta - \sin\theta \cos\theta)} \right], \tag{2.57}$$

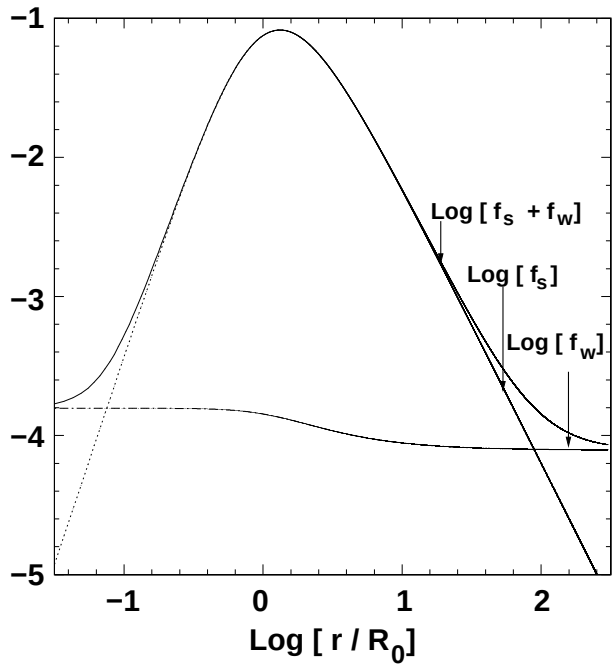

Figure 2.6 Nondimension emission measure as a function of r/R_0. The impact parameter r is kept constant. The dotted and dashed lines represent the functions, f_s of the shell, and f_w of the stellar winds, respectively. The total nondimensional emission measure $f_s + f_w$ is represented by the solid line. The physical description of the plot is given in the text.

and

$$f_w = \frac{1}{4}\left(\frac{c_s}{v_1}\right)^2 \left[\frac{\pi}{2} + \frac{r/R_0}{1+(r/R_0)^2} + \operatorname{arcot}\left(\frac{R_0}{r}\right)\right]. \tag{2.58}$$

Substituting the trigonometric functions $\sin\theta = (r/R_0)/\sqrt{1+(r/R_0)^2}$, $\cos\theta = 1/\sqrt{1+(r/R_0)^2}$, and $\theta = \operatorname{arcot}(r/R_0)$ into equation (2.57), it is possible to give the emission measure in terms of r/R_0 (equation [2.56]) as a single function $EM(r/R_0)$.

In Figure 2.6, we present f_s, f_w, and $f_s + f_w$ as functions of r/R_0, which determine the behavior of EM. We keep the impact parameter r constant and only varies the stagnation point radius R_0, and consequently the binary separation D. Initially, as r/R_0 increases (which means closer binary systems), the emission measure from the shell increases, reaching a maximum value at $r/R_0 \simeq 1.3$, after which it steadily decreases.

This behavior can be understood as follows: for $r \ll R_0$, the preshock densities, and hence the pressures within the shocks and their EM, increase as the stars become closer to each other. On the other hand, for $r \gg R_0$, the preshock densities play a minor role, and it is now the normal components of the preschock velocities which determine the behavior of the pressures. In this case, as r/R_0 increases (closer systems), the preshock velocities, and hence the pressures and the EM decrease. In addition, it can be observed from the Figure that for $r/R_0 \simeq 1$, $f_s \gg f_w$, and then the emission is dominated by the shell. On other hand, for $r/R_0 \ll 1$, and $r/R_0 \gg 1$, the emission is dominated by the unshocked stellar winds.

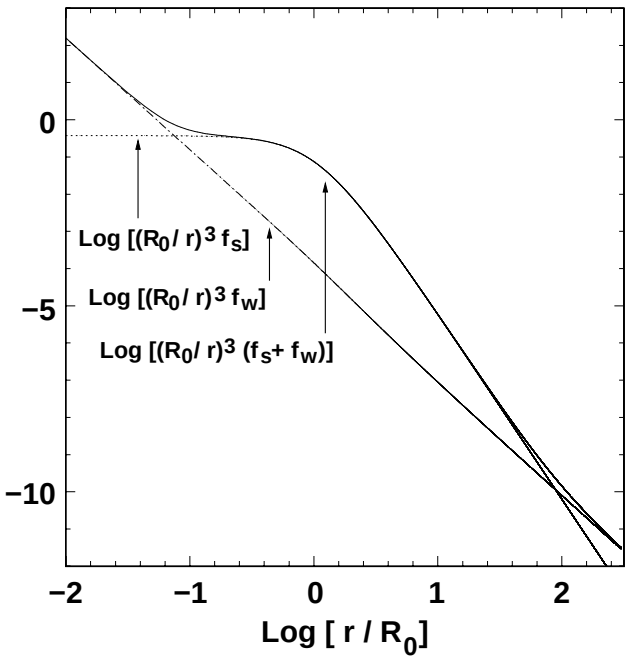

Figure 2.7 Behavior of the nondimension emission measure as function of r/R_0 by fixing the stagnation point R_0. The function $(r/R_0)^{-3} f_s$ (dotted line) of the shell, and $(r/R_0)^{-3} f_w$ (dashed line) of the stellar winds are presented. The solid line represents the total nondimension emission measure $(r/R_0)^{-3} (f_s + f_w)$. The physical description of the plot is given in the text.

2.3.2 The Emission Measure EM as a Function of the Impact Parameter r

We now fix the stagnation point radius R_0 and investigate the variation of the total emission measure EM as a function of the impact parameter r. In this case, it is useful to write the total emission measure $EM\,(= EM_s + EM_w)$ given by equation (2.56) as

$$EM = \frac{\dot{m}_1^2}{4\pi^2 \bar{m}^2\, c^2 R_0^3} \left(\frac{R_0}{r}\right)^3 \Big(f_s + f_w\Big). \tag{2.59}$$

In Figure 2.7, we show the total emission measure EM, as well as the contributions from the shell EM_s and the unshocked winds EM_w. We note from the Figure that the emission measure is dominated by the shell ($EM_s \gg EM_w$) at impact parameters $(r/R_0) \simeq 1$. However, at very low ($r/R_0 \ll 1$) or very high ($r/R_0 \gg 1$) values of the impact parameter, the contribution of the stellar winds to the total emission measure is more important ($EM_s \ll EM_w$).

Given the emission measure EM_s, the optical depth of the shell as function of r can be written as

$$\tau_s = \frac{A_\nu}{r^3}\, f_s, \tag{2.60}$$

where $A_\nu = \dot{m}^2\, \chi(\nu)/(4\pi^2 \bar{m}^2 c_s^2)$.

PARAMETERS OF THE COLLIDING WINDS

Model [(a)]	β	D/AU	χ	R_0/D
B1	1	8	0.12	0.5
B2	1	4	0.06	0.5
B3	1	1	0.02	0.5
Model [(b)]	β	D/AU	χ	R_0/D
B4	0.25	4	0.15	0.33
B5	0.025	4	0.65	0.14

(a) $v_{1,2} = 10^3$ km s^{-1}; $\dot{m}_{1,2} = 5 \times 10^{-5}$ M$_\odot$ yr^{-1}
(b) $v_{1,2} = 10^3$ km s^{-1}; $\dot{m}_2 = 5 \times 10^{-5}$ M$_\odot$ yr^{-1}; $\dot{m}_1 = 1.25 \times 10^{-5}$ M$_\odot$ yr^{-1} for model B4 and $\dot{m}_1 = 1.25 \times 10^{-6}$ M$_\odot$ yr^{-1} for model B5.

For lines of sight with $r/R_0 \ll 1$ it can be shown that $f_s \simeq 3/8\,(r/R_0)^3$, and

$$\tau_s \simeq \frac{3}{8}\,\frac{A_\nu}{R_0^3}. \tag{2.61}$$

Therefore, in this limit, the optical depth of the shell τ_s, does not depend on the value of r, as can be seen in Figure 2.7. Furthermore, $\tau_s \propto R_0^{-3}$ (and hence $\propto D^{-3}$). This is consistent with the behavior of EM at the same limit ($r/R_0 \ll 1$), discussed in the previous subsection (see Figure 2.6).

On the other hand, for higher impact parameters when $r/R_0 \gg 1$, then $f_s \simeq 2/\pi\,(R_0/r)^2$ and

$$\tau_s \simeq \frac{2}{\pi}\,A_\nu \frac{R_0^2}{r^5}. \tag{2.62}$$

Thus, in this limit $\tau_s \propto r^{-5}$, which corresponds to the drop of the curve in Figure 2.7. Furthermore, for a given line of sight, $\tau_s \propto R_0^2$ (and hence $\propto D^2$).

2.4 The Thermal Radio-continuum Emission from Colliding Wind Binaries

In Section 2.2, we presented a model to calculate the thermal radio emission from a radiative WCR, under the assumption of a thin-shell bounded by two isothermal shocks. In this section, we investigate the behavior of the WCR contribution to the total flux density by determining its dependence with the wind parameters and the binary separation.

Here, we present analytic predictions of the thermal spectra at radio frequencies from different radiative models, which satisfy the condition of radiative shocks ($\chi < 1$) described by the equation (2.1). In Table 2.4, we list the different sets of parameters used for our analysis. In models B1-B3, we assume identical wind sources (β= 1) in order to investigate the effect of the binary separation. On the other hand, in models B2, B4, and B5, we choose wind parameters from which we obtain a different wind momentum ratio β for each model, assuming the same binary separation D for all models. For models B4 and B5 we estimate the value of χ for each

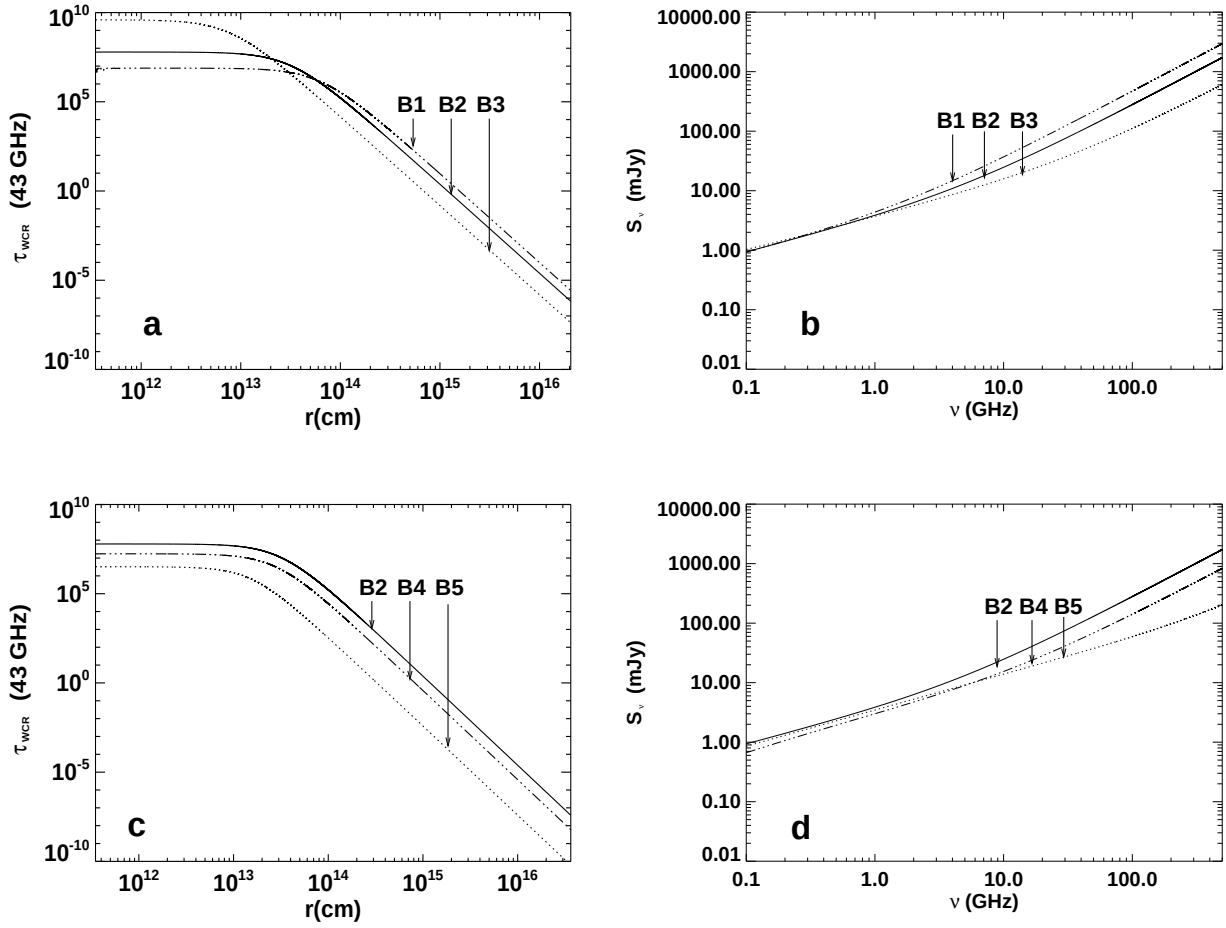

Figure 2.8 Optical depth $\tau_{WCR}(43\ \mathrm{GHz})$ of the WCR as a function of impact parameter r (left panels), and the predicted total flux density S_ν at radio frequencies (right panels) for the models of Table 2.4. In top panels, the dot-dashed, solid and dotted lines represent the optical depth and the radio spectrum from the models B1, B2, and B3, respectively. In bottom panels, the corresponding values of models B2, B4, and B5 are shown by the solid, dot-dashed, and dotted lines, respectively. The physical description of the plots are given in the text.

shock that bounds the WCR. In Table 2.4, we indicate the highest value of χ for each of these models. In Figure 2.8 we present the optical depth of the WCR as a function of the impact parameter r (left panels), and the predicted flux density at radio frequencies (right panels). Top panels show the results of the Models B1-B3, while the models B2, B4, and B5 are shown in bottom panels. Because of the geometry of the model, the emission calculated corresponds to an observer located in the orbital plane along the symmetry axis. This configuration corresponds to a system with an inclination angle $i = 90^\circ$ with the most powerful stellar wind in front, as is shown in Figure 2.1.

2.4.1 The Effect of the Binary Separation D

The models B1-B3 correspond to the particular case studied in Section 2.3. As it is seen in Figure 2.8-a, for small impact parameters ($r/R_0 \leq 1$), $\tau_{WCR}(43\ \mathrm{GHz})$ does not depend on r,

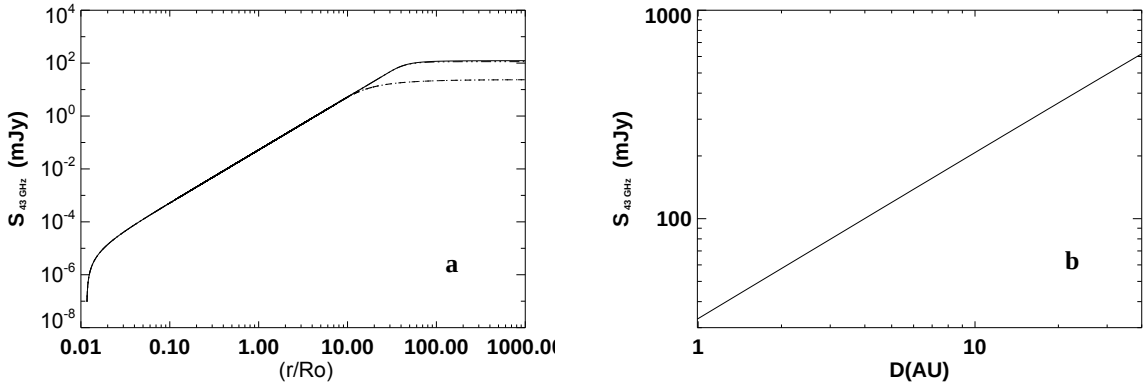

Figure 2.9 a) Integrated flux density at 43 GHz of the shocked layer over the nondimensional impact parameter r/R_0. In this example, we assumed the parameters of the colliding winds of Model B2 (see Table 2.4). The behavior of the plot is described in the text. b) Predicted flux density at $S_{43\,\mathrm{GHz}}$ from a binary system as function of the binary separation D. Also we adopted the stellar wind parameters of Model B2. We found that the flux scales as $D^{0.79}$.

and scales as D^{-3}, as predicted from the equation (2.61). On the other hand, for large impact parameters ($r/R_0 \gg 1$), τ_{WCR}(43 GHz) decreases as r^{-5} (see equation [2.62]). In addition, for a given line of sight, at this limit, τ_{WCR} scales as D^2. The dependence of τ_{WCR} with r changes at impact parameters $r \sim R_0$. This behavior of the optical depth is inherited from the emission measure EM, given by equation (2.56) (see Figures 2.6 and 2.7). On the other hand, from the predicted flux density of the models B1-B3 (Figure 2.8-b), we note that as the binary separation increases, the contribution from the shell becomes more important.

In Figure 2.9-a, we present the flux density at 43 GHz, $S_{43\,\mathrm{GHz}}$, as a function of the nondimensional impact parameter r/R_0 . We adopted the parameters of model B2. At the low impact parameters, $S_{43\,\mathrm{GHz}}$ grows as r^2, which corresponds to the emission arising from an optically thick disk whose area is $\propto r^2$. Eventually, at $r/R_0 \approx 40$, the shell becomes optically thin, and the flux density tends to a constant value. Thus, the main contribution to the flux density arises from the optically thick region of the shell and, therefore, the emission from the optically thin region can be neglected.

Let r_m be the impact parameter at which $\tau_s(r_m) = 1$. Since for lines of sight with impact parameters $r \leq r_m$ the optical depth is dominated by the shell (for simplicity, we are not considering those impact parameters $r \ll R_0$ for which $EM_s \ll EM_w$), it follows from equation (2.62) that

$$\tau(r_m) \simeq \frac{2\,A_\nu}{\pi}\frac{R_0^2}{r_m^5} \simeq 1, \tag{2.63}$$

and then the area of the optically thick region increases as $r_m \propto R_0^{2/5}$. Since the total flux density is dominated by the emission from the optically thick region it follows that $S_\nu \propto r_m^2$, and therefore, the flux density from the shell scales as $\propto D^{4/5}$ (since $R_0 \propto D$). In Figure 2.9-b we present the flux density from the shell $S_{43\,\mathrm{GHz}}$, as function of D. This emission was calculated from equation (2.45), using the stellar wind parameters of model B2. In this equation, both the optically thick and optically thin contributions of the shell are considered. From this figure

we find that $S_\nu \propto D^{0.79}$, which is consistent with the analytical prediction considering only the emission from the optically thick region of the shell. This result contrasts with the inverse dependence with the binary separation described by Pittard et al. (2006) for an adiabatic and optically thin WCR, where the flux density of the WCR is expected to scale as D^{-1}. This difference lies in the fact that for the radiative case, the emission mainly comes from an optically thick region, and hence, as we described, it depends on the surface density and the area of emitting region. On the other hand, for the adiabatic case, the material remains hot and optically thin, and hence, its total emission depends on the density (as $\rho^2 \propto D^{-4}$) and the volume of the emitting region (which is expected to scale as D^3; see Section 1.4.2).

2.4.2 The Effect of the Wind Momentum Ratio β

Finally, the effect of varying the wind momentum ratio β on the value of τ_{WCR}(43 GHz) and the total spectrum, is investigated from models B2, B4, and B5 (bottom panels of Figure 2.8). It can be seen that the optical depth increase with β for all values of r (Figure 2.8-c). Note that for a given value of β, τ_s is independent on r for $r \ll R_0$, and is $\propto r^{-5}$ for $r \gg R_0$.

Figure 2.8-d shows the predicted thermal radio spectra for these models. The plots show the dependence of the flux density with the wind momentum radio, β. At high frequencies, we note that the total flux density increases with the parameter β. This behavior is consistent with the discussion in Section 2.4.1, since as we showed, most of the emission arises from the optically thick part of the shell that increases with R_0 (Figure 2.8-c), which also increases with β (see Figure 2.2). Thus, the flux density becomes more important for higher values of β.

2.5 Restrictions and Applicability of the Model

In this section we discuss the characteristics of the binary systems for which the model described in Section 2 could be applied. First, the approximation of a radiative, isothermal shell constrains the model to those systems that satisfy the condition $\chi \ll 1$. The value of χ is highly dependent on the stellar wind parameters and the binary separation of the stars (see equation 2.1). From hydrodynamic simulations, Parkin & Pittard (2008) found that for a WR+O system, with typical mass-loss rate and velocity values (2×10^{-5} and $2 \times 10^{-6}\,\mathrm{M_\odot\,yr^{-1}}$ for the O and the WR stars, respectively, with wind velocities of $2000\,\mathrm{km\,s^{-1}}$, and masses of $50\,\mathrm{M_\odot}$ each), the cooling is efficient for orbital periods, $P \lesssim 1$ year. Furthermore, they pointed out that if the WR star is a WC subtype, cooling could be important even for periods up to several years, since cooling is more efficient with such abundances (see e.g. Stevens et al. 1992). On the other hand, Parkin & Pittard (2008) also found that O+O systems will usually be radiative for orbital periods $P \lesssim 10$ days.

On the other hand, the assumption of a steady wind will be broken for those close systems where the WCR lies into the wind acceleration region. Such situations would result in a different shape for the shell than that given by equation (2.6). Besides, Stevens & Pollock (1994) showed that, in close binaries, the radiation of a luminous star would inhibit the initial acceleration of the companion's wind towards the stagnation point. These radiative forces result in lower velocities than those expected in single star models, moderating the wind collision. Gayley et

al. (1997) investigated the potential role of the radiative braking effect, which occurs when the primary wind is decelerated by radiation pressure as it approaches the surface of the companion star. These authors concluded that radiative braking must have a significant effect for wind-wind collision in WR+O binaries with medium separations $D < 100\,R_{\odot}$ (orbital periods $\sim$15 days). For O+O type binaries, the radiative inhibition and braking effects are expected to be more relevant, specially for those systems with $P \lesssim 10$ days, for which a radiative WCR is expected. Therefore, in order to determine the applicability of our model to O+O and WR+O close binaries ($P \lesssim 15$ days), it is necessary to investigate the importance of these effects in the resulting radio spectrum of such systems.

Furthermore, flux density variability is expected to result from the change of the relative position of the stars due to the orbital motion. In this way, the flux density and spectral index are expected to be modulated along the orbit (Pittard 2010, see also Figure 1.20). Pittard (2010) investigated the contribution of the WCR to the total thermal spectrum, as a function of the orbital motion for a radiative O+O type system. They found that the minimum of the emission corresponds to an orbital configuration similar to that assumed in our model (with an inclination angle $i = 90^{\circ}$ and orbital phase ~ 0.0). Another effect of the orbital motion occurs for close systems where the orbital velocity is similar to the velocity of the wind. In this case, the wind material will be wound-up by the orbital motion into a complex geometry that our model is not considering (Stevens 1995). Recently, Parkin and Pittard (2008) carried out 3D hydrodynamical simulations of CWBs and showed that the orbital motion of the stars results in Coriolis forces that deform the shape of the WCR into a spiral structure. These factors restrict the applicability of our model to close systems in general; however, it represents a simple and useful method to determine whether a minimum for a WCR is expected to be detected from observations of radiative systems.

2.6 Comparison with Observations

Summarizing the previous discussion, our model can be applied at least to WR+O binary systems that satisfy i) $P \lesssim 1$ year, for which the cooling is important, and ii) $P \gtrsim 15$ days, where the wind acceleration region and braking effect (Gayley et al. 1997), can be neglected. The observational evidence supporting the thermal contribution from a radiative WCR is mainly expected from the presence of a steep ($\alpha > 0.6$) and variable spectrum. Several observational works have found spectral indices with high values that are difficult to explain as a single stellar wind spectrum (e.g. Leitherer 1991, Montes et al. 2009). In this section, we apply the analytical model to the close binary WR 98 and compare our results with the observations reported for this source.

The case of WR 98

WR 98 was identified as a double line binary (WN7o/WC+O8-9) with an orbital period, $P =$ 47.8 days (Gamen & Niemela 2002). Abbott et al. (1986) classified WR 98 as a non-thermal radio source. Recently, multi-wavelength observations (from 5 to 23 GHz) of this source have revealed that the spectral index changed from ~ 0.26 to ~ 0.64 in a period of time of $\sim$ 15 days

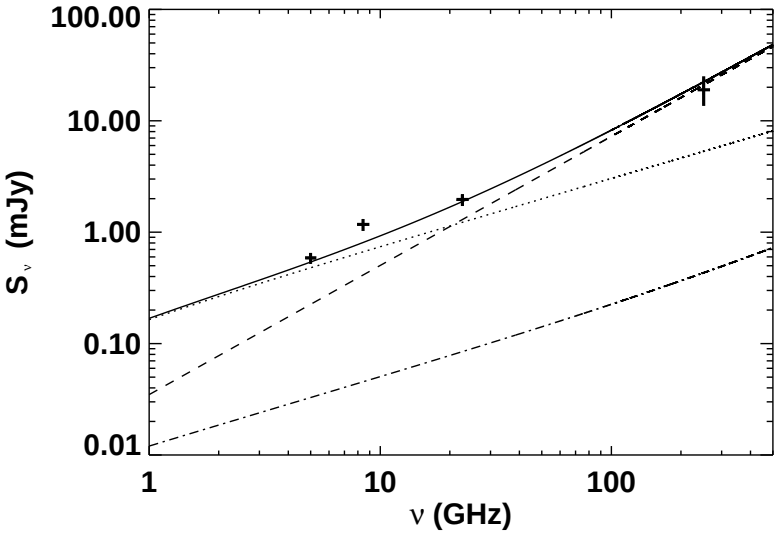

Figure 2.10 Comparison between our model and the flux densities at 5, 8.4, 23 and 250 GHz ('+' sign; uncertainty in the flux measurements are given by the length of the bars) of the binary system WR 98 obtained by Montes et al. (2009) and Altenhoff et al. (1991), respectively. We assumed the stellar wind parameters $\dot{M}_{WR} = 3.0 \times 10^{-5}\,\mathrm{M}_{\odot}\,\mathrm{yr}^{-1}$, $v_{WR} = 1200\,\mathrm{km\,s}^{-1}$, $\dot{M}_O = 4.0 \times 10^{-6}\,\mathrm{M}_{\odot}\,\mathrm{yr}^{-1}$, and $v_O = 1800\,\mathrm{km\,s}^{-1}$. The stars are separated by a distance $D \sim 0.5$ AU. The dotted and dashed lines represent the fluxes ($\propto \nu^{0.6}$) from the winds of the WR and O type stars, respectively. The radiation from the WCR (dot-dashed line) and the total flux density (solid line) from the binary source are also shown.

(see Chapter 3). This behavior suggest a binary influence over the radio spectrum, possibly from a variable non-thermal contribution that is absorbed at certain orbital phases, turning the spectrum into a "thermal state". The stellar parameters of this binary indicate that a radiative WCR ($\chi \sim 0.6$) is likely to be formed within this system.

We applied our model to the binary system WR 98 to investigate if a thermal component of emission from the WCR is able to contribute significantly to the total spectrum. Our results from the model are compared with the observations at the thermal state when $\alpha \sim 0.64$. We assumed for the WR star a mass loss rate $\dot{M}_{WR} = 3.0 \times 10^{-5}\,\mathrm{M}_{\odot}\,\mathrm{yr}^{-1}$ (upper limit derived from radio observations at the thermal phase at 8.4 GHz when $\alpha \sim 0.64$; Montes et al. 2009), and an ejection velocity $v_{WR} = 1200\,\mathrm{km\,s}^{-1}$ (Eenens & Williams, 1994). The best fit to the observations was found for an O-type star with stellar wind parameters $\dot{M}_O = 4.0 \times 10^{-6}\,\mathrm{M}_{\odot}\,\mathrm{yr}^{-1}$ and $v_O = 1800\,\mathrm{km\,s}^{-1}$. With these values we calculate the parameters: $\beta = 0.20$, $R_0 = 0.31D$, and $\theta_{\infty} = 0.6\,\pi$.

We assume a mean atomic weight per electron $\mu = 4.2$ and an average ionic charge $Z = 1.1$ for the WR wind, and $\mu = 1.5$ and $Z = 1$ for the O star (which are typical values for O-type stars; see Bieging et al. 1989). Considering that most of the emission from the WCR arises from impact parameters, r, such that $\theta < \theta_{\infty}$, from equations (2.2) and (2.3) we can estimate the ratio of mass incorporating to the WCR from the WR stellar wind, to that from the O star, $\dot{M}_2/\dot{M}_1 > 0.75$. Thus, we assume that the WCR is mainly composed by material from

the strongest wind, and we adopt the same values of μ and Z for the shocked material as those used for the WR wind. From the value of $a \sin i \sim 100\,R_{\odot}$, (where a is the semi-major axis and i is the inclination angle of the orbit) determined by Gamen & Niemela (2002), we assume $D \sim 0.5$ AU, which is the value for a (when $i \sim 90°$). Since the geometric configuration assumed for the model represents the WR stellar wind in front of the O star, we are determining the minimum expected thermal contribution from the WCR.

In Figure 2.10, we show the predicted spectrum from WR 98 system. The observational data, $S_{5\,\mathrm{GHz}} = 0.58 \pm 0.06\,\mathrm{mJy}$, $S_{8.4\,\mathrm{GHz}} = 1.18 \pm 0.05\,\mathrm{mJy}$, and $S_{23\,\mathrm{GHz}} = 1.94 \pm 0.15\,\mathrm{mJy}$, (presented in Table 3.3) are also plotted. It can be seen that our model predicts an increase in the flux density at high frequencies, which results in a steepening of the spectrum with respect to the standard 0.6 value for stellar winds. We also note that for a frequency of 250 GHz, the WCR produces an excess of emission of a factor > 2 over the $\sim$8 mJy expected for the WR wind. To test this prediction of the model at higher frequencies, we included the flux density $S_{250\,\mathrm{GHz}} = 19 \pm 5\,\mathrm{mJy}$ measured by Altenhoff et al. (1991), which seems to agree with the 22 mJy predicted for the total flux density at 250 GHz.

From our model, we have found that a thermal contribution from a radiative WCR in WR 98 is likely to be detected at high frequencies. However, as we pointed out, we can only present a lower limit for this contribution, due to the uncertainty of parameters such as the binary separation, D. On the other hand, as we previously established, the configuration adopted in our model (with an inclination angle of 90° and orbital phase ~ 0) corresponds to the minimum contribution to the total thermal emission expected from radiative shocks in binary systems with an inclination angle $\sim 90°$ (according to Pittard 2010). The predicted excess of emission at millimeter wavelengths is expected to be variable and modulated by the orbital motion. Observations of WR 98 suggest variability at centimeter wavelengths, changing its spectral index from $\sim$0.26 to $\sim$0.64 in a period of $\sim$15 days. Such variability is unlikely to be related to the WCR component predicted from our model, and will be discussed in the next Chapter.

2.7 Summary and Conclusions

In this Chapter, we have presented a semi-analytical model for calculating the thermal contribution to the radio emission from a radiative WCR in massive binary systems. As we have described, the WCR in massive binary systems is expected to contribute to the total radio emission, with a non-thermal and/or a thermal component. For close binary systems, the non-thermal emission is expected to be absorbed by the dense surrounding material from the stellar winds, and their radio spectrum is thought to be composed only by the thermal emission from the unshocked winds. However, it has been shown that free-free thermal emission from the WCR may also contribute to the total radio spectrum, being more important for close binary systems.

In radiative systems, the two-shock structure resulting from the two-wind interaction, collapses onto the contact surface between the shocks. In this case, the shock structure can be approximated by a thin-shell bounded by two isothermal shocks. Based on considerations of linear and angular momentum conservation, we developed a formulation for calculating the emission measure under a thin-shell approximation. From this model, simple predictions of the

radio spectrum can be made. We have found that most of the thermal radio emission from the shell arises from the optically thick material, with an intrinsic flux density with an spectral index $\sim$ 1.1. Thus, the contribution of a radiative WCR would be detected as an excess of emission at high frequencies, with respect to that expected from a single stellar wind. Using typical parameters of massive WR+O binaries, we found that the thin shell may contribute to the total spectrum of radiative close systems, becoming more significant as the binary separation increases, with the flux density scaling as $D^{4/5}$. This result contrasts with the adiabatic case, for which the hot material within the WCR remains optically thin, with an spectral index ~ -0.1, and the flux density scales as D^{-1} (Pittard et al. 2006). Our results resemble those steep radio spectra inferred from observations of WR stars (see next Chapter). In particular, we applied the model to the close binary system WR 98, and predict an excess of emission at high frequencies that seems to be in agreement with millimeter observations reported for this source.

Our results are in agreement with those presented by Pittard (2010) from hydrodynamical simulations of an O+O-type radiative system. He found that most of the material within the shock remains optically thick with a steep spectral index $\sim$ 1.5 from frequencies $\sim$100 GHz. In addition Pittard (2010) also investigated the variability of the flux density as a result of the orbital motion. Comparing with their results, we conclude that the geometry assumed for our model corresponds to an orbital phase with a minimum for the WCR contribution. Therefore, our model represents a simple and useful method to determine if a minimum for a WCR is expected to be detected from observations. Since other factors (as deviations in the wind parameters from that assumed for a standard wind) may also result in high values of the spectral indices, we propose the detection of variability as the most promising way to unambiguously determine the contribution of a radiative WCR.

Finally we point out that our model cannot be properly applied to those close systems where the winds collide within the acceleration zone, and future models are required to investigate its influence over the spectrum. This is specially required, since in such close systems the cooling is expected to be even more efficient, owing to the lower values of the preshock velocity, which favor the radiative cooling. Furthermore, in close systems, the orbital motion changes the shape of the WCR due to Coriolis forces that results in spiral structures. These effects require to be investigated by performing 3D hydrodynamical simulations of radiative shocks in colliding winds, which will be presented in a future work.

3

Observations of Stellar Winds from Wolf-Rayet Stars

Wolf-Rayet (WR) stars display strong stellar winds, forming a dense and expanding envelope that is ionized by the hot central star. These winds emit free-free thermal emission detectable at radio frequencies with the flux density growing with frequency with a spectral index $\alpha \approx 0.6$ ($S_\nu \propto \nu^\alpha$). However, several processes have been found to change the spectral index from this "standard" value. In particular for binary stars, a wind-wind collision region (WCR) between the stars may contribute with an extra component to the total emission, being thermal and/or non-thermal emission, affecting the spectrum from low to high frequencies. Through multi-frequency observations it is possible to characterize the spectrum and disentangle the processes and contributions that could be affecting it. In this chapter we present radio observations of a sample of 14 Wolf-Rayet stars, aimed to characterize their radio emission in the frequency range from 1.4 GHz to 250 GHz. Two of these stars were observed with the GMRT at 1.4 GHz, 13 stars with the VLA at 4.8, 8.4, and 23 GHz, and six with the IRAM 30 m telescope at 250 GHz. In particular, we discuss the possible influence of a WCR over the total spectrum of binary stars. We found evidence of such influence for nine stars previously identified as binary systems. Furthermore, for ten of the stars in the sample, we found indications of a non-thermal contribution. On the other hand, two stars show hints of an excess of emission at high frequencies. Thus, this work presents observational evidence of the influence of a binary companion over the radio spectrum even for close binaries, for which only a single stellar wind spectrum has been expected to be detected. Finally, we remark the importance of characterizing the spectrum over a wide range of frequencies in order to properly identify all the contributions that may impact the spectrum.

3.1 Introduction

Wolf-Rayet (WR) stars are evolved and massive objects that result from the high mass loss of O type stars. In this stage of evolution, the star continues losing material via strong stellar winds, with parameters up to one order of magnitude higher than those of the winds from their O star

precursors. In this way, WR stellar winds display high mass-loss rates, $\dot{M} \sim 10^{-5}\,\mathrm{M_\odot\,yr^{-1}}$, and high terminal velocities, $v_\infty \sim 1000 - 2500\,\mathrm{km\ s^{-1}}$. These stellar winds reveal themselves at several frequency ranges, for example by tracing the terminal velocity in the P Cygni profiles in UV (e.g. Crowther et al. 1995), or showing an excess of emission at IR and radio frequencies (e.g. Abbott et al. 1986). At radio frequencies, the emission is associated with the contribution of the free-free thermal emission arising from the ionized and expanding envelope formed by the stellar wind. Early studies by Panagia & Felli (1975), and Wright & Barlow (1975) found that the thermal radio spectrum of an ionized, spherically symmetric, and steady wind with an electron density profile, $n_e \propto r^{-2}$ (r being the distance from the central star), follows a power-law with frequency, $S_\nu \propto \nu^\alpha$, with a positive spectral index $\alpha \approx 0.6$ (hereafter this stellar wind is referred to as the "standard" wind). These authors also derived a simple and useful relation between the flux density S_ν and the mass-loss rate $\dot{M}$ of the star. In this way, in the last years, multi-frequency radio observations have been used to determine spectral indices and characterize the spectrum of a large sample of WR stars (Abbott et al. 1986, Leitherer et al 1995, 1997, Chapman et. 1999, Contreras et al. 2004, Cappa et al. 2004). These studies have revealed spectral indices with negative, flat ($\alpha \sim 0$), or even steeper ($\alpha > 0.6$) values than that one expected for the standard wind spectrum.

The $\alpha > 0.6$ values have been explained as the result from deviations in the wind conditions from those assumed for a standard wind, such as clumps and/or changes in the ionization state (Leitherer et al. 1991, Nugis et al. 1998). On the other hand, negative and flat indices are thought to be an indication of a composite spectrum, with a thermal plus a non-thermal contribution. The non-thermal emission is thought to be synchrotron emission produced by relativistic electrons, which have been accelerated either in strong shocks within the stellar wind, for single stars (White 1985), or in a wind-wind collision region (WCR) between the stellar components in binary systems (WR+0; Usov 1992, Eichler & Usov 1993). Recently, theoretical (Van Loo, 2005) and observational (Dougherty & Williams, 2000) studies suggest that negative or flat spectra, resulting from synchrotron emission, could only be originated in colliding wind binaries (CWB). Thus, a non-thermal spectrum appears to be strongly related to the binary condition of the source. Dougherty and Williams (2000) analyzed the radio spectra of a sample of 23 WR binary stars, and found that those binaries with orbital periods P >1 year exhibit a non-thermal spectrum, and those with shorter periods exhibit a thermal one. In this way, the origin of the non-thermal emission from the WCR in wide systems (P >1 year) has been supported by theoretical (e.g. Eichler & Usov 1993, Dougherty et al. 2003) and observational studies (e.g. WR 147, Williams et al. 1997; WR 140, Dougherty et al. 2005). On the other hand, for close binaries ($P < 1$ year), it is unlikely that the non-thermal emission from the WCR could be detected, since in these systems the synchrotron emission is expected to be fully absorbed by the dense WR stellar wind (Dougherty & Williams 2000). Hence, for these sources, their spectra have been thought to be composed only by the thermal emission from the stellar winds, without any influence due to their binarity.

Nevertheless, theoretical studies suggest that the thermal emission from the WCR might also have an important, yet not dominant, contribution to their total emission, being more relevant as the stars become closer the one to the other (Stevens 1995). Recent studies have shown that

the thermal spectrum of a WCR in massive binary systems will be highly dependent on the nature of the shock, with a spectral index ~ -0.1 for adiabatic and optically thin (Pittard et al. 2006), and up to ~ 1.5 for radiative and optically thick WCR (Pittard 2010; Chapter 2). Thus, even for close systems, the WCR is likely to impact the resulting radio spectrum for a wide range of the radio spectrum, from low to high frequencies. However, for such close systems, there is a lack of multi-frequency observations aimed to analyze their radio spectra and to determine any possible influence of its binarity over them.

In the next sections we present radio observations of a sample of WR stars for a wide range of frequencies, from 1 to 250 GHz. For this purpose, we have used three different instruments: the GMRT at 1.4 GHz, the VLA at 5, 8.4, and 22 GHz, and the IRAM 30-m radio telescope at 250 GHz. First we will discuss the information obtained from the VLA and GMRT observations (intermediate-low frequencies; Section 3.2), and then we discuss the results from our high frequency observations (Section 3.3). From the high frequency observations we look for the observational evidence of the theoretic results presented in Chapter 2. In particular, we focus on the possible detection of the WCR in close binary systems, for which its binarity has been thought not to affect their radio spectra. Furthermore, we present new observations and analyze the spectrum of two single stars previously classified as non-thermal sources.

3.2 Centimeter Observations

The study of stellar winds from massive stars at intermediate frequencies (1-40 GHz; centimeter observations) has been the most common method to characterize their spectra and determine their $\dot{M}$ (e.g. Abbott et al. 1986, Contreras & Rodriguez 1999, Chapman et al. 1999). At this frequency range it has been possible to detect and disentangle both thermal and non-thermal spectra. Furthermore, through high angular resolutions (see Section 1.), it has been also possible to resolve the two emission components within one system: the non-thermal from the WCR, and the thermal from the unshocked stellar wind (e.g. WR 147, Williams et al. 1997, Contreras & Rodriguez, 1999; see Figure 1.11). Although for close systems it is unlikely to resolve the two emitting regions, spectral index determinations from simultaneous multi-frequency observations allow to characterize the spectrum and identify any possible effect of an emission component from a WCR.

3.2.1 The Sample

In this section, we present simultaneous, multi-frequency observations of a sample of 13 WR stars (Table 3.1), using the VLA at 4.8, 8.4, and 23 GHz, and the GMRT at 1.4 GHz. The main goal of this work is to detect the influence of the WCR in close WR systems. Nine of the stars are close systems ($P \lesssim$ few months) previously detected at least at one radio frequency (WR 8, 12, 113, 133, 138, 141, 156). We also observed WR 98a and WR 104, in order to detect any variability that allows us to confirm the non-thermal nature of their radio spectrum. These two sources are well known by its IR spiral structure (the so-called pinwheel nebula; see Section 1.3.1), and their non-thermal radio emission seems to be severely affected by free-free absorption from the WR winds, even when their orbital periods are higher than 1 year (Monnier

Table 3.1. Wolf Rayet Sample and their Properties

WR	Spectral Type	Binary Status	P (days)
8	WN7/WCE+?	SB1	38.4,115
12	WN8h+?	SB1,no d.e.l.	23.92
79a	WN9ha	VB	...
89	WN9h+OB	a,d.e.l.,VB	...
98	WN8/WC7	SB1	48.7
98a	WC8-9vd+?	CWB	565
104	WC9d+B0.5V	SB2,VB	243
105	WN9h	...	...
113	WC8d+O8-9IV	SB2	29.7
133	WN5+O9I	SB2,VB	112.4
138	WN5+B?	SB2,VB	11.6,1538
141	WN5+O5V-III	SB2	21.6
156	WN8h+OB?	d.e.l.	6.5,10

Note. — The values displayed in the columns were taken from the van der Hucht (2001) WR catalog. SB:Spectral Binary; VB: Visual Binary; a: absorption; d.e.l. diluted emission lines; CWB Colliding Wind Binary.

et al. 2000). We add two single stars previously classified as non-thermal radio sources (WR 79a and WR 105), in order to corroborate the nature of their spectra by detecting variability in their emission. Furthermore, in order to confirm the hints of non-thermal emission from the VLA observing frequencies of WR 98 and WR 79a, we extend these observations to lower frequencies. Thus, we present 1.4 GHz observations with the GMRT towards these two sources.

From these observations we aimed at disentangling the origin of their stellar wind radio emission through the analysis of their spectral indices and time variability by comparison with previous observations. We first describe the observations taken with each instrument. Next, we show our results and classification of the emission nature. For WR 98 and WR 79a, we jointly analyzed the observations from the VLA and GMRT. We also present $\dot{M}$ estimates for each of the stars detected in our sample. Finally, we discuss our results, by describing the possible scenarios that are likely to produce the observed spectrum.

3.2.2 Observations

3.2.2.1 The Very Large Array

We performed radio observations at intermediate frequencies with the Very Large Array (VLA) of the National Radio Astronomy Observatory (NRAO)[1] . This radio interferometer is located in New Mexico (United States of America) and consists of 27 radio antennas of 25 meter diameter each. The antennas are distributed along a three-arm array describing a Y-shape. The resolution of the VLA is set by the size of the array, with a maximum separation between the antennas of 1 km (D configuration), 3.6 km (C configuration), 10 km (B configuration), and 36 kilometers (A configuration). This allows to reach angular resolutions up to 8.4" for D configuration and up to

[1]The NRAO is a facility of the National Science Foundation operated under cooperative agreement by Associated Universities, Inc.

0.23" for A configuration (at a frequency of 8.4 GHz). The VLA receivers operate at eight bands (0.074, 0.32, 1.4, 4.8, 8.4, 15, 23, and 43 GHz; wavelengths from 400 to 0.7 cm). Recently, the VLA was transformed into the Expanded Very Large Array (EVLA). This transformation has enhanced the instrument sensitivity and frequency range, by extending the receivers bandwidth, and installing a new appropriate correlator. During our observations EVLA antennas were included. However, the instrument was still operating as the "old" VLA.

Calibration

Two sets of observations were performed in 2007 while the VLA was in D configuration: we observed five sources on April 21 at 4.8 and 8.4 GHz, and three additional sources on May 6 at 4.8, 8.4, and 23 GHz. In March 2008, we observed seven sources with the VLA in C configuration: five of them were new sources and the other two were also observed in 2007 (WR 79a and WR 105). We should note that the VLA configuration was not relevant for our purposes, since we were interested only in the flux density of the stars, whose size is not resolved at any VLA configuration.

Data editing and calibration were carried out using the NRAO Astronomical Image Processing System (AIPS) package, following standard VLA procedures. Absolute flux calibration was achieved by observing 3C 48 and 3C 286. During the observations EVLA antennas were included, thus it was necessary a baseline calibration in order to correct the differences between the VLA and EVLA receivers. For WR 105, self-calibration at 23 GHz allowed us to improve the phase calibration for this source. However, for the rest of the sources we could not perform self-calibration due to the weakness of the sources. Expected off-source rms of ~ 50 and $\sim 40\mu$Jy/beam at 4.8 and 8.4 GHz respectively, and $\sim 60\mu$Jy/beam at 23 GHz, were successfully achieved for most of the sources, with an on-source time of 15 minutes at 4.8 and 8.4 GHz respectively, and of 30 minutes at 23 GHz. However, the observations of WR 79a, 89, 104, and 105, which were obtained with the VLA in D configuration, suffered from side-lobe contamination, resulting in an increase of the rms noise. We improved the rms of those images by excluding the shorter baselines in the AIPS-IMAGR (UVRANGE=3,0). We used the AIPS-IMFIT procedure in order to fit the position and flux density of the detected sources. Since the sources are not expected to be resolved, we fixed in IMFIT the standard parameters for unresolved sources. We took a box size approximately twice the beam size of each image. This procedure fits a 2D-Gaussian to the sources and estimates the position of the maximum, the total flux density, and the errors of these estimates. The error estimated by IMFIT considers both the quality of the fit and the image rms.

We present in Figure 3.1 contour images for the 12 detected sources (including marginal detections at $3\,\sigma$). In Table 3.2 we present the position, total flux density, and spectral indices obtained for the 12 detected sources. The flux density uncertainties were calculated considering both the IMFIT error estimates and 2% calibration uncertainties at 4.8 and 8.4 GHz, and 5% at 23 GHz. Note that the rms noise of the image is the dominant contribution to the error budget. The upper limits of the undetected sources were taken as three times the rms noise.

We also used unreported archival VLA data for WR 105 and WR 133, searching for a possible variability in their radio emission which would indicate a likely non-thermal origin.

Table 3.2. Radio Flux Densities and Spectral Indices

Source	Observation	Positions at 8.4 GHz (J.2000.0)			Fluxes (mJy)			
WR No.	Date	R.A.	Dec.	Error	4.8 GHz	8.4 GHz	23 GHz	α
79a	07-Apr-21	16 54 58.51	-41 09 04.3	0.4	0.86±0.07	1.67±0.06	...	1.16±0.16
89	07-Apr-21	17 19 00.53	-38 48 52.0	0.2	1.82±0.24	3.01±0.08	...	0.88±0.24
98	07-May-06	17 37 13.82	-33 27 55.4	0.3	0.94±0.06	1.09±0.05	...	0.26±0.14
98a	07-May-06	17 41 13.12	-30 32 32.0	1.0	<0.39	0.59±0.06	...	>0.73
104[a]	07-May-06	18 02 04.31	-23 37 41.4	0.8	<0.21	0.42±0.09	...	>1.22
105	07-May-06	18 02 23.44	-23 34 37.5	0.1	2.51±0.11	4.38±0.12	...	0.98±0.09
98	07-May-06	17 37 13.75	-33 27 54.9	0.4	0.58±0.06	1.18±0.05	1.94±0.15	0.64±0.07
133	07-May-06	20 05 57.25	+35 47 18.2	0.4	<0.41	0.31±0.03	0.57±0.07	0.60±0.15
138	07-May-06	20 17 00.01	+37 25 23.7	0.2	<0.12	0.52±0.03	1.15±0.08	>0.82
8	08-Mar-07	07 44 58.19	-31 54 30.0	0.3	0.22±0.04	0.28±0.03	0.30±0.05	0.17±0.15
12[a]	08-Mar-07	08 44 47.18	-45 58 55.9	7.8	<0.22	...	...	...
79a	08-Mar-05	16 54 58.49	-41 09 03.0	0.1	0.99±0.04	1.56±0.05	2.31±0.14	0.54±0.05
105[b]	08-Mar-05	18 02 23.46	-23 34 37.4	0.1	4.22±0.13	...	7.63±0.39	0.38±0.04
113	08-Mar-05	18 19 07.36	-11 37 59.3	0.1	0.22±0.03	0.47±0.04	1.27±0.07	1.06±0.09
141	08-Mar-08	20 21 31.73	+36 55 12.8	0.1	0.59±0.04	1.28±0.04	2.86±0.15	0.91±0.05
156	08-Mar-08	23 00 10.15	+60 55 38.4	0.1	0.77±0.04	0.99±0.04	1.59±0.09	0.46±0.05

Note. — Upper limits of the undetected sources were fixed at three times the rms noise of the map. For WR 133 at 4.8 GHz the upper limit was fixed from the peak of the unresolved emission. The α errors were estimated from, $\Delta\alpha^2 = [(\partial\alpha/\partial S_1)\Delta S_1]^2+[(\partial\alpha/\partial S_2)\Delta S_2]^2$, for two frequency determinations of α, and from the error of the weighted linear regression fit used for the three frequency determinations. See Section 2 for details about the error of the flux densities determinations. Lines separate the observing epochs.

[a]Probable detection. Coordinates refer to the local maximum position at 4.8 GHz for WR 12 and at 8.4 GHz for WR 104, both close to the optical positions.

[b]Position at 23 GHz.

For WR 105 we used VLA observations in B configuration taken on November 20, 1999 at 1.4, 4.8, and 8.4 GHz, and on November 27, 1999 at 4.8, 8.4 and 15 GHz. For WR 133, we analyzed observations on May 31, 1993 at 1.4, 4.8, and 8.4 GHz, when the VLA was in BC configuration. We calibrated these archival data following the same procedure used for our observations, reaching similar values for the rms noise. For WR 105, self-calibration could be performed at any of the observed frequencies.

3.2.2.2 The Giant Metrewave Radio Telescope

Observations at 1.4 GHz toward WR 79a and WR 98 were performed with the Giant Metrewave Radio Telescope (GMRT). The GMRT is located about 80 km north of Pune in India, and consists of 30 antennas of 45 m of diameter each. From these antennas, 14 are located more or less randomly in a compact central array in a region of about 1 km^2. The remaining 16 antennas are spread out along the three arms of an approximately Y-shaped configuration over a much larger region, with the longest interferometric baseline of about 25 km. The interferometer operates in six frequency bands centered around 50, 153, 233, 325, 610 and 1420 MHz. For some frequency configurations, dual-frequency observations are also possible. The highest angular resolutions achievable for the GMRT range from $\sim$ 60" at the lowest frequencies to $\sim$ 2" at 1.4 GHz.

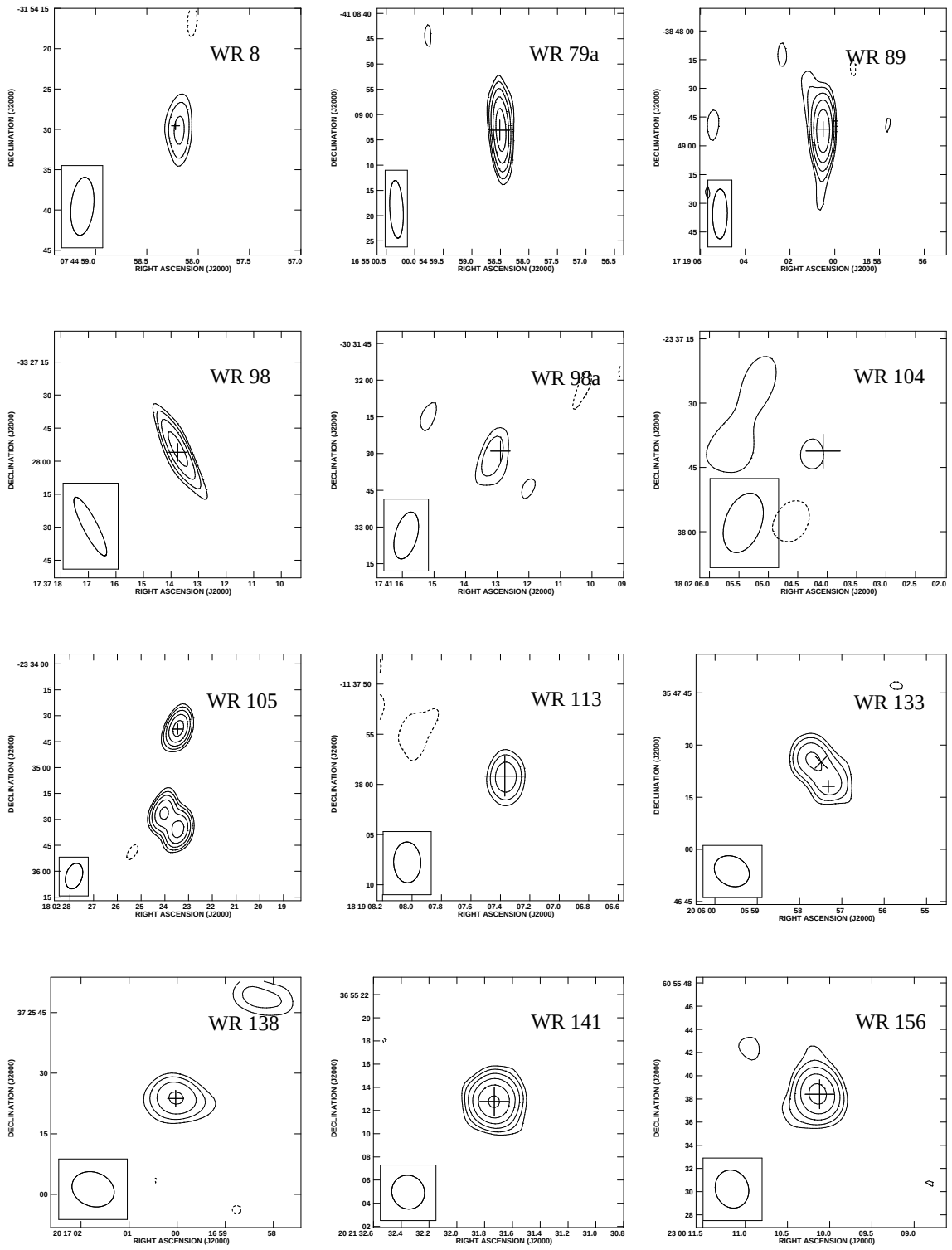

Figure 3.1 Contour images for the 12 WR stars detected at 8.4 GHz, including the tentative detection of WR 104 at $3\,\sigma$. Contour lines are -3, 3, $3\sqrt{3}$, 9, ... the rms noise. The rms noise is ~ 50 μJy, except for WR 104 and WR 105 for which is $\approx$2 times higher, owing to their low declinations and the influence of extended sources within the field of view. The synthesized beam is drawn at the bottom left of each image. In each panel, the plus sign marks the optical positions of the star (we note that the size does not represent the uncertainty in the position). The cross-sign in the WR 133 image marks the peak of the emission at 4.8 GHz.

Calibration

Observations at 1.4 GHz were performed during 2007 at four epochs: October 29, November 16, December 8 and December 21. WR 98 was observed in all the epochs, while WR 79a was only observed during November 16. We used the same flux and phase calibrators in all epochs, 3C286 and 1626−298, respectively. Data editing and calibration were carried out using the AIPS package developed by the NRAO. Observations were performed with a bandwidth of 16 MHz covered by 128 channels. Bandpass calibration was applied using the absolute flux calibrator over 96 central channels. Because of the high contamination from interference signals at these low frequencies, a more careful editing process was required. After the editing process, all channels were combined into a single channel. The resulting single channel data were then calibrated following the standard process for continuum observations.After this calibration, data from each epoch were self-calibrated using the brighter sources present in the field. Finally, we made natural weighting maps for each epoch. In all epochs, we note that strong side-lobes are present. This effect is probably related with a poor uv-coverage. In order to obtain a higher quality map, we stacked the uv data from all observing epochs of WR 98. With this procedure, we obtained a map with reduced side-lobe effects, and a rms noise of ~ 0.08 mJy/beam for both WR 98 and WR79a. From these maps, we did not detect neither WR 79a nor WR 98, and only an upper limit to the flux density of 0.3 mJy ($\sim 3 \times \sigma$) was determined for both sources. In Figure 3.2 we present an image of the WR 98 map. Several field sources were detected from these observations, and as an example we show a double source detected at the northwest of the WR 98 optical position.

3.2.3 Disentangling the Nature of the Radio Emission in WR Stars

3.2.3.1 Spectral Index Estimates

We observed a total of 13 WR stars and detected 12 of them at least at one frequency. In Table 3.2 we present the flux densities of the detected sources at each observed frequency, as well as upper limits for the undetected sources. All the sources observed with the VLA were observed quasi-simultaneously at different frequencies on the same day; six of them were observed in this mode for the first time (WR 8, 98, 113, 138, 141 and 156). Due to the observed flux density variability for this kind of sources, we point out the importance of the simultaneity in order to correctly determine their spectral index. Using this approach, we derived spectral indices for the eight sources detected at all observing frequencies. We also derived lower limits for the spectral indices of the remaining four sources that were detected at least at one frequency, but with only a flux density upper limit at another. When only two frequencies were available, the spectral index was determined using the expression

$$\alpha = \frac{\log(S_{\nu_1}/S_{\nu_2})}{\log(\nu_1/\nu_2)}. \tag{3.1}$$

Otherwise, when three frequencies were available, we used a linear regression fit weighting each data point by its error. For WR 133 we have not used the data at the lower frequencies to determine its spectral index. The archival data at 1.4 GHz had a large rms noise, which

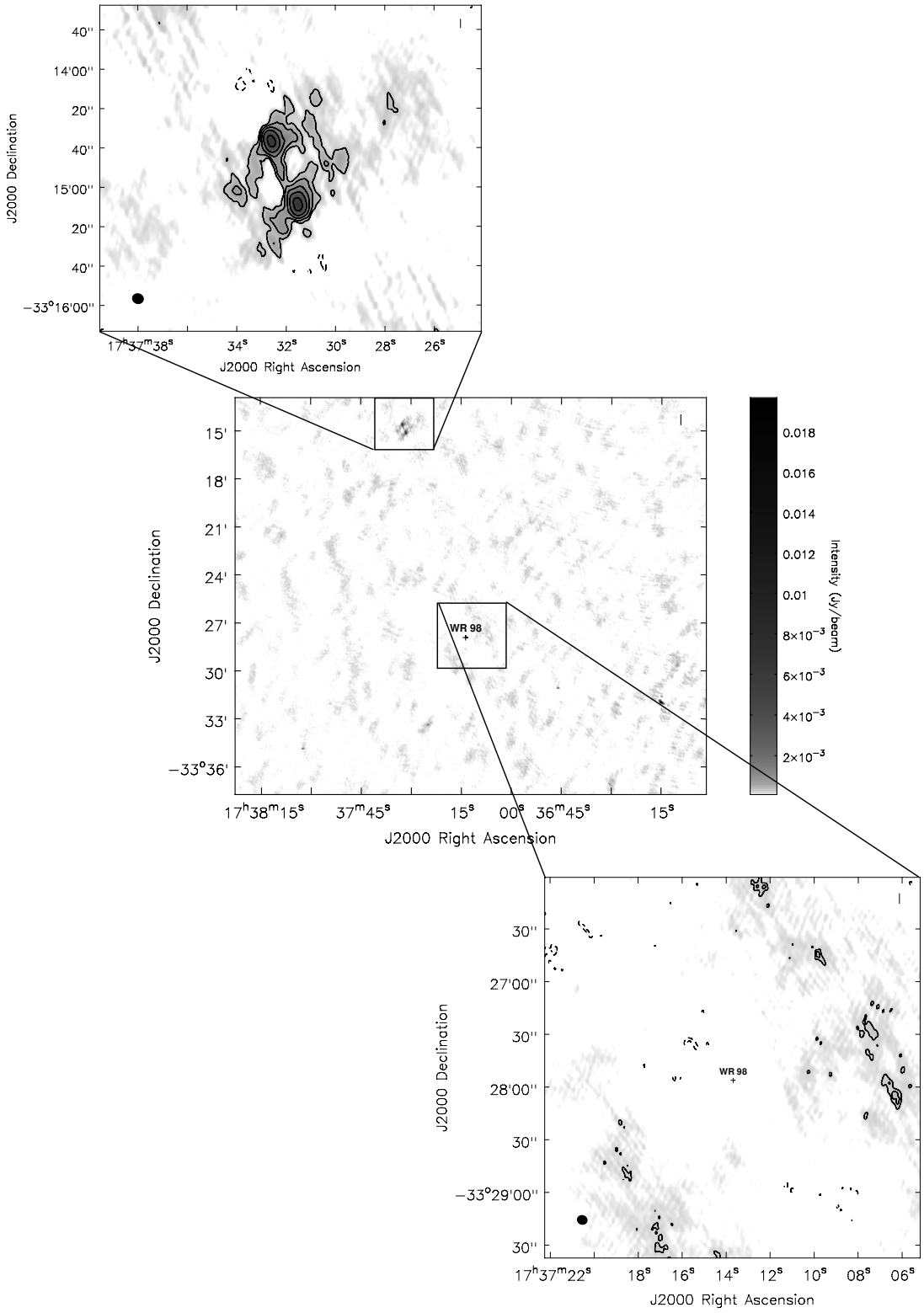

Figure 3.2 Contour images from the field resulted from the GMRT observations at 1.4 GHz towards WR 98.'+' sign marks the optical position of WR 98. In the bottom image we present the zoom of the field, centered in the WR 98 position. The top panel shows a double source detected at the northwest of the WR 98 optical position. Contour lines in bottom and top panels are 4, 8, 16, 32, 64, 128 the rms noise. In the middle image, contour lines are 3,4,5,6 the rms noise. We plot different contour lines in order to make clear the images. The rms noise is ~ 80 μJy for all the images. The synthesized beam is drawn at the bottom left of each image.

prevented us from fixing a reliable upper limit for its flux density. On the other hand, our 4.8 GHz data did not allow us to determine an upper limit to the flux density, since WR 133 is perturbed by the unresolved emission of a source at the northeast of the WR 133 position. From the upper limits inferred from the GMRT observations of WR 98 and WR 79a, we derived lower limits for the spectral index between 1.4 GHz and 4.8 GHz. For WR 98, for which variability at 4.8 GHz was observed, we determined two values for the lower limit of the spectral index by using the two different flux densities obtained at this frequency. In Table 3.3 we present only the highest value of these determinations.

3.2.3.2 Spectrum Classification

Thermal stellar winds are expected to have spectral indices ~ 0.6 (Wright & Barlow, 1975; Nugis et al. 1998). On the other hand, in the case of non-thermal WR stars, the contribution of the thermal emission from the stellar winds combined with a non-thermal component from the WCR, will result in a total spectrum characterized by spectral indices < 0.6 (e.g. Eichler & Usov 1993). This non-thermal emission is expected to be modulated by the orbital motion of the system, resulting into a variability of the total spectrum (e.g. WR 140; Dougherty et al. 2005) with a periodicity related to the orbital period.

In order to classify the nature of the WR radio emission, we have determined i) the spectral index for each source and observing epoch and ii) the presence of variability by comparing all the flux density measurements from the different observing epochs. We considered the existence of flux density variability when the differences in the flux densities between two or more epochs were higher than 3σ. For the spectral index, we used a conservative $3\,\sigma$ criterion as a significant difference. Optically-thin thermal emission (for which ≈ -0.1) from a single stellar wind is not expected for these massive stars at these frequencies (Dougherty & Williams, 2000). In this way, we classified our sources as follows:

- Thermal (T; free-free thermal emission): sources with a spectral index $\gtrsim 0.6$ for all observing epochs.
- Non-thermal (NT; dominant non-thermal emission): sources that showed a spectral index $\lesssim -0.1$ for at least one observing epoch, as well as variability in their emission.
- Composite (T/NT; thermal+non-thermal): sources that presented spectral indices higher than -0.1 but flatter than 0.6 (for at least one observing epoch), as well as variability in their emission.

Applying these criteria to the spectral indices and flux densities determined from these and previous observations, we found that at least four sources are T (WR 89, 113, 138, and 141), one is NT (WR 105), and three present a T/NT behavior (WR 8, WR 79a, and 156).

For the rest of the sources we have relaxed those criteria (WR 98, 98a, 104, and 133), since their strict application would mask important characteristics of these sources. In any case, we would assume them as T/NT. For WR 98a and WR 104, we have also considered the modeling of the emission presented by Monnier et al. (2002), and classified them as T/NT sources.

Table 3.3. Radio Flux Densities and Spectral Index Comparison with Previous Observations

WR	$S_{1.4\,\mathrm{GHz}}$ (mJy)	$S_{2.4\,\mathrm{GHz}}$ (mJy)	$S_{4.8\,\mathrm{GHz}}$ (mJy)	$S_{8.4\,\mathrm{GHz}}$ (mJy)	$S_{15\,\mathrm{GHz}}$ (mJy)	$S_{23\,\mathrm{GHz}}$ (mJy)	α	Obs Date	Ref.	Spec. Type
8	...	...	...	0.36±0.03	...	...	...	01Nov12	CG04	
	...	...	0.22±0.04	0.25±0.03	...	0.30±0.05	0.17±0.15	08Mar05	TS	(T/NT)[a]
12	...	...	...	0.51±0.06	...	...	...	01Nov12	CG04	
	...	...	<0.22	...	...	...	...	08Mar05	TS	
79a	...	...	1.1±0.1	...	2.4±0.1	...	0.9±0.1	84Apr03	BA89	
	...	1.0±0.1	0.8±0.1	0.9±0.1	...	...	-0.1±0.1	Nov00	SC03	
	...	...	...	0.7±0.1	...	...	...	01Sep15	CG04	
	...	...	0.86±0.07	1.67±0.06	...	...	1.16±0.16	07Apr21	TS	
	...	...	0.99±0.04	1.56±0.05	...	2.31±0.14	0.54±0.05	08Mar05	TS	(T/NT)[a]
	<0.3	...	...	...	...	...	>0.9 [e]	07Dec	TS	
89	...	...	0.6±0.1	...	...	...	...	82Aug20	AB86	
	...	...	1.94±0.19	2.99±0.10	...	...	0.76±0.18	94Sep08	LC95	
	<1.20	<0.90	...	...	...	...	...	97Feb23	CL99	
	...	...	...	2.0±0.1	...	...	...	01Nov12	CG04	
	...	...	1.82±0.52	3.01±0.09	...	...	0.88±0.24	07Apr21	TS	(T)[a]
98	...	...	0.9±0.07	...	...	...	...	85Aug17	AB86	
	...	...	0.94±0.06	1.09±0.05	...	...	0.26±0.14	07Apr21	TS	
	...	...	0.58±0.06	1.18±0.05	...	1.94±0.15	0.64±0.07	07May06	TS	(T/NT?)[c]
	<0.3	...	...	...	...	...	>0.8 [e]	07Dec	TS	
98a	<0.36	...	0.37±0.07	0.60±0.05	0.64±0.11	0.57±0.10	0.30±0.22	00Feb24	MT02	
	...	...	...	0.47±0.05	...	...	...	01Oct08	CG04	
	...	...	<0.39	0.59±0.06	...	...	>0.73	07Apr21	TS	(T/NT)[b]
104	...	...	<0.4	...	...	...	...	84Apr04	AB86	
	...	...	<2.01	<0.39	...	...	...	94Sep07	LC97	
	<1.59	<0.99	...	...	...	...	...	97Feb23	CL99	
	<0.30	...	...	0.87±0.06	1.02±0.12	0.94±0.10	0.10± 0.23	00Feb25	MT02	
	...	...	...	0.54±0.06	...	...	...	01Nov12	CG04	
	...	...	<0.21	0.42±0.09			>1.22	07Apr21	TS	(T/NT)[b]
105	...	...	3.6±0.2	...	...	...	...	84Apr04	AB86	
	...	...	4.39±0.15	3.75±0.15	...	...	-0.28±0.01	94Sep07	LC97	
	<1.17	<0.69	...	...	...	...	...	97Feb23	CL99	
	1.43±0.20	...	2.92±0.08	4.77±0.10	...	...	0.81±0.04	99Nov20	TS	
	...	...	2.73±0.07	...	7.02±0.37	...	0.83±0.05	99Nov27	TS	
	...	...	...	5.4±0.1	...	...	...	01Nov12	CG04	
	...	...	2.51±0.11	4.38±0.12	...	...	0.98±0.09	07Apr21	TS	
	...	...	4.22±0.13	...	...	7.63±0.39	0.38±0.04	08Mar05	TS	(NT) [a]
113	...	...	≤0.4	...	...	...	...	80Jul26	BA82	
	...	...	<0.80	<0.80	...	...	...	94Sep07	LC97	
	<2.25	<0.90	...	...	...	...	...	97Feb23	CL99	
	...	...	...	0.75±0.04	...	...	...	01Nov12	CG04	
	...	...	0.22±0.03	0.47±0.04	...	1.27±0.07	. 1.06±0.09	07May06	TS	(T)[a]
133	...	...	<0.3	...	...	...	...	85Aug17	AB86	
	<0.81	...	0.38±0.08	0.27±0.03	...	...	-0.65±0.42	93May31	TS	
	...	...	...	0.36±0.03	...	...	...	01Nov12	CG04	
	...	...	<0.41	0.31±0.03	...	0.57±0.07	0.60±0.15	07May06	TS	(T/NT?)[d]
138	...	...	0.6±0.1	...	...	...	...	80Jul27	BA82	
	...	...	<0.12	0.52±0.03	...	1.15±0.08	>0.82	07May06	TS	(T)[a]
141	...	...	0.6±0.1	...	...	...	...	85Aug05	AB86	
	...	...	0.59±0.04	1.28±0.04	...	2.86±0.15	0.91±0.05	08Mar05	TS	(T)[a]
156	...	...	...	1.06±0.03	...	...	...	01Nov12	CG04	
	...	...	0.77±0.04	0.99±0.04	...	1.59±0.09	0.46±0.05	08Mar05	TS	(T/NT)[a]

Note. — The whole frequency range observed was used for the spectral index and lower limits determinations, except for WR 133, for which the upper limits of the flux densities at the lower frequencies were not taken into account.
For all the sources spectral classification was done over the whole group of observations. (T) Thermal. (NT) Non-thermal. (T/NT) Composite, thermal+non-thermal. (T/NT?) tentative composite.
Spectral classification criteria used:

[a] According to the criteria described in section 3.2.

[b] Study presented in MT02

[c] According to the criteria described in section 3.2 and the short time variability ∼15 days in the density flux.

[d] According to the criteria described in section 3.2 and the flat tendency of the spectral index determination at the lower frequency range.

[e] Lower limits were derived from the upper limits at 1.4 GHz obtained from the GMRT observations, and the highest value of the flux density at 4.8 GHz.

References. — TS:This Study; BA82: Bieging et al. (1982); BA89: Bieging et al. (1989); SC03: Setia Gunawan et al. (2003); MT02: Monnier et al. (2002).

Table 3.4. Mass-Loss Rate Estimates

WR	Spectral Type	v_∞ ($\mathrm{km\,s^{-1}}$)	d (kpc)	μ	Z	γ	$S_{8.4\ \mathrm{GHz}}$ (mJy)	$\dot{M}_{8.4\ \mathrm{GHz}}$ $10^{-5}\,\mathrm{M_\odot\,yr^{-1}}$
8	WN7/WCE+?	1590	3.47	1.7	1.0	1.0	0.28	1.79
79a	WN9ha	935	1.99	2.6	1.0	1.0	1.56	2.67
89	WN9h+OB	1600	2.88	1.5	1.0	1.0	3.01	7.14
98	WN8/WC7	1200	1.9	3.7	1.0	1.0	1.09	3.30
98a	WC8-9vd+?	2000	1.9	4.7	1.1	1.1	0.59	4.03
104	WC9d+B0.5V	1220	2.3	4.7	1.1	1.1	0.42	2.54
105	WN9h	700	1.58	2.6	1.0	1.0	4.38	2.91
113	WC8d+O8-9IV	1700	1.79	4.7	1.1	1.1	0.47	2.64
133	WN5+O9I	1800	2.14	4.0	1.1	1.1	0.27	2.06
138	WN5+B?	1400	1.26	4.0	1.1	1.1	0.52	1.18
141	WN5+O5V-III	1550	1.26	4.0	1.1	1.1	1.28	2.57
156	WN8h+OB?	660	3.56	3.3	1.0	1.1	0.99	3.87

Note. — The logarithmic error in the $\dot{M}$ estimates are 0.21 for the stars considered in cluster/association, and 0.41 for the rest (WR 98, 98a, 104 and 156).

For WR 98, the first determination of the spectral index is not conclusive about its spectrum; therefore, we also have taken into account the short time variability (15 days, see Table 3.3) at 4.8 GHz as a plausible indication of a possible non-thermal emission and a tentative T/NT nature. For WR 133, it is difficult to infer a variability in the spectrum from the two spectral index determinations, since those were determined from different frequency ranges (see Table 3.3). However, we should point out that the observations at the lower frequency range of WR 133 shows a tendency towards a non-thermal spectrum in the 1993 epoch. Therefore, we classified WR 98 and WR 133 as tentative T/NT sources.

Summarizing, we have found four T (WR 89, 113, 138, and 141), one NT (WR 105), and seven T/NT sources (WR 8, 79a, 98, 98a, 104, 133, and 156).

3.2.3.3 Mass-Loss Rates

As we mentioned in Section 3.1, Panagia & Felli (1975) and Wright & Barlow (1975) by assuming standard winds conditions derived a general expression for the mass-loss rate, $\dot{M}$, in terms of observable quantities (see Section 1.2.1 for details),

$$\left[\frac{\dot{M}}{\mathrm{M_\odot\,yr^{-1}}}\right] = 5.34\times10^{-4}\left[\frac{S_\nu}{\mathrm{mJy}}\right]^{3/4}\left[\frac{v_\infty}{\mathrm{km\,s^{-1}}}\right]\left[\frac{d}{\mathrm{kpc}}\right]^{3/2}\left[\frac{\nu}{\mathrm{Hz}}\right]^{-1/2}\left[\frac{\mu^2}{Z\gamma g_\nu}\right]^{1/2}, \qquad (3.2)$$

where v_∞ is the terminal velocity of the stellar wind, d is the distance to the star, ν is the observed frequency, and g_ν is the free-free Gaunt factor. The parameters μ, Z and γ are the mean molecular weight, the average ionic charge, and the mean number of electrons per ion, respectively. In this way, radio observations have been one of most widespread methods for determining $\dot{M}$ (e.g. Leitherer et al. 1991, Contreras & Rodríguez, 1997).

In Table 3.4, we present $\dot{M}$ values by using equation (3.2) for the 12 sources of our sample detected at 8.4 GHz. At this frequency we detected most of the observed sources. Furthermore, at this intermediate frequency, we expect to minimize any effect from a possible WCR. Those

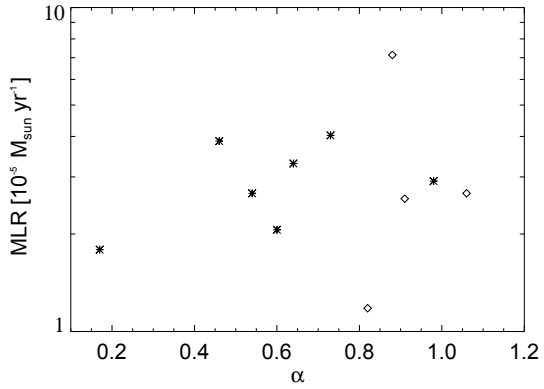

Figure 3.3 Mass loss rate estimates (MLR) vs. spectral indices α. '$\diamond$' represent the thermal sources and '$*$' those classified as NT and T/NT.

values were obtained by assuming a standard stellar wind with a filling factor, $f = 1$; we, however, note that deviations from such assumptions might lead into an overestimation of $\dot{M}$.

For the sources identified as T (WR 89, 113, 138, and 141), the spectral indices higher than 0.6 suggest an overestimation for these $\dot{M}$ estimates. On the other hand, for NT and T/NT sources, the additional contribution to the thermal stellar wind emission would also cause an overestimation. At this frequency the impact of any extra contribution is not expected to be significant (see Section 3.3.4). We found no relationship between the $\dot{M}$ and the spectral classification of the sources that would suggest any effect of the WCR to overestimate the $\dot{M}$ (see Figure 3.3). Thus, these estimates can be considered reliable.

The values μ, Z, and γ were taken from Cappa et al. 2004. For WR 138 and WR 141 we adopted the values of WR 133, since they share the same spectral type, WN5. We compute g_ν from equation (3) within Leitherer & Robert (1991), adopting T_e= 10^4 K (deviations from this temperature have minor effects on g_ν). The terminal velocities v_∞ and distances d of the stars were obtained from the van der Hucht (2001) WR catalog. We estimated the uncertainties for each parameter in Table 3.4 using the same criteria as in Leitherer et al. (1997). For the parameter d we assumed a 20% error based on the cluster/association membership of the star, otherwise 40% errors are assumed (0.09 and 0.25 dex, respectively). For the errors in v_∞ we assume 10% (0.04 dex). The error obtained in g_ν is about 10%. Finally, for μ, Z, and γ we assumed an error of $\pm$0.08 dex, as in Cappa et al. 2004. Therefore, following the equation (5) in Leitherer et al. 1997 for the $\dot{M}$ uncertainties, we obtained a typical logarithmic error of 0.21 for the stars considered in cluster/association and 0.41 for the rest (WR 98, 98a, 104, and 156).

We compared our results for $\dot{M}$ with those previously reported by Cappa et al. (2004): we calculated the average $\dot{M}$ for each of the main spectral types in the sample, $\dot{M}(\mathrm{WN}) = (3.05 \pm 2.21) \times 10^{-5}\,\mathrm{M_\odot\,yr^{-1}}$ and $\dot{M}(\mathrm{WC}) = (3.07 \pm 2.73) \times 10^{-5}\,\mathrm{M_\odot\,yr^{-1}}$, for WN and WC respectively. We found these values to coincide within the errors with those presented by Cappa et al. (2004; $\dot{M}(\mathrm{WN}) \sim 4 \times 10^{-5}\,\mathrm{M_\odot\,yr^{-1}}$ and $\dot{M}(\mathrm{WC8-9}) \sim 2 \times 10^{-5}\,\mathrm{M_\odot\,yr^{-1}}$; see Figure 3.4).

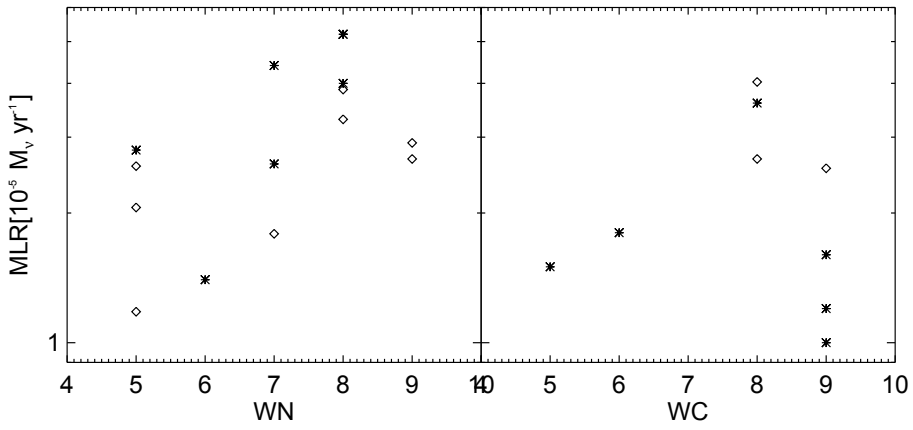

Figure 3.4 Comparison between our mass loss rate estimates ($\diamond$) and those presented by Cappa et al. (2004; $*$). We plot WR mass loss rates vs spectral subtype. '$\diamond$' represent our estimates and '$*$' those taken from Cappa et al. (2004). For this plot we have not considered the upper limits presented by these authors.

3.2.4 Discussion

The results of our observations provide relevant information about the nature of the radio emission of the 12 detected WR stars. As we have already mentioned, from the spectra classification of our sample, we have found flux densities and spectral indices α ($S_\nu \propto \nu^\alpha$), that indicate the existence of thermal, non-thermal dominant, and composite spectrum sources.

The Thermal Sources

For the sources identified as thermal (WR 89, 113, 138, and 141), we found spectral indices $\alpha \sim 1$. In a single star context, when the radio-continuum spectrum is consistent with thermal emission, the deviations from the expected 0.6 value for an isotropic wind (Panagia & Felli 1975; Wright & Barlow 1975) may be caused either by the presence of condensations (clumps) that produce a non-standard electron density profile ($n \propto r^{-s}$; with $s \geq 2$). Leitherer et al. (1991) found that changes in the ionization state of WR winds could also result in an increase of the spectral index. On the other hand, for close binary systems, although the non-thermal emission from the WCR is expected to be absorbed by the WR stellar wind, the hot and dense shocked gas within the WCR might be able to contribute to the thermal radio spectrum (Stevens et al. 1995, Pittard et al. 2006, Pittard 2010). Moreover, in this kind of systems, it is possible that the WCR turns radiative, resulting in a dense and optically-thick thermal emitting structure with a positive spectral index ($\gtrsim 1$; Pittard 2010, see Chapter 2). The cooling of the WCR can be quantified through the cooling parameter, which is defined as the ratio of the cooling time to the escape time for the material flow out of the shock region

$$\chi \approx 0.15 \left[\frac{v_\infty}{10^3\,\mathrm{km\,s^{-1}}}\right]^4 \left[\frac{d}{1\,\mathrm{AU}}\right] \left[\frac{\dot{M}_w}{10^{-5}\,\mathrm{M_\odot\,yr^{-1}}}\right]^{-1}, \tag{3.3}$$

where v_∞ and $\dot{M}$ are the terminal velocity and the mass loss rate of the WR star respectively, and d is the distance from the WR star to the WCR (Stevens et al. 1992; see Section 1.4 for details).

In this way, the WCR can be either radiative ($\chi < 1$) or adiabatic ($\chi \gtrsim 1$). For the binary thermal sources in our sample, $D < 1$ AU which implies $\chi < 0.5$, according to the stellar wind parameters given in Table 3.4. This suggests a radiative WCR with a thermal contribution to the spectrum, which might be able to increase its spectral index into such high values. Therefore, for WR 113, 138 and 141, although their high spectral indices (~ 1) might result from a clumpy single stellar wind, it is also possible that such spectral indices are also indicating the presence of a binary star system (see Section 3.3). Moreover, for WR 141 there seems to be evidence for the presence of a WCR region from observations at other frequencies (X-rays, Oskinova 2005, and spectral analysis, Moffat et al. 1996). Our high frequency observations presented in Section 3.3 give more information about the spectrum of WR 113 and WR 141.

The Non-thermal Emission from the Single Stars WR 79a and WR 105

On the other hand, the hints of non-thermal emission from the single stars WR 79a (T/NT) and WR 105 (NT) have no clear explanation. A non-thermal spectrum in WR stars seems to be closely related to the binary nature of the star. Dougherty & Williams (2000) analyzed the radio emission of a sample of 23 WR stars. They found that most sources with a non-thermal signature were binary systems, which suggests that binarity is intrinsically related to the detection of the non-thermal emission produced within the WCR between the two stellar components. However, WR 79a and WR 105 do not show any evidence of binarity (Marchenko et al 1998). Van Loo et al. (2006) presented a study of the non-thermal emission produced by wind-embedded shocks resulting from instabilities within a single O-type stellar wind (also applicable to WR stars). They found that the radial decline of the shock strength (velocity jump and compression ratio) produces a rapid decrease of the synchrotron emission, becoming negligible at those radii where the stellar wind becomes optically thin. This rules out the detection of a non-thermal spectrum for single stars. Moreover, as pointed out by Dougherty & Williams (2000), proving that a star is single is very difficult, and we cannot rule out the presence of a companion in these stars.

Since detectable non-thermal emission depends, in part, on the binary separation and the inclination angle of the system (e.g. WR 140 Dougherty et al. 2005), the detected flux density is expected to be modulated by the orbital motion, showing variability with a periodic behavior. Therefore, the observed variability in the spectra of WR 79a and WR 105 might be an indication of binary systems. Observations of WR 105 show variability in its 4.8 GHz flux density over a period of time of $\sim$14 yr. For WR 79a, the high value of the lower limit derived for the spectral index at low frequencies suggest the presence of a non-thermal component strongly affected by the absorption at such frequencies. On the other hand, the comparison between the flux density at 2.4 GHz determined by Setia Gunawan et al. (2003; $\sim$1.0 mJy), and the upper limit determined from our GMRT observations at 1.4 GHz (< 0.3 mJy), suggests strong variability at low frequencies, since such difference in flux densities within such small frequency range (1.4-2.4 GHz) is not expected. Furthermore, the emission at 8.4 GHz increases by about $\sim$50% between 2001 and 2005 observations (see Table 3.3). However, shorter variability time-scales in both sources can not be ruled out, since observations do not allow for a precise determination of their variability time scale.

The Thermal/Non-thermal Sources

The sources WR 98 and WR 133, tentatively classified as T/NT, are close binaries with well defined periods of 48.7 and 112.4 days, respectively. Assuming a total mass for the system of $M = 50$ $M_\odot$, the semi-major axis of the orbits would be ~ 1 AU and 1.7 AU, respectively. Non-thermal emission arising from a WCR in these systems must be within the optically-thick region of the WR stellar wind ($\gtrsim 30$ AU at 4.8 GHz; from equation [1.25]) and would not be detectable. This seems difficult to reconcile with the tentative T/NT behavior displayed by WR 98 and WR 133. In fact, the short periods of these systems make it unlikely that the separation between the components (D) increases (even for a high eccentricity), at least to those radii required for non-thermal emission to escape the absorption (~ 30 AU). Pittard et al. (2006) analyzed the thermal emission arising from an adiabatic WCR, and pointed out that thermal emission from the WCR may increase when D decreases (see Figure 1.18), contributing significantly to the total thermal flux, and resulting in a spectrum that may mimic a non-thermal contribution. In this scenario:

- An enhancement of 40% in the flux density (at 4.8 GHz) of the system WR 98 would suggest a decrease of 29% in the separation D (since the thermal emission from the WCR is expected to scale as D^{-1}). However, a WCR within this system would be roughly isothermal with a cooling parameter $\chi \sim 0.1$ (from equation 3.3), contributing with a thermal component with a positive spectral index as we found in Chapter 2. Therefore, the tentative T/NT behavior for WR 98 is likely to be non-thermal emission from the WCR that is able to escape the absorption at certain orbital phases. The upper limit at 1.4 GHz indicates that the non-thermal contribution is strongly affected by the absorption of the unshocked winds at such low frequencies.

- On the other hand, for WR 133 the WCR is likely to be adiabatic ($\chi \gtrsim 1$) with a flat thermal spectrum (Pittard et al. 2006). For WR 133 the presence of a WCR is also supported by the strong emission at X-ray energies (Oskinova 2005) and optical spectroscopic analysis (Underhill & Hill, 1994). However its influence at radio frequencies remains unclear, since the high errors of the spectral indices and the lack of a good time coverage do not allow to infer any variability.

Detailed theoretical models are required in order to determine whether a T/NT spectrum can be reproduced entirely by thermal emission, or whether a non-thermal component of emission can be detected for these systems.

WR 98a and WR 104 are well known colliding-wind binaries with an expanding dust spiral, called 'pinwheel nebulae' which is clearly resolved at IR frequencies (Tuthill et a. 1999, Monnier et al. 1999, Tuthill et al. 2008; see Figure 1.8). Monnier et al. (2002) modeled their radio emission taking into account a thermal plus an absorbed non-thermal component. At 8.4 GHz, we detected WR 98a, but only marginally WR 104. However, we have not detected either of these sources at 4.8 GHz, probably as a consequence of the strong absorption of the non-thermal emission suggested by Monnier et al. (2002). This absorption, and the lack of information about the flux density at higher frequencies in our observations, are likely to be the reason for the high value of the lower limits for their spectral indices.

Finally, although we classified WR 8 and WR 156 as T/NT, we can not completely rule out a single thermal wind origin of the observed emission. The binarity of WR 8 has been questioned by Crowther et al. (1995). Moreover, variability in its emission was only marginally determined from our criteria, and the uncertainty in the determination of its spectral index is high. The same occurs for the flux density and spectral index determinations of WR 156. Further radio observations of both stars are needed to confirm its emission nature.

3.3 Millimeter Observations

The positive radio spectral index of a standard stellar wind emission ($\alpha \sim 0.6$) is expected to extend out at millimeter wavelengths. However, as we have shown for the centimeter range, the millimeter spectrum may also be affected by several processes that could change its α value. The characteristic radius of the emitting region scales with frequency as $R_\nu \propto \nu^{-0.7}$ (Wright & Barlow 1975, Panagia & Felli 1975, see also Section 1.2.1); therefore, at high frequencies (millimeter wavelengths) the emission arises from the innermost part of the wind, and any structure within it is expected to have a high influence over the spectrum (Blomme 2007). Thus, by observing a range of frequencies it is possible to detect changes of structure with distance. Furthermore, our results from the theoretical model presented in Chapter 2 indicate that a radiative WCR in close binary systems could be able to contribute with a thermal component of emission with a spectral index $\gtrsim 1$, which will be detected as an excess of emission at short wavelengths ($\lesssim 1$ cm; see also Pittard 2010). On the other hand, for those sources with hints of non-thermal emission at centimeter wavelengths, the spectrum characterization at millimeter, where only the unshocked stellar winds are expected to contribute, will help to confirm whether a non-thermal contribution is really taking place. In particular, for close binary systems, both the thermal contribution at millimeter wavelengths and the absorption of the non-thermal at centimeter, make the millimeter observations specially important in order to detect any effect of the binarity on the WR spectra.

3.3.1 The Sample

In this section, we analyze observations of nine WR stars at 1.2 mm (250 GHz). The main goal of this analysis is the detection of the influence of a WCR at millimeter wavelengths, suggested by the results presented in Chapter 2. Thus, our sample includes seven close WR binaries, for which their stellar and binary parameters suggest a radiative WCR. For these sources we expected to disentangle any excess of emission at 1.2 mm. We included in the sample the single stars WR 105 and WR 135 as part of a preliminary work aimed to detect the possible difference between the millimeter spectrum of single and close binaries. Four of the sources detected were already observed at centimeter wavelengths.

3.3.2 Observations

3.3.2.1 The 30m telescope

Six of the total nine WR stars of the sample were observed at 1.2 mm with the IRAM 30m telescope (Table 3.3). This antenna is located in Pico Veleta (Sierra Nevada, Sapain) at an

Table 3.5. Wolf Rayet Sample and their Properties

WR	Spectral Type	Binary Status	P (days)	$S_{1.2\,\mathrm{mm}}$ (mJy)
113	WC8d+O8-9IV	SB2	29.7	4.11±1.10
133	WN5+O9I	SB2,VB	112.4	2.62±0.68
135	WC8	single	...	6.66±1.08
139	WN5+O6V	SB	4.2	8.44±0.72
141	WN5+O5V-III	SB2	21.6	8.02±1.08
156	WN8h+OB?	d.e.l.	6.5,10	8.91±0.99

Note. — The values displayed in the columns (1) to (4) were taken from the van der Hucht (2001) WR catalog. SB:Spectral Binary; VB: Visual Binary; a: absorption; d.e.l. diluted emission lines; CWB Colliding Wind Binary.

altitude of 2850 meters. The observations were taken with the bolometer camera MAMBO2 in the on-off mode. The camera operates at 1.2 mm wavelength with a HPBW (Half Power Beam-Width) of 11", a pixel spacing of 20", and a sensitivity of 1.5 mJy (this is the rms after 10 minutes of integration time with normal conditions and sky-noise removal).

Calibration

The Six WR stars were observed during the pool observing session in October/November of 2010. Data calibration was carried out with the MOPSIC package, using the pipeline provided by the IRAM support team. Pointing and focus sources were observed every ~ 2 hours. We reached a rms$\sim 1\,\mathrm{mJy\,beam^{-1}}$ and $\sim 0.7\,\mathrm{mJy\,beam^{-1}}$ with 20 and 60 minutes of integration, respectively. The forward efficiency (Feff) was found to be not stable during the whole pool observing session. We tested the stability of our observations by calibrating the sub-scan separately for those sources for which more than one scan were taken. In fact, we did not detect any major effect on our rms noise values. In Table 3.5 we present the observed WR stars and the flux density measurements.

3.3.3 Millimeter Spectra of WR stars

In this section we analyze the spectrum at millimeter wavelengths for nine WR stars and compare it with the centimeter spectra obtained from our previous observations. We present in Table 3.6 the flux densities (centimeter and millimeter) used for such analysis. For the stars in Table 3.5, flux densities at 1.2 mm were determined from our observations. For WR 98, 105, and 138, millimeter flux densities were taken from Althenhoff et al. (1994).

The centimeter spectra of seven of the stars in the millimeter sample (WR 98, 105, 113, 133, 138, 141, and 156) were previously characterized and discussed in Section 3.2. For these stars, we determined the expected flux densities at 1.2 mm, $S_{\mathrm{cm-1.2\,mm}}$, by extrapolating the centimeter spectrum. In the case of sources for which variability at their centimeter spectra was found, we characterized the centimeter spectrum using only the flux densities at the epoch when the spectrum was classified as thermal from the shorter wavelengths (this is considered as a minimum contribution of the WCR, see Section 1.3.2). For WR 135 and WR 139, for which only 6 cm observations were available, we determined the expected flux density at millimeter wavelengths

by extrapolating a standard wind spectrum with a spectral index $\alpha = 0.6$. Extrapolated and measured flux densities at 1.2 mm are both presented in Table 3.6.

For those sources detected at several centimeter wavelengths, we determined two spectral indices in order to characterize both the centimeter and millimeter wavelength ranges. The spectral index at centimeter wavelengths, $\alpha_{\rm cm}$, was determined from the flux densities used for the extrapolation described above. On the other hand, centimeter-millimeter spectral indices, $\alpha_{\rm cm-mm}$, were determined using the flux density at 1.2 mm and that at the shorter wavelength of the centimeter observations considered. For WR 135 and WR 139, we could determine only one spectral index considering the flux densities at 1.2 mm and 6 cm. Notice that we are not taking into account the possible spectral changes associated with time variability, since the flux densities at centimeter and millimeter wavelengths were taken in different days. In Figure 3.5 we plot the extrapolation of the centimeter spectrum to millimeter wavelengths, and the centimeter-millimeter spectra inferred from the flux densities at 1.2 mm. We present in Table 3.6 the centimeter flux densities used for the extrapolation, the values compared at 1.2 mm, and the spectral indices derived for each wavelength range.

Table 3.6. Comparison between cm and mm Observations.

WR	$S_{6\,\mathrm{cm}}$ (mJy)	$S_{3.6\,\mathrm{cm}}$ (mJy)	$S_{2\,\mathrm{cm}}$ (mJy)	$S_{1.3\,\mathrm{cm}}$ (mJy)	$S_{1.2\,\mathrm{mm}}$ (mJy)	$S_{\mathrm{cm}-1.2\,\mathrm{mm}}$	α_{cm}	$\alpha_{\mathrm{cm}-\mathrm{mm}}$	Obs Date	Ref.
98	0.58±0.06	1.18±0.05	...	1.94±0.15		9.93±2.37	0.64±0.07		07May06	MP09
	...	...	...	...	19±5			0.95±0.26	87Dec	AT94
105	2.73±0.07	...	7.02±0.37	...		72.30±13.77	0.83±0.05		99Nov27	MP09
	...	...	...	...	48±5			0.68±0.1	87Dec	AT94
113	0.22±0.03	0.47±0.04	...	1.27±0.07		15.89±3.31	1.06±0.09		07May06	MP09
	...	...	...	...	4.11±1.10			0.49±0.26	10Oct28	TS
133	<0.41	0.31±0.03	...	0.57±0.07		2.53±1.23	0.60±0.15		07May06	MP09
	...	...	...	...	2.62±0.68			0.63±0.27	10Oct27	TS
135	0.6±0.09	...	...	...		6.27				HO82
	...	...	...	...	6.66±1.08			0.62±0.13	10Oct27	TS
138	<0.12	0.52±0.03	...	1.15±0.08		7.54±2.01	0.79±0.09		07May06	MP09
	...	...	...	...	12±4			0.98±0.33	87Dec	AT94
139	0.28±0.03	...	...	...		2.93				BA82
	...	...	...	...	8.44±0.72			0.87±0.18	10Oct27	TS
141	0.59±0.04	1.28±0.04	...	2.86±0.15		27.72±4.43	0.91±0.05		08Mar05	MP09
	...	...	...	...	8.02±1.08			0.43±0.14	10Oct27	TS
156	0.77±0.04	0.99±0.04	...	1.59±0.09		4.57±0.73	0.46±0.05		08Mar05	MP09
	...	...	...	...	8.91±0.99			0.73±0.12	10Oct27	TS

Note. — Flux densities at wavelength $\geq$ 1.3 cm were used for the α_{cm} determinations. For $\alpha_{\mathrm{cm}-\mathrm{mm}}$ we considered only $S_{1.2\,\mathrm{GHz}}$ and the flux density at the closer short wavelength available.

References. — TS:This Study; BA82: Bieging et al. (1982); HO82: Hogg (1982); AT94: Altenhoff et al. (1994); MP09: Montes et al. (2009).

We consider that there is an excess or deficit in the flux density at 1.2 mm when the measured and interpolated values do not agree within their error bars. The difference between these two values implies a change in the spectrum behavior from the centimeter to the millimeter wavelength ranges. This change in the spectrum is also shown by the difference between $\alpha_{\rm cm}$ and $\alpha_{\rm cm-mm}$, although, the lack of observations at intermediate wavelengths does not allow to properly sample the change in the spectral index. From our analysis we classify the stars in three groups:

- Stars for which no significant difference between the measured and the interpolated flux densities was found, suggesting a *standard wind spectrum*.
- Stars for which the millimeter flux density indicates an excess of emission, with respect to the value obtained from the extrapolation of the centimeter spectrum. For these sources their $\alpha_{\rm cm-mm}$ values also suggest an increase of the spectral index towards millimeter wavelengths.
- Stars for which the millimeter flux density indicates a deficit of emission with respect to the value obtained from the extrapolation of the centimeter spectrum. These sources present a *steep centimeter spectra* ($\alpha_{cm} > 0.6$), while the millimeter spectral index is in agreement with a standard wind spectrum.

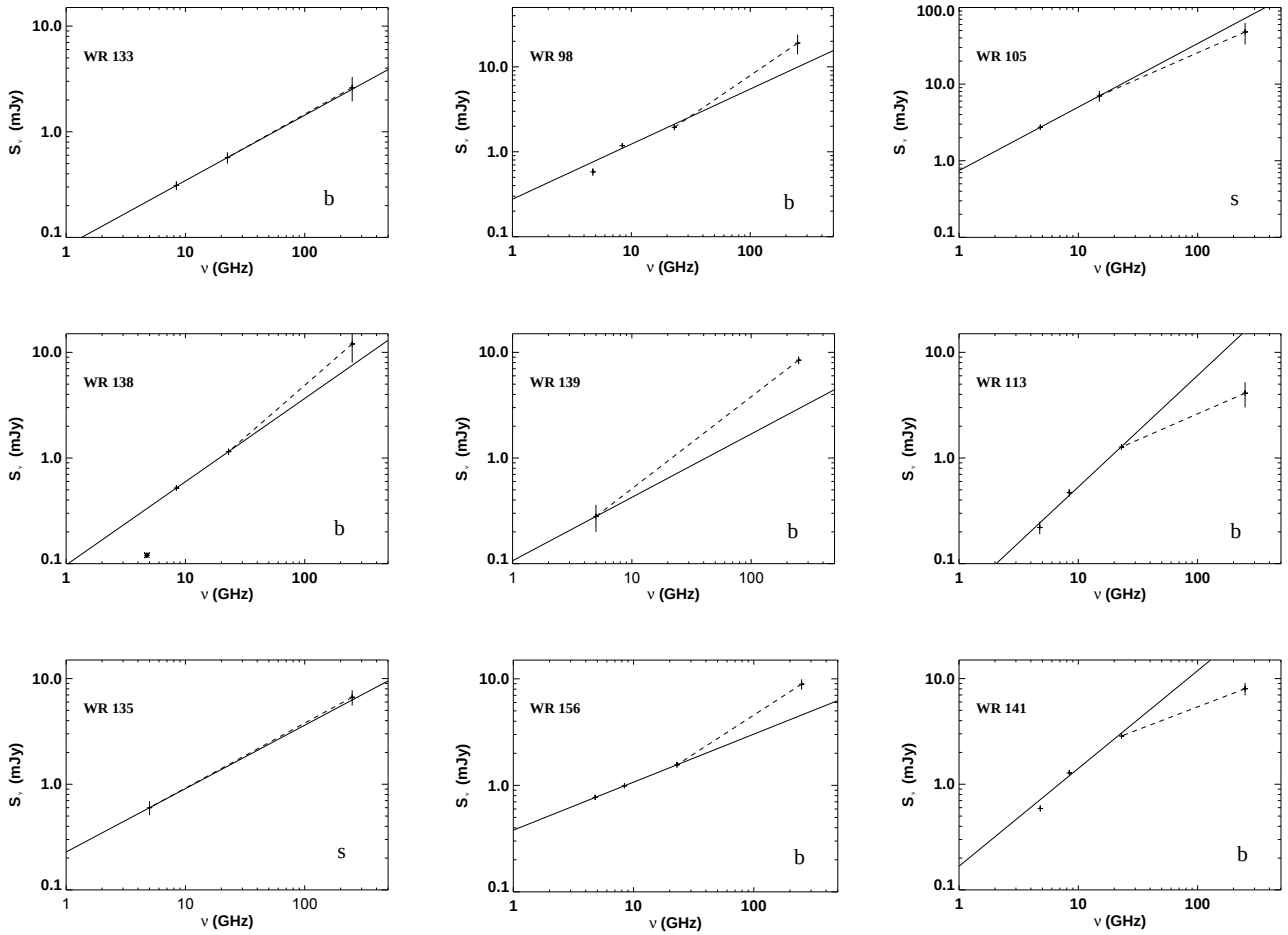

Figure 3.5 Extrapolation of the centimeter spectrum to millimeter wavelengths (solid line) and comparison with the millimeter spectrum (dashed line). The comparison between the extrapolation and the flux densities obtained from millimeter observations results in three groups: Stars for which the whole spectrum seems to be in agreement with a standard wind spectrum (left column), stars with an increase in the spectral index toward millimeter wavelengths, interpreted as a hint of an excess of emission at millimeter (middle column), and, finally, sources with a steep centimeter spectrum that turns into a standard wind spectrum at millimeter (right column). 'b' and 's' labels indicate the binary and single status of the star, respectively.

3.3.4 Discussion

As we previously commented, deviations in the standard wind parameters may result in a change of its thermal spectrum, with $\alpha \neq 0.6$. On the other hand, the presence of a companion may also impact the spectrum through the contribution of an extra component of emission. Thus, for a non-standard wind spectrum, it is difficult to disentangle the different processes that could be affecting it. In this section, we will discuss the processes that are likely to be taking place in the three different kinds of spectra we discussed in the previous subsection. In particular, for the binary stars of our sample (WR 98, 113, 133, 138, 139, 141, and 156), we will ascertain the relationship between their binarity and their spectra.

Standard Stellar Wind Spectrum

For WR 133, the thermal spectrum inferred from our millimeter observations are in agreement with that suggested from the centimeter observations, with no significant difference between, $S_{1.2\,\mathrm{mm}}$ and $S_{\mathrm{cm}-1.2\,\mathrm{mm}}$. In Section 3.2 we have presented archival data from which this source showed a tentative non-thermal spectrum (see Table 3.3), suggesting the presence of an extra component of emission at centimeter wavelengths, presumably from a WCR. The WCR within this system is expected to be adiabatic (with a cooling parameter $\chi \gtrsim 1$) with a thermal contribution with a spectral index ~ -0.1. Thus, any contribution from it would be mainly relevant at centimeter wavelengths, without any significant impact over the millimeter range, which is consistent with the results obtained from our observations.

WR 135 is a single star for which its radio spectrum has not been previously characterized. Our results suggest a standard stellar wind spectrum; however, intermediate wavelength observations, between 6 cm and 1.2 mm, are required in order to rule out any change in the spectrum.

Finally, for WR 138 we did not detect a significant change in the spectrum from the centimeter to the millimeter wavelength range. Slightly high values of the spectral indices, but still consistent with the standard value of 0.6, were found for this source. However, it is remarkable the low value of the upper limit at 4.8 GHz, which resulted in a high value of the lower limit for the centimeter spectral index derived in Section 3.2 (see Table 3.3).

Steep Millimeter Spectrum ($\alpha > 0.6$)

The steep tendency of the spectrum of a single stellar wind toward short wavelengths has been previously interpreted as the result of the presence of clumps and/or changes in the ionization state (Leitherer & Roberts 1991, Nugis et al. 1998). Furthermore, in close systems, the steep spectrum of a radiative WCR contribution could dominate the spectrum, changing the spectral index of the stellar wind at centimeter wavelengths to a steeper value at shorter wavelengths (Chapter 2, Pittard 2010).

WR 98 shows flux density variability at 6 cm, changing the spectral index from ∼0.26 to ∼0.64 within a period of time of ∼15 days (see Table 3.3). For the comparison with the millimeter spectrum, we considered only the spectral index in its "thermal state" ($\alpha_{\mathrm{cm}} \sim 0.64$). In Figure 3.5 a clear steepening of the spectrum toward short wavelengths can be seen. From the millimeter

observations we found a flux density $S_{1.2\,\mathrm{mm}} \sim 19$ mJy, which is a factor of two higher than that obtained from the extrapolation of the centimeter spectrum, $S_{\mathrm{cm}-1.2\,\mathrm{mm}} \sim 10$ mJy. Furthermore, although marginally, an increase in the spectral index towards millimeter wavelengths can be seen (for the comparison between $\alpha_{\mathrm{cm}-\mathrm{mm}}$ and α_{cm}; see Table 3.6). Such behavior can result from a thermal contribution from a radiative WCR. In Section 2.6 we successfully fitted the spectrum of WR 98 by including the thermal contribution from a radiative WCR. This is supported by the value of $\chi < 1$ derived from its physical parameters. The short time scale variability of $S_{6\,\mathrm{cm}}$ was previously interpreted as indicative of a non-thermal contribution from a WCR that changes due to the orbital motion of the stars (see Section 3.2.4). Thus, if a thermal WCR contribution is responsible for the steep spectrum at millimeter wavelengths, it is likely that the resulting spectrum at these wavelengths will be also variable.

For WR 139 we found a flux density, $S_{1.2\,\mathrm{mm}} \sim 8.5$ mJy that suggests an excess of emission, with respect to that estimated (~ 3 mJy) by the extrapolation of the $S_{6\,\mathrm{cm}}$. It is likely that this excess of emission is due to a thermal contribution from a radiative WCR. However, the best way to confirm the WCR contribution is through flux density variability studies, mainly at 1.2 mm, looking for a possible correlation between such variability and the orbital period.

For WR 156, although a difference between $S_{1.2\,\mathrm{mm}}$ and $S_{\mathrm{cm}-1.2\,\mathrm{mm}}$ was inferred, the whole spectrum could be adjusted with a standard wind spectrum ($\alpha \sim$0.58). From the spectral index determinations, we found that the millimeter spectrum is slightly steeper ($\alpha_{\mathrm{cm}-\mathrm{mm}} = 0.73 \pm 0.12$), yet consistent with a standard wind spectrum. However, the T/NT centimeter spectrum ($\alpha_{\mathrm{cm}-\mathrm{mm}} \sim 0.46$; see Section 3.2.3.2) suggests a WCR contribution. Such contribution could be either non-thermal, or optically thin thermal emission if the WCR remains adiabatic. Thus, for this source, although our criteria suggest an excess of emission at millimeter wavelengths, it is likely that a WCR is mainly affecting the centimeter range, unlike the case of WR 98 and WR 139.

Steep Centimeter Spectrum

For WR 105, 113, and 141, we found the centimeter spectrum to be steeper than the one derived from the 1.2 mm observations. Such spectrum is reflected as a deficit in the flux density at millimeter wavelengths with respect to that one extrapolated from the centimeter spectrum.

A similar behavior has been interpreted as the sum of a thermal component from the stellar wind, and a non-thermal component from the WCR diminished by free-free absorption in the unshocked wind (e.g. Chapman et al. 1999, see left panel in Figure 3.6). Thus, the resulting spectrum can be modeled as,

$$S_{\nu,\mathrm{obs}} = S_{\nu_0,th}\left(\frac{\nu}{\nu_0}\right)^{\alpha_{th}} + S_{\nu_0,nth}\left(\frac{\nu}{\nu_0}\right)^{\alpha_{nth}} e^{-\tau_\nu}, \tag{3.4}$$

where $S_{\nu_0,th}$ and $S_{\nu_0,nth}$ are the flux densities at the frequency ν_0 of the thermal and the non-thermal components, with the spectral indices α_{th} and α_{nth}, respectively, and $\tau_\nu \approx \tau_{\nu_0}(\nu/\nu_0)^{-2.1}$ is the optical depth. On the other hand, Pittard et al. (2006) have found recently, that in close systems, where the optically thin thermal emission from the WCR becomes comparable to the thermal emission from the unshocked winds, a similar spectrum can also result entirely

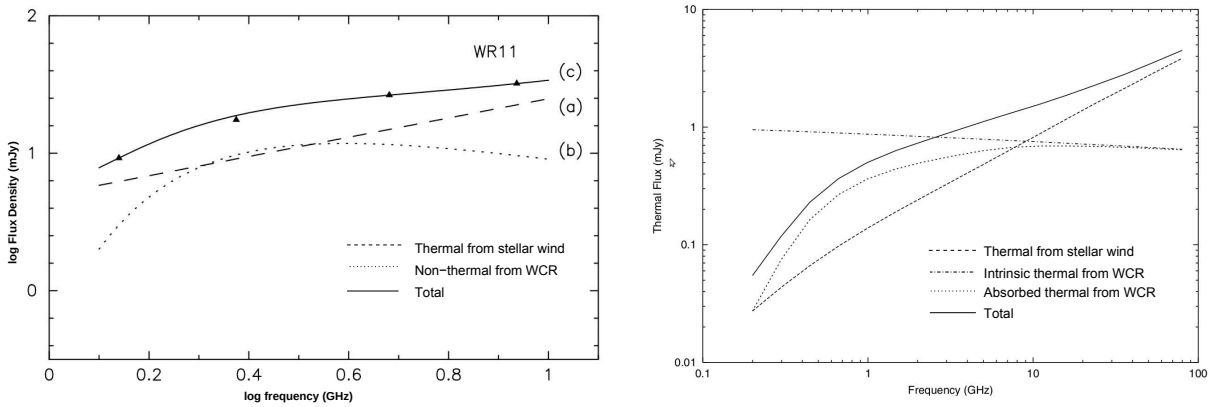

Figure 3.6 In the left panel, the model for the radio spectrum (solid line) of γ^2 Vel (WR 11) composed by a thermal stellar wind component (dashed line) and a non-thermal contribution (dotted line) diminished by the absorption in the winds (Chapman et al. 1999). The right panel presents the plot of the thermal spectrum (solid line) from a system with an adiabatic WCR with an optically thin thermal emission contribution. The thermal emission from the stellar winds (dashed line), the intrinsic emission from the WCR (dot-dashed line), and that resulting after having been diminished by the absorption (dotted line) are plotted (Pittard et al. 2006).

from thermal processes, which could be erroneously interpreted as evidence of non-thermal emission (see Figure 3.6). Therefore, an estimation of the possible contribution from each kind of emission (non-thermal or optically-thin thermal) is required in order to discern between these two possibilities.

WR 105 shows a variable spectral index at centimeter, which changes from negative values to those higher than 0.6 (see Table 3.3). On the other hand, the millimeter spectrum derived is quite similar to that of a standard wind. It is likely that the steep $\alpha_{\rm cm} \sim 0.83$ (see Table 3.6) is actually resulting from the non-thermal emission component being diminished by the absorption in the winds, resulting in this way in the observed excess of emission at centimeter wavelengths. Although it is difficult to unambiguously disentangle a non-thermal component from an optically thin thermal one by only the spectral index value, the negative spectral indices determined for one of the observing epochs supports the non-thermal nature of such component (such negative value of ~ -0.3 is not expected for optically-thin thermal emission). However, as we pointed out in previous sections, the binarity of this system has not been yet proved, which makes difficult to assure a WCR as the origin of the non-thermal emission.

WR 113 and WR 141 were previously classified as thermal sources because of their positive spectral indices at centimeter wavelengths (see Section 3.2.3.2). However, the millimeter observations indicate an excess of emission at centimeter wavelengths, probably from a WCR emission component. We fit the equation (3.4) to the flux densities at 4.8, 8.4, 23, and 250 GHz of WR 113 and WR 141. We assume a spectral index for the thermal component of $\alpha_{th} = 0.6$ (a standard stellar wind), and $\alpha_{nth} = -0.5$ for the non-thermal (Eichler & Usov 1993 see also 1.4.1). We set $\nu_0 = 8.4$ GHz and fitted the data, solving for the free parameters $S_{\nu_0,th}$, $S_{\nu_0,nth}$, and τ_{ν_0}. For WR 113 we find $S_{\nu_0,th} = 0.4$ mJy, $S_{\nu_0,nth} = 5.1$ mJy, and $\tau_{\nu_0} = 15.0$. For WR 141 the solution is $S_{\nu_0,th} = 1.0$ mJy, $S_{\nu_0,nth} = 2.2$ mJy, and $\tau_{\nu_0} = 2.1$. In Figure 3.7 we plot the result for the models of these two stars. Although the thermal emission is the dominant contribution to the total radio emission from both WR systems at essentially all frequencies,

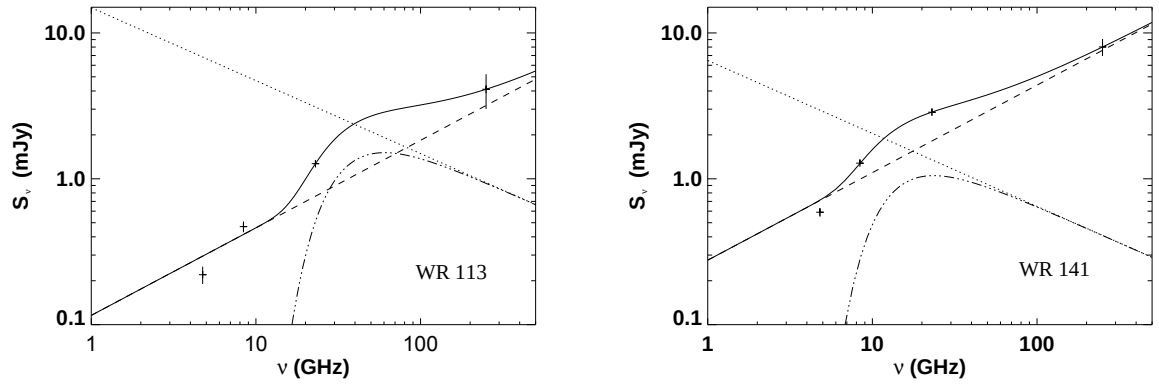

Figure 3.7 Fits to the flux densities at 4.8, 8.4, 23, and 250 GHz ('+'; vertical lines represent the uncertainties) of WR 113 (left) and WR 141 (right). In both panels the total emission was modeled by assuming a thermal component plus a non-thermal one diminished by the absorption in the winds (solid line). The thermal (dashed line), the intrinsic non-thermal (dotted line), and the non-thermal emission diminished by the absorption (dot-dash line) are plotted. See text for details of the fits.

the effect of the non-thermal contribution is noticeable at intermediate frequencies (10 to 100 GHz), considerably modifying the resulting spectrum in those regions of the spectrum.

We found that a similar fit can also result from the assumption of an optically thin thermal emission component from an adiabatic WCR with $\alpha_{nth} \sim -0.1$. However, both systems are roughly radiative with cooling parameters $\chi < 1$. Therefore, optically thin thermal emission is unlikely to be taking place in these systems. It is important to note that the value of χ plays an important role in the classification of the nature of a system.

On the other hand, Eichler & Usov (1993) estimated that in order the non-thermal emission to escape the absorption at a frequency ν in a WR system, the orbital period must be greater than a critical value given by

$$\left[\frac{P_{cr}}{\mathrm{days}}\right] \simeq 26\left(1-\frac{\beta^{2/5}}{4}\right)^{-1}\beta^{-1/3}\left[\frac{\dot{M}}{10^{-5}\mathrm{M}_\odot\,\mathrm{yr}^{-1}}\right]^{2/3}\left[\frac{v_\infty}{10^3\mathrm{km\,s}^{-1}}\right]^{-5/3}\left[\frac{T}{10^4\mathrm{K}}\right]^{-1/2}\left[\frac{\nu}{5\mathrm{GHz}}\right]^{-2/3} \quad (3.5)$$

where $\beta = (\dot{M}_{WR}\, v_{WR})/(\dot{M}_O\, v_O)$ is the wind momentum ratio, and $\dot{M}$, v_∞, and T, are the mass loss rate, terminal velocity, and temperature of the WR wind, respectively (see Section 1.4.1 for details). From Figure 3.7 it can be seen that the higher contribution of the WCR at our observing frequencies occurs at 23 GHz.

Thus, in order to investigate if non-thermal emission is likely to escape the absorption at least at this frequency, we estimated P_{cr} at ν =23 GHz. We assumed the WR wind parameters, $\dot{M}$ and v presented in Table 3.4, and a value of $\beta = 0.1$ (typical value in WR systems) for both systems. For WR 113, P_{crit} is $\sim$ 17 days, which is less than the orbital period, P $\sim$29.7 days. Therefore it is likely that the non-thermal emission can be detectable at 23 GHz, which supports the model presented in Figure 3.7. For WR 141, P_{crit} is $\sim$ 20 days, which is similar to its orbital period P $\sim$21.6 days. Simultaneous multi-wavelength observations, covering both the millimeter and the centimeter ranges, would allow us to confirm whether a two component model applies here or not.

3.4 Comments on Individual Sources

WR 8. This WR star was identified as a spectroscopic binary by Niemela (1991). However they found that several periods (P=38.4 to 64 days) were able to fit their radial velocity study. Crowther et al. (1995) confirmed their combined spectral type (WN7/WCE) and questioned its binarity. At radio frequencies, this star was first detected by Cappa et al. 2004 at 8.4 GHz. We have detected it at 4.8, 8.4, and 23 GHz. Its spectral index ($\alpha = 0.17 \pm 0.15$) suggests a T/NT spectrum; however, due to its high uncertainty we cannot completely discard a thermal nature for its emission, and more observations are required in order to confirm a non-thermal contribution.

WR 79a. This luminous star was initially classified as O8 Iafpe (Mason et al. 1998) and subsequently as WN9ha (Bohannan & Cowther 1999). It is considered as a massive star, probably in the boundary between O and WR type (Millour et al. 2008). Bieging et al. (1989) observed it for the first time at radio frequencies, and classified it as a thermal source with $\alpha \simeq 0.8$. Later observations by Setia Gunawan (2003) showed evidence of non-thermal emission ($\alpha \sim -0.1$). The upper limit, $S_{1.4\ \mathrm{GHz}} \lesssim 0.3$, suggests that any non-thermal contribution is being severely affected by the absorption at 1.4 GHz. Although this source is known as a visual binary (O8 Iafpe+F4p; Mason et al. 1998), it is unlikely that the non-thermal emission arises from a WCR between these components, since the separation between the stars is too large (6.″9; Mason et al. 1998). If the non-thermal emission is actually a diagnostic for binarity (Williams & Dougherty, 2000; Van Loo et al. 2006), it is likely that the WR star itself is a binary; however there is no spectroscopic evidence for this (Marchenko et al. 1998b). Prinja et al. (2001) reported variability in the inner regions of the wind on time-scales of days. They also discussed its variability in a context of co-rotating interaction regions (CIR; see Cranmer & Owocki 1996 and Prinja et al. 2001); however, it is not clear whether these perturbations could affect the radio emission, which is produced in the more external regions of the wind.

WR 89. This star (WN8h+OB) was classified as a visual binary by van der Hucht (2001). Its radio emission was first detected by Abbott et al. (1986), who characterized it as a thermal source. Later observations revealed flux density variability but always with a positive α (Table 3.3). We report an enhancement of its flux density, especially at 8.4 GHz, which produces a change in α, but still being consistent with thermal emission.

WR 98. This star was found to be a close binary (WN7o/WC+O8-9) with P=48.7 day (Gamen & Niemela, 2002). Abbott et al. (1986) classified it as a non-thermal radio source. We present two sets of radio observations at centimeter wavelengths, separated by ∼15 days. Although the 8.4 GHz flux density was similar at both epochs, an increase in the emission at 4.8 GHz was observed between the two epochs, which caused the spectral index to change from negative to positive (see Table 3.3). Furthermore, the upper limit derived from our GMRT observations at 1.4 GHz suggests that a non-thermal component would be severely affected by the absorption of the winds at this frequency. The observed variability supports a WCR as the origin of the non-thermal emission. On the other hand, the flux density at 250 GHz suggests an excess of emission at high frequencies. The parameters of this system indicate that a radiative WCR could be able to contribute with an optically thick thermal emission with a spectral index

~ 1, resulting in the excess of emission suggested by our high frequency observations. The flux at 250 GHz was consistent with the contribution of a radiative WCR contribution calculated from our model in Section 2.6. Thus, our observations indicate that the WCR is likely to be affecting the whole spectrum, with a non-thermal component at low frequencies and a thermal one at high frequencies. Detailed observations covering the whole orbit are required in order to confirm the periodic behavior in the changing spectrum, and hence the detection of the WCR.

WR 98a. This binary star (WC8-9vd+?) is a well known infrared source, presenting an expanding dust spiral, a "pinwheel" nebulae, with P=565 days (Monnier et al. 1999). These spiral structures are thought to be the result of denser regions coming from the interaction between the winds of a CWB with a WC type star component. At radio, it was first studied by Monnier et al. (2002). The spectral index determined from their observations is slightly flat ($\alpha \sim 0.3$) and the authors report the detection of a non-thermal contribution. We detected this source just at one frequency; hence, we present only a lower limit for α. Therefore, we cannot draw any firm conclusion on the nature of its emission only from our observations.

WR 104. This binary star (WC9d+B0.5 V) is the infrared pinwheel nebulae prototype. It was described by Tuthill et al. 1999 with a period P=241 days. It was included in the multi-frequency radio study presented by Monnier et al. (2002). As well as WR 98a, its flat spectral index ($\alpha \sim 0.1$) suggests a non-thermal contribution. Cappa et al. (2004) reported variability in the 8.4 GHz flux density. From our observations, we report only a marginal detection of $\sim 4\sigma$ at 8.4 GHz, which suggests a decrease in the emission with respect to the Cappa et al. (2004) observations, confirming the variability. Without any detection at 4.8 GHz, we only report a tentative lower limit for the spectral index.

WR 105. This star was reported as a non-thermal variable radio source by Abbott et al. (1986) and Leitherer et al (1997). We present two sets of observations separated by one year, and another two sets from the VLA archive performed in 1999. We confirm the variability in the flux density and in the spectral index, and hence the presence of a non-thermal contribution. The change of α, from negative to positive, resembles that observed for several CWB. We also notice an anti-correlation in time, between the flux densities at 8.4 GHz and at 4.8 GHz (see Table 3.3 and Figure 3.8). This source was one of the non-thermal emitters in the Williams & Dougherty (2000) study without any confirmation of binarity. The high values of the spectral indices at the thermal state are not in agreement with a single stellar wind spectrum; instead, they are likely to be the result from a maximum value for the absorption of the non-thermal component at low frequencies. In contrast, the flux density at 250 GHz reveals a standard stellar wind spectrum towards such high frequencies, which supports a non-thermal contribution at centimeter wavelengths. However, because of the observed variability for this source, simultaneous multifrequency observations, covering from low to high frequencies (from 1 to 250 GHz), are required in order to properly characterize the spectrum shape. As well as for WR 79a, its non-thermal nature could be an indication of the binarity of WR 105.

WR 113. The orbit of this spectroscopic binary (WC8+O8-9) was fitted by Niemela et al. (1999), who obtained a period of P=29.7 days. Cappa et al. (2004) presented the first detection at radio wavelengths (8.4 GHz). We detected it at the three observing frequencies (including for the first time observations at 4.8 and 23 GHz) and report a positive steep spectral index.

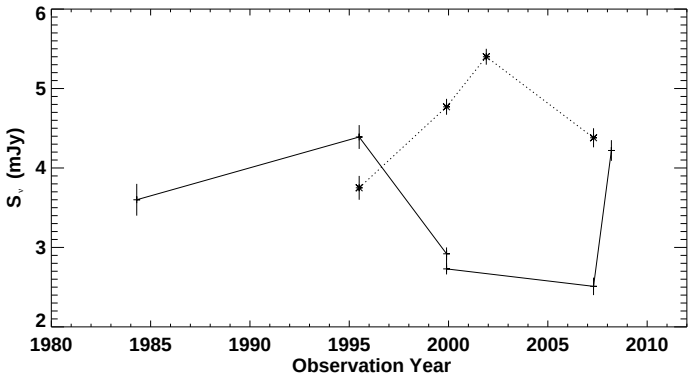

Figure 3.8 WR105 flux densities at 4.8 GHz ('+') and 8.4 GHz ('∗'); vertical lengths represent the uncertainties) as function of the observation date. This figure suggests an anti-correlation between flux densities at 4.8 GHz and 8.4 GHz (see also Table 3.3).

Such positive spectral index could be interpreted as indicative of thermal emission. However, the change of the spectrum from a steep to a standard wind value of 0.6 towards millimeter wavelengths, suggests an excess of emission at the centimeter wavelengths, presumably coming from a non-thermal component from a WCR (Figure 3.7). In this way, the spectrum of this source suggests that in close systems the non-thermal emission could also impact the spectrum, even in the case that a negative spectrum is not detected. Simultaneous multi-wavelength observations, including the frequencies between 23 GHz and 250 GHz, are required in order to improve the fit and the model of the whole spectrum.

WR 133. This star is a close binary system (WN5+O9I) with P=112.4 days (Underhill & Hill, 1994). It was not detected at 4.8 GHz by Abbott et al (1986). Cappa et al. (2004) detected it at 8.4 GHz, but did not provide any information about its spectral index. We observed it at 4.8, 8.4 and 23 GHz with the VLA with no detection at 4.8 GHz. From the flux densities at 8.4 and 23 GHz we found a positive spectral index that suggests a thermal nature. We also observed this source at 250 GHz, corroborating the standard wind spectrum suggested from the VLA observations. We also analyzed archive VLA data at 1.4, 4.8 and 8.4 GHz finding a tentative $\alpha < 0$ and a first detection at 4.8 GHz. This flux density and spectral index variability, together with the strong emission at X-ray energies (Oskinova 2005) could be indicative of the presence of a WCR between the WR and its closer companion. This was also suggested by Underhill & Hill (1994) from an absorption line detected in their spectroscopic analysis. In our first observing epoch (May 2007), we also detected the northern non-thermal source reported by Cappa et al. (2004). However it is undetected in the archive data analyzed (taken in May 1993). In Figure 3.9 we present a comparison between our observations and the archival data.

WR 135. This star has been only detected at 4.8 GHz by Hogg (1982), without any previous information about its radio spectrum. Our observations at 250 GHz indicate a thermal spectrum consistent with a standard stellar wind. Intermediate frequency observations are required in order to trace the spectrum with great detail.

WR 138. This spectroscopic binary with a period of P=1538 days (Annuk 1991) was first detected by Bieging et al. (1982) at 4.8 GHz with $S_{4.8\,\mathrm{GHz}} \approx 0.6\,\mathrm{mJy}$. We have detected it

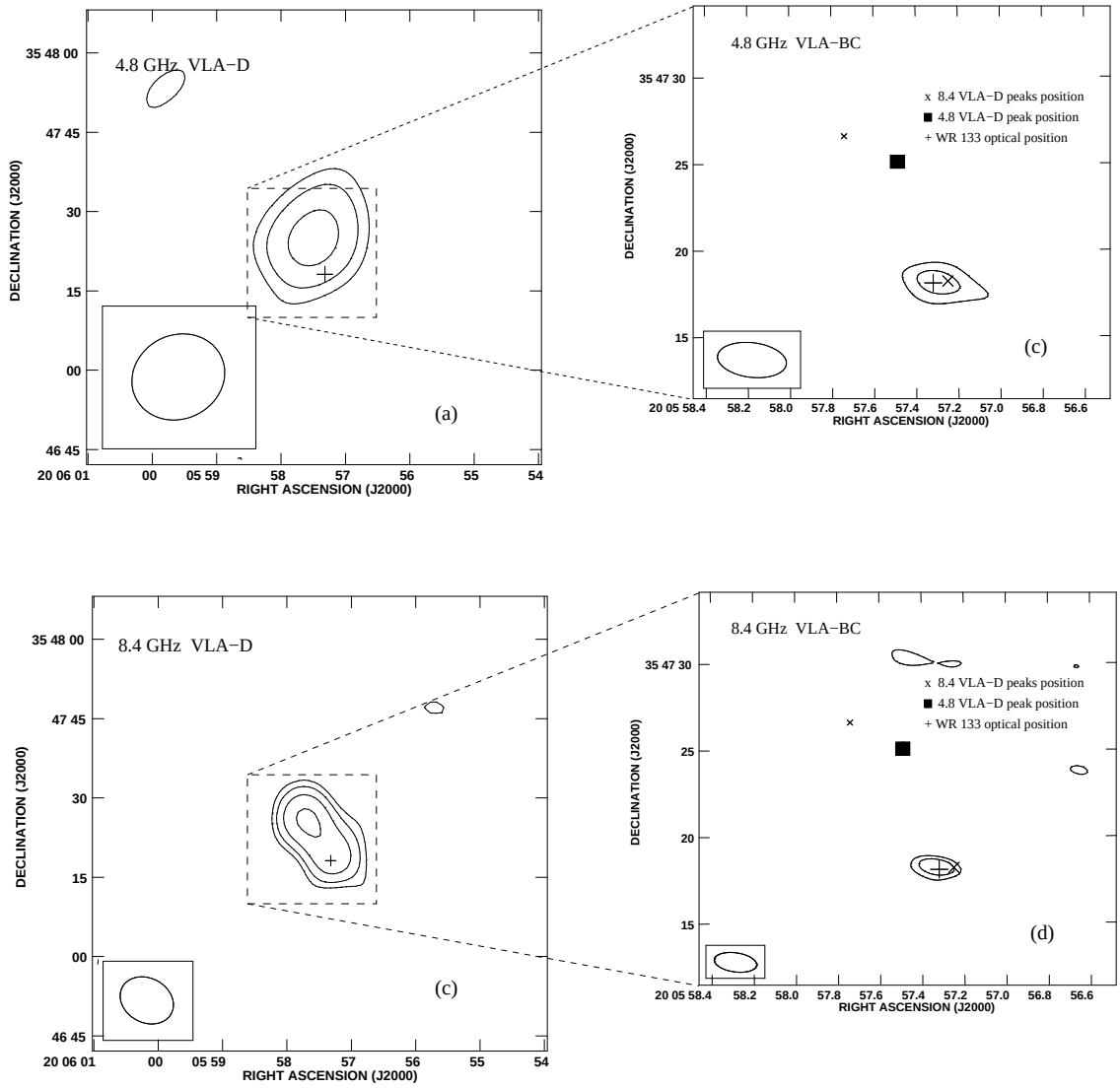

Figure 3.9 Contour images of WR 133. (a) and (b) are 4.8 GHz images and (c) and (d) at 8.4 GHz. The images in the left were both done with VLA-D observations and those in the right with VLA-BC. The plus sign marks the optical position of WR 133. The cross in (c) and (d) are the positions of the radio source associated with WR 133 and the north non-thermal source at 8.4 Hz. The square is the position of the northern source at 4.8 Hz presented in (a). We ruled out the source detected at 4.8 GHz with VLA-D to be WR 133, since the position of this source is closer to the northern source observed at 8.4 GHz.

at 8.4 and 23 GHz. However, at 4.8 GHz we only derived an upper limit for its flux density ($S_{4.8\,\mathrm{GHz}} < 0.12\,\mathrm{mJy}$) which suggests variability at this frequency. Besides this, the upper limit to the flux density at 4.8 GHz, results in a high value for the lower limit of spectral index between 4.8-8.4 GHz ($\sim$2.67). As for WR 79a, WR 98a, and WR 104, the variability and the high value of the lower limit of the spectral index at the lower observed frequencies, could be an indication of an emission component from a WCR. On the other hand, this source shows spectroscopic indications of a close compact companion with a short period ($P \sim$ days; Lamontagne et al. 1982 and Moffat & Shara, 1986). If this source is actually a close binary, it is possible that the steep spectrum at low frequencies results from a non-thermal contribution partially absorbed

by the stellar wind, with a spectrum similar to that modeled for WR 113 and WR 141 (Figure 3.7). On the other hand, the flux density at 250 GHz suggests a slightly steep spectrum, but still consistent with a single stellar wind.

WR 139. This binary, better know as V444 Cyg (WN5+O6), was detected at 6 cm by Bieging et al. (1982) with a flux density, $S_{6\,\mathrm{cm}} = 0.28 \pm 0.08$ mJy, a higher value than that estimated (0.05 mJy) by assuming a smooth wind with $\dot{M} = 0.6 \times 10^{-5}\,\mathrm{M_\odot\ yr^{-1}}$ (e.g. Kurosawa et al. 2002). Furthermore, this source shows variable X-ray emission, which is thought to result from the shocked material within the WCR (Corcoran et al. 1996, Bhatt et al. 2010). Our observations at 1.2 mm suggest an excess of emission by a factor of ~ 3, with respect to that estimated (~ 3 mJy) from the extrapolation of the $S_{6\,\mathrm{cm}}$ (assuming a stellar wind spectrum with $\alpha = 0.6$). However, the best way to corroborate such origin for the steep spectrum, is through the correlation between the variability and the orbital period. Thus, multifrequency observations, along a complete orbital period are required for this source.

WR 141. Marchenko et al. (1998) analyzed this spectroscopic binary (WN5+O5V-III), fixing a period of P=21.6 days. It was first detected at radio frequencies (4.8 GHz) by Beiging et al. (1982). We detected it at all the observing frequencies, with no significant variability at 4.8 GHz (the only previous detection). Marchenko et al. (1998) noticed a periodic behavior in an extra emission component present in some emission lines of the WR stellar wind. Although these authors could not distinguish the origin of this emission, they pointed out that this behavior could be originated by a WCR, frequently detected in WR+O binaries (Moffat et al. 1996). The X-ray emission detected by Oskinova (2005) also supports this scenario, since it is expected that the WCR should have a contribution to the thermal emission detected at these energies (Stevens et al. 1992). The 250 GHz observations suggest a spectrum similar to that described for WR 113, with a thermal plus a potentially absorbed non-thermal significant contribution at frequencies between 8.4 and 23 GHz (Figure 3.7).

WR 156. This WN8h star was classified as a binary in the WR catalog (van der Huch, 2001), but a conclusive periodicity has not been determined. Moreover, Hamann et al. (2006) concluded that this star is likely a single one. We detected it at 4.8, 8.4, and 23 GHz with $\alpha \simeq 0.46$ which is classified as a T/NT spectrum. The high frequency observations describes a slightly steep spectrum, but still consistent with a stellar wind spectrum. Thus, any influence of binarity is likely to be taking place at the low frequency range (centimeter wavelengths). Moreover, the whole spectrum of this source is also consistent with a thermal standard wind spectrum.

3.5 Alternative Scenarios

In this chapter we have discussed the characteristics of the spectrum for the sources of our sample, mainly attending to the possible contribution from the WCR. In this way, we have found that such contribution may explain the observed differences in the spectral index (with respect to the standard $\alpha \sim 0.6$) by considering a non-thermal, optically thin thermal (partially absorbed or not), and/or optically thick thermal contributions. However, we cannot discard that other mechanisms occurring in a single star context could also be compatible with our

observational results.

The standard wind assumptions of isothermal, steady and spherical symmetric wind with a density profile $n \propto r^{-2}$, lead to the standard value of $\alpha \approx 0.6$ that characterizes the standard radio spectrum. Thus, it is expected that deviations in such assumptions result in deviations in α with respect to that standard value. Wrigth & Barlow (1975) and Schmid-Burgk (1982) investigated the consequences of a non-spherical symmetry over the spectrum. They concluded that changes (in particular higher values; see Section 1.2.1) in the spectral index are unlikely to result from stationary non-spherical winds. On the other hand, Leitherer & Roberts (1991) showed, based on the results of Wright & Barlow (1975) and Schmid-Burgk (1982), that for a power law dependence on the radial distance from the star (r) of the temperature ($T \propto r^{-\zeta}$), velocity ($v \propto r^{\beta}$), and ionization state ($Z \propto r^{-\epsilon}$; $\gamma \propto r^{-\eta}$; such that $\delta \geq 0$,$\beta \geq 0$, $\epsilon \geq 0$, and $\eta \geq 0$), the spectral index takes the value

$$\alpha = \frac{-0.6\zeta + 4\beta + 4\epsilon + 2\eta + 1.8}{-1.35\zeta + 2\beta + 2\epsilon + \eta + 3}. \tag{3.6}$$

Note that this equation contains the $\alpha = 0.6$ when $\zeta = \beta = \epsilon = \eta = 0$. This equation implies that an an increase in the velocity or any decrease of the temperature and ionization state will steepen the radio spectrum. From their analysis they concluded that acceleration/deceleration zones and changes in the ionized state at the radio emitting region could explain the observed deviations in the spectral indices.

For WR stars, the stellar wind is expected to reach its terminal velocity at distances $< 10\ R_\star$ (of the order of 10^{11} cm), which is two orders of magnitude smaller than the size of the emitting region at 250 GHz (of the order of 10^{13} cm, and even larger at 4.8 GHz). Thus, the acceleration zone is well within the optically thick region of the WR wind at our observing frequencies; hence, we can discard any effect from it on the spectrum inferred from our observations. On the other hand, temperature gradients only weakly affect the flux through the gaunt factor; thus, this effect is unable to explain the difference between standard and observed spectral indices (Pittard 2010). However, changes in the ionization state are more difficult to be discarded, since the ionization structure in WR stars is difficult to state (Nugis 2000). Moreover, clumpy wind models with shocks (at 30-100 stellar radii) producing a higher ionization zone in the outer wind seems to result in an steepening of the spectrum towards high frequencies (Nugis et al. 1998). Clumps and structures favoring this situation have been observed for some WR stars (e.g. Charepashchuk et al. 1984, Prinja et al. 2001); however, there is not direct evidence of its effect over the radio emitting regions. Thus, a clumpy wind, changing the state of ionization could be an alternative explanation for the steepening of the spectrum towards high frequencies observed for WR 98, and 139. We, however, discharge this as the reason of the steepening of the centimeter spectrum of WR79a, 98a, 104, 105, 113, and 141, since for clumpy winds we cannot explain the change to a standard spectrum observed at millimeter wavelengths (see Nugis et al. 1998).

On the other hand, variability in the wind parameters ($\dot{M}$ and v_∞), in contrast with the steady assumption, may result in internal shock structures affecting the resulting spectrum (González & Cantó 2008). Early studies of Abbott et al. (1981) showed that clumps and

structures distributed uniformly will not alter the resulting shape of the spectrum. However, high density regions occupying an small fraction of the volume may produce a noticeably effect. These studies were applied to P Cygni, which is a well known variable star in an untestable state of evolution (LBV) from which strong wind variability has been observed. Such strong variability is not expected in WR stars (Lamers 1988). Thus, although variability in the wind parameters of WR stars has been found to result in internal structures (Robert 1994), there are not detailed studies regarding the radial evolution of such structures to the radio emitting region of WR stars.

Finally, flat (and even negative) spectral indices could be also the result from a fall in the density profile with $\delta < 2$ ($n \propto r^{-\delta}$; see Section 1.2.1). However, the variability observed in the sources classified as NT and T/NT support our conclusion of a WCR contribution. Thus, for WR 98, although the millimeter spectrum could alternatively be explained in a single star context, the centimeter spectrum is more likely to result from a WCR effect.

3.6 Conclusions

The impact of the processes that may affect the spectrum of Colliding Wind Binaries (CWBs) is expected to be different depending on the wavelength range observed. In this way, the comparison between the spectrum at millimeter wavelengths with that extrapolated from centimeter wavelengths, allows to properly characterize their spectra and discern between the different contributions and effects that may have an impact over it. In particular, for close binary systems, this kind of analysis are specially necessary, since an additional thermal component of emission from the WCR is expected to contribute to the total spectrum. Furthermore, the non-thermal contribution in such close systems has been assumed to be completely absorbed, discarding its influence over the observed spectrum. On the other hand, for long period ones the non-thermal contribution can be important, being more relevant than the thermal contribution.

Our observational study includes a total of 14 WR stars, from which we have characterized 12 of them at centimeter and nine at millimeter. From the spectral characterization at the two wavelength ranges, and by the comparison between the millimeter and the centimeter spectral indices, we have found different kind of spectra:

- Stars with a standard thermal wind spectrum, at least at one observing epoch (WR 89, 133, and 135).
- Stars with hints of an excess of emission at millimeter wavelengths, probably resulting from a optically thick thermal contribution from a WCR (WR 98 and WR 139).
- Stars with negative or flat spectral indices at centimeter wavelengths, indicative of a non-thermal component of emission arising from the WCR (WR 8, 79a, 98, 105, 133, and 156).
- Stars for which the steep spectrum at centimeter, and the standard wind spectrum at millimeter, suggest the influence of a non-thermal component of emission partially absorbed at centimeter wavelengths (WR79a, 98a, 104, 105, 113, and 141).

In order to determine if the binary condition of the sources is able to affect their spectra, we have discussed the different kinds of spectra in a binary context. However, we can not rule out that besides the binary influence, instabilities in the wind parameters, clumps, and/or deviations from a standard wind could also affect the spectrum. Furthermore, since in such close systems it is unlikely to spatially resolve the WCR (as in the case of wide systems), the best way to unequivocally determine a WCR contribution, is through the relation between variability and orbital period, by sampling a light curve along a complete period, at least at one frequency.

We want to remark the importance of the millimeter observations for the spectral analysis. Such observations allowed us to reveal the presence of a partially absorbed non-thermal contribution at centimeter for WR 105, 113, and 141. These sources could be classified as thermal, owing to the positive spectral index at centimeter wavelengths; however, the millimeter observations revealed that such spectrum is also compatible with a non-thermal contribution partially absorbed at centimeter wavelengths. In this way, we have found that for such close systems, the influence of a non-thermal component is more likely to be present at intermediate frequencies ($\sim$ 4.8 to 23 GHz), in contrast with the case of wide binaries, for which the smaller effect of the stellar wind absorption makes easier to detect the non-thermal emission at lower frequencies. This high absorption is likely to be the reason for the non-detection of the sources observed at 1.4 GHz (WR 79a and WR 98). Furthermore, for some close systems, the optically thick thermal emission from a radiative WCR can be detected as an excess of emission at millimeter. In this way, even when the non-thermal emission could not be detected owing to the absorption at centimeter wavelengths, the influence of the binarity could be inferred from millimeter observations.

4

Conclusions

4.1 General Discussion and Conclusions

In this thesis, I have presented a study of the radio emission arising from stellar winds in Wolf-Rayet (WR) stars. The main goal of this work is to determine how the binary condition of a WR star may affect the radio and millimeter spectrum, specially in the case of close binary systems, where the non-thermal component from a wind-wind collision region (WCR), is expected to be completely absorbed. For this purpose we have performed observations of a sample of WR stars in a wide range of frequencies, from centimeter to millimeter wavelengths. We have compared our observations with those previously reported by other authors, in order to search for variability and/or to extend the wavelength coverage of our observations. We have also developed a semi-analytical model aimed to quantify the thermal contribution from a radiative wind-wind collision region (WCR) in binary systems.

The radio flux density of stellar winds is expected to grow with frequency with a standard spectral index $\alpha \approx 0.6$ ($S_\nu \propto \nu^\alpha$). At present, observational evidences of the presence of a binary companion have been mainly inferred by negative or flat ($\alpha \sim 0$) spectral indices at radio wavelengths, which are interpreted as the result of a non-thermal component of emission arising from the WCR. These studies have been very successful in the determination and constraint of stellar and binary parameters in wide systems. However, for close systems with orbital periods $P < 1$ year, the WCR is thought to lie within the optically thick region of the WR wind and, thus, to be absorbed. In this way, any effect of the binarity over the resulting radio spectrum would be lost in the case of close binary systems.

Ours and previous theoretical studies of the thermal emission from the WCR suggest that its contribution to the total spectrum may be significant, becoming even more important as the stars of the systems become closer. In an adiabatic WCR the hot material remains optically thin, and it is expected that it will contribute with a thermal component of emission with an spectral index ~ -0.1. Thus, the flux from an adiabatic WCR may dominate the thermal spectrum of the system, particularly at centimeter wavelengths. Furthermore, in this case the flux density is expected to scale with the binary separation as D^{-1}, becoming more important for closer systems. On the other hand, as the stars become closer, the cooling of the material within the

WCR is expected to become more important, changing from an adiabatic to a radiative WCR. In this regime, our model predicts a change in the WCR contribution, becoming optically thick with a spectral index ~ 1.1. Thus, a radiative WCR could also dominate the spectrum, this time at millimeter wavelengths. Moreover, our model predicts an increase of the emission with the binary separation, being the flux density scaled as $D^{4/5}$. Thus, our results suggest that for the case of radiative systems, it is possible to detect the WCR as an excess of emission at millimeter wavelengths with respect to the expected emission from the unshocked winds.

Our observational results suggest that a WCR could be contributing to the radio spectrum for at least nine of the total 14 WR stars observed in our sample. Seven of these nine stars are classified as binaries with orbital periods shorter than a few months. The influence of the WCR contribution has been inferred from three main characteristics in their spectra:

- *Stars with hints of an excess of emission at millimeter wavelengths (WR 98 and WR 139).* We found these systems to be close enough for the WCR to become highly radiative ($\chi < 1$). We consider that the observed excess of emission at millimeter wavelengths could be explained as the result of the thermal contribution from a radiative WCR. These cases can be considered as the observational evidence of the results we have obtained from our semi-analytical model.

- *Stars with negative or flat spectral indices at centimeter wavelengths (WR 8, 79a, 98, 105, 133, and 156).* This is usually interpreted as evidence of a non-thermal contribution from a WCR region. However, since WR 8, 98, 133, and 156 are close systems, the non-thermal emission from the WCR is unlikely to escape the strong absorption from the WR wind. We have discussed the possible scenario where an adiabatic thermal contribution from the WCR could result in the observed spectrum, and conclude that such scenario is implausible. In contrast, we suggest that non-thermal contribution could be escaping the absorption at least at certain orbital phases. For WR 98, this is supported by the variability observed at 4.8 GHz and by the low value of an upper limit for the flux density at 1 GHz, which suggests that the enhanced emission at 4.8 GHz would be strongly absorbed at this frequency. Nevertheless, more observations and a detailed modeling are required to corroborate the non-thermal nature of the radio spectra in these stars. For WR 105 and WR 79a, which are classified as single stars, this confirmation would strongly support the presence of a binary companion.

- *Stars with a steep spectrum at centimeter wavelengths ($\alpha > 0.6$), and a standard wind spectrum at millimeter wavelengths (WR 105, 113, and 141).* These spectra were interpreted as a result of a non-thermal contribution strongly diminished by the WR wind absorption at centimeter wavelengths. The standard wind spectrum found at millimeter wavelengths suggests that the maximum of such contribution occurs at intermediate wavelengths, between 20 and 50 GHz. A similar scenario has been proposed for WR 98a and 104 from the comparison of our centimeter observations with those presented by Monnier et al. (2002).

The observational evidences of a non-thermal contribution found in some close systems of our sample (WR 98, 133, and 156) seem to contradict the fact that the non-thermal emission would

be absorbed in systems with orbital periods $P < 1$ year. Evidence of non-thermal emission has been previously found in close WR systems (e.g. γ^2 Vel with $P = 78.5$ days; Chapman et al. 1999). An explanation could be that clumps in the wind would result in low opacity lines of sight through which the non-thermal emission could escape the absorption. Another possibility is that the relativistic particles flow along the contact discontinuity of the interacting region, allowing the non-thermal emission to reach lower opacity regions of the WR wind, being detectable at least at certain orbital phases (Dougherty & Williams, 2000). However, as already discussed by Pittard et al. (2006), a significant thermal contribution from an adiabatic WCR can result in a composite-like spectrum, often interpreted as evidence of a non-thermal contribution. Our estimations of the cooling parameter favor a radiative WCR, supporting the non-thermal nature of the spectrum. However, these estimates are strongly dependent on the stellar wind parameters and on the changes in the binary separation (as a consequence of an eccentric orbit); thus, and detailed models are required in order to discard an adiabatic WCR. Therefore, we cannot completely rule out that the possibility observed spectrum is the result from an optically thin thermal contribution from the WCR in WR 8, 98, 113, 133, 141 and 156.

The main general conclusions of our work can be summarized as follows:

- The WCR is able to have a significant effect on the radio spectra observed for WR stars, even for close binary systems with orbital periods < 1 year, where the absorption of the non-thermal emission was thought so far to avoid the effect of the binarity.
- The effect of the WCR in close WR binary stars could be detectable i) at centimeter wavelengths, from a non-thermal and/or an optically thin thermal contribution, and ii) at millimeter wavelengths, from an optically thick contribution detectable as an excess of emission. Furthermore, the strong absorption in these close systems, may translate the turn-over frequency of a possible non-thermal (or optically thin thermal) contribution to higher frequencies, compared to the case of wide systems where the non-thermal contributions is usually detected at frequencies $\lesssim 10$ GHz. Thus, in this case, it will be contributing only at intermediate frequencies, between 20 and 50 GHz (2 cm and 7 mm).
- In close systems, the WCR may affect the spectrum at different wavelength ranges, depending on the conditions of the shocks, and hence, on the nature of the emission resulting. This represents a more complex scenario for the case of close systems, in comparison with wide binaries, for which the effect of the binarity mainly results from the non-thermal emission, which mainly contributes at low frequencies ($\lesssim 10$ GHz).

We remark the importance of analyzing the spectrum of WR stars from observations at a wide range of frequencies, from centimeter to millimeter wavelengths. In this work, millimeter observations have allowed us to identify an excess of emission at these wavelengths with respect to that expected from the extrapolation of the centimeter spectrum. Furthermore, the comparison between millimeter and centimeter observations are also a tool to discover that, spectra previously classified as thermal (from their positive spectral index at centimeter wavelengths), are also compatible with non-thermal emission being partially absorbed at centimeter wavelengths.

4.2 Future Work

Finally, I remark the future work and prospects that thesis opens.

- I have discussed the spectrum characteristics in a binary context. However, I also pointed out that several factors occurring in a single star context could be also compatible with our observational results. On the other hand, for these close systems the WCR is unlikely to be spatially resolved. Thus, the best way to unambiguously confirm a WCR contribution is through a relation between variability and orbital period. This could be established by the full coverage of a radio light curve along an orbital period, at least at one observing frequency. In particular, this kind of studies could be performed at millimeter wavelengths through the detection of variable excess of emission from a radiative WCR. From our work, we find that WR 98 ($P \sim 48.7$ days) and WR 139 ($P \sim 4.2$ days) are excellent candidates for a future study aimed at testing this scenario.

- Most of WR stars are located at large distances ($\sim$ 2 kpc). Their emission is therefore usually faint ($\sim$ 1 mJy at centimeter wavelengths). The new generation of ultra-sensitive radio interferometers such as the Expanded VLA (EVLA), the upgrade of MERLIN (e-MERLIN), and the Atacama Large Millimeter/submillimeter Array (ALMA) are starting to become operative, providing an excellent platform to extend the work initiated in this thesis to a large sample of WR stars from which statistically meaningful results can be obtained.

- The semi-analytic model presented in this thesis allows to determine whether a radiative WCR contributes to the total radio spectrum of a binary system of not. It is necessary to extend this theoretical study to hydrodynamic simulations in order to include several features that are expected to be relevant in close systems. The inclusion of the acceleration region of the winds, and the orbital motion of the stars, are particularly important in such close systems where a radiative WCR is likely to occur. Furthermore, the inclusion of the orbital motion will also allow to determine the spectrum at several orbital phases, and analyze the variability resulting from the orbital motion.

5

List of Publications

The work presented in this Thesis has originated the following publications:

- *The Nature of the Radio Emission in Close Wolf-Rayet Binaries*
  Montes, G., Pérez-Torres, M.A., Alberdi, A. & González, R.F., in preparation

- *A model for the thermal radio-continuum emission from radiative shocks in colliding stellar winds*
  Montes, G., González, R.F., Cantó, J., Pérez-Torres, M.A., Alberdi, A.
  Astronomy & Astrophysics, 531, 52 (2011)

- *Thermal Radio Emission from Radiative Shocks in Colliding Stellar Winds*
  Montes, G., González, R.F., Cantó, J., Pérez-Torres, M.A., Alberdi, A.
  Société Royale des Sciences de Liège, Bulletin, 80, 704-708 (2010)

- *Disentangling the Nature of the Radio Emission in Wolf-Rayet Stars*
  Montes, G., Pérez-Torres, M.A., Alberdi, A., González, R.F.
  The Astrophysical Journal, 705, 899-906 (2009)

Other publications related to the Thesis work:

- *The Radio Counterparts to the Binary O4+O4 System CEN 1 in NGC 6618, the Cluster Ionizing M17*
  Rodríguez, L.F., González, R.F., **Montes, G.**
  Revista Mexicana de Astronomía y Astrofísica, 45, 273-277 (2009)

Bibliography

Abbott, D. C., Beiging, J. H., Churchwell, E., & Torres, A. V. 1986, ApJ, 303, 239

Altenhoff, W. J., Thum, C., & Wendker, H. J. 1994, A&A, 281, 161

Annuk, K. 1990, Acta Astronomica, 40, 267

Antokhin, I. I., Owocki, S. P., & Brown, J. C. 2004, ApJ, 611, 434

Barlow, M. J. 1979, Mass Loss and Evolution of O-Type Stars, 83, 119

Barniske, A., Hamann, W.-R., & Gräfener, G. 2006, Stellar Evolution at Low Metallicity: Mass Loss, Explosions, Cosmology, 353, 243

Becker, R. H., & White, R. L. 1985, ApJ, 297, 649

Bieging, J. H., Abbott, D. C., & Churchwell, E. B. 1982, ApJ, 263, 207

Bieging, J. H., Abbott, D. C., & Churchwell, E. B. 1989, ApJ, 340, 518

Bohannan, B., & Crowther, P. A. 1999, ApJ, 511, 374

Cantó, J., Raga, A. C., & Wilkin, F. P. 1996, ApJ, 469, 729

Cantó, J., Raga, A. C., & González, R. 2005, Revista Mexicana de Astronomia y Astrofisica, 41, 101

Cappa, C., Goss, W. M., & van der Hucht, K. A. 2004, AJ, 127, 2885

Castor, J. I., Abbott, D. C., & Klein, R. I. 1975, ApJ, 195, 157

Chapman, J. M., Leitherer, C., Koribalski, B., Bouter, R., & Storey, M. 1999, ApJ, 518, 890

Cherepashchuk, A. M. 1976, Soviet Astronomy Letters, 2, 138

Cranmer, S. R., & Owocki, S. P. 1994, Bulletin of the American Astronomical Society, 26, 1446

Conti, P. S. 1976, Memoires of the Societe Royale des Sciences de Liege, 9, 193

Contreras, M. E., Rodríguez, L. F., Gómez, Y., & Velázquez, A. 1996, ApJ, 469, 329

Contreras, M. E., Montes, G., & Wilkin, F. P. 2004, RMxAA, 40, 53

Corcoran, M. F., Stevens, I. R., Pollock, A. M. T., et al. 1996, ApJ, 464, 434

Crowther, P. A., Smith, L. J., & Willis, A. J. 1995, A&A, 304, 269

Crowther, P. A., Dessart, L., Hillier, D. J., Abbott, J. B., & Fullerton, A. W. 2002, A&A, 392, 653

Crowther, P. A., Hadfield, L. J., Clark, J. S., Negueruela, I., & Vacca, W. D. 2006, MNRAS, 372, 1407

Crowther, P. A. 2007, ARA&A, 45, 177

De Becker, M. 2007, A&A Rev., 14, 171

Dickel, H. R., Habing, H. J., & Isaacman, R. 1980, ApJ, 238, L39

De Becker, M., & Rauw, G. 2007, Massive Stars in Interactive Binaries, 367, 207

Dougherty, S. M., & Williams, P. M. 2000, MNRAS, 319, 1005

Dougherty, S. M., Williams, P. M., & Pollacco, D. L. 2000, MNRAS, 316, 143

Dougherty, S. M., Pittard, J. M., Kasian, L., Coker, R. F., Williams, P. M., & Lloyd, H. M. 2003, A&A, 409, 217

Dougherty, S. M., Beasley, A. J., Claussen, M. J., Zauderer, B. A., & Bolingbroke, N. J. 2005, ApJ, 623, 447

Eenens, P. R. J., & Williams, P. M. 1994, MNRAS, 269, 1082

Eichler, D., & Usov, V. 1993, ApJ, 402, 271

Florkowski, D. R. 1982, Wolf-Rayet Stars: Observations, Physics, Evolution, 99, 63

Gamen, R. C., & Niemela, V. S. 2002, New Astronomy, 7, 511

Gayley, K. G., Owocki, S. P., & Cranmer, S. R. 1997, ApJ, 475, 786

Gehrz, R. D., & Hackwell, J. A. 1974, ApJ, 194, 619

Georgiev, L. N., & Koenigsberger, G. 2004, A&A, 423, 267

González, R. F., & Cantó, J. 2008, A&A, 477, 373

Hamann, W.-R., Gräfener, G., & Liermann, A. 2006, A&A, 457, 1015

Henley, D. B., Stevens, I. R., & Pittard, J. M. 2005, MNRAS, 356, 1308

Herald, J. E., Hillier, D. J., & Schulte-Ladbeck, R. E. 2001, ApJ, 548, 932

Hjellming, R., Blankenship, L. C., & Balick, B. 1973, Nature, 242, 84

Hirv, A., Annuk, K., Eenmäe, T., et al. 2006, Baltic Astronomy, 15, 405

Hogg, D. E. 1982, Wolf-Rayet Stars: Observations, Physics, Evolution, 99, 221

Hogg, D. E. 1984, BAAS, 16, 522

Hogg, D. E. 1985, Radio Stars, 116, 117

1999, Irish Astronomical Journal, 26, 171

Kenny, H. T., & Taylor, A. R. 2005, ApJ, 619, 527

Lamontagne, R., Moffat, A. F. J., Drissen, L., Robert, C., & Matthews, J. M. 1996, AJ, 112, 2227

Leitherer, C., & Robert, C. 1991, ApJ, 377, 629

Leitherer, C., Chapman, J. M., & Koribalski, B. 1995, ApJ, 450, 289

Leitherer, C., Chapman, J. M., & Koribalski, B. 1997, ApJ, 481, 898

Lépine, S., Moffat, A. F. J., St-Louis, N., et al. 2000, AJ, 120, 3201

Luo, D., McCray, R., & Mac Low, M.-M. 1990, ApJ, 362, 267

Kallrath, J. 1991, MNRAS, 248, 653

Kurosawa, R., Hillier, D. J., & Pittard, J. M. 2002, A&A, 388, 957

Niemela, V. S., Morrell, N. I., Barba, R. H., & Bosch, G. L. 1996, Revista Mexicana de Astronomia y Astrofisica Conference Series, 5, 100

Niemela, V. S. 1991, Wolf-Rayet Stars and Interrelations with Other Massive Stars in Galaxies, 143, 201

Niemela, V. S., Gamen, R., Morrell, N. I., & Giménez Benítez, S. 1999, Wolf-Rayet Phenomena in Massive Stars and Starburst Galaxies, 193, 26

Nugis, T., Crowther, P. A., & Willis, A. J. 1998, A&A, 333, 956

Madura, T. I. 2010, Ph.D. Thesis, University of Delaware

Maeda, Y., Koyama, K., Murakami, H., et al. 1998, The Hot Universe, 188, 352

Marchenko, S. V., Moffat, A. F. J., & Eenens, P. R. J. 1998, PASP, 110, 1416

Mason, B. D., Gies, D. R., Hartkopf, W. I., et al. 1998, AJ, 115, 821

Moffat, A. F. J., Drissen, L., Lamontagne, R., & Robert, C. 1988, ApJ, 334, 1038

Monnier, J. D., Tuthill, P. G., & Danchi, W. C. 1999, ApJ, 525, L97

Monnier, J. D., Greenhill, L. J., Tuthill, P. G., & Danchi, W. C. 2002, ApJ, 566, 399

Montes, G., Pérez-Torres, M. A., Alberdi, A., & González, R. F. 2009, ApJ, 705, 899

Montes, G., González, R. F., Cantó, J., Pérez-Torres, M. A., & Alberdi, A. 2011, A&A, 531, A52

Moran, J. P., Davis, R. J., Spencer, R. E., Bode, M. F., & Taylor, A. R. 1989, Nature, 340, 449

Oskinova, L. M. 2005, MNRAS, 361, 679

Owocki, S. 2004, in Evolution of Massive Stars, Mass Loss and Winds (Edited by M. Heydari-Malayeri, Ph. Stee and J.-P. Zahn), 163-250

Panagia, N., & Felli, M. 1975, A&A, 39, 1

Parkin, E. R., & Pittard, J. M. 2008, MNRAS, 388, 1047

Pittard Ph.D. Thesis, The University of Birmingham

Pittard, J. M., Stevens, I. R., Corcoran, M. F., Gayley, K. G., Marchenko, S. V., & Rauw, G. 2000, MNRAS, 319, 137

Pittard, J. M., & Dougherty, S. M. 2006, MNRAS, 372, 801

Pittard, J. M., Dougherty, S. M., Coker, R. F., O'Connor, E., & Bolingbroke, N. J. 2006, A&A, 446, 1001

Pittard, J. M. 2009, MNRAS, 396, 1743

Pittard, J. M. 2010, MNRAS, 403, 1633

Prinja, R. K., Stahl, O., Kaufer, A., et al. 2001, A&A, 367, 891

Pollock, A. M. T. 1987, ApJ, 320, 283

Pollock, A. M. T., Corcoran, M. F., Stevens, I. R., & Williams, P. M. 2005, ApJ, 629, 482

Prilutskii, O. F., & Usov, V. V. 1976, Soviet Ast., 20, 2

Purton, C. R., Feldman, P. A., & Marsh, K. A. 1973, Nature, 245, 5

Rauw, G., Stevens, I. R., Pittard, J. M., & Corcoran, M. F. 2000, MNRAS, 316, 129

Rybicki, G. B., & Lightman, A. P. 1979, New York, Wiley-Interscience, 1979. 393 p.

Seaquist, E. R., & Gregory, P. C. 1973, Nature, 245, 85

Setia Gunawan, D. Y. A., Chapman, J. M., Stevens, I. R., Rauw, G., & Leitherer, C. 2003, A Massive Star Odyssey: From Main Sequence to Supernova, 212, 230

Shore, S. N., & Brown, D. N. 1988, ApJ, 334, 1021

St.-Louis, N., Willis, A. J., & Stevens, I. R. 1993, ApJ, 415, 298

Stevens, I. R., Blondin, J. M., & Pollock, A. M. T. 1992, ApJ, 386, 265

Stevens, I. R., & Pollock, A. M. T. 1994, MNRAS, 269, 226

Stevens, I. R. 1993, MNRAS, 265, 601

Stevens, I. R. 1995, MNRAS, 277, 163

Stevens, I. R., Corcoran, M. F., Willis, A. J., et al. 1996, MNRAS, 283, 589

Skinner, S. L., Nagase, F., Koyama, K., Maeda, Y., & Tsuboi, Y. 1995, Wolf-Rayet Stars: Binaries; Colliding Winds; Evolution, 163, 471

Skinner, S. L., Güdel, M., Schmutz, W., & Stevens, I. R. 2001, ApJ, 558, L113

Tuthill, P. G., Monnier, J. D., & Danchi, W. C. 1999, Nature, 398, 487

Tuthill, P. G., Monnier, J. D., Danchi, W. C., & Turner, N. H. 2003, A Massive Star Odyssey: From Main Sequence to Supernova, 212, 121

Tuthill, P. G., Monnier, J. D., Lawrance, N., et al. 2008, ApJ, 675, 698

Underhill, A. B., & Hill, G. M. 1994, ApJ, 432, 770

Usov, V. V. 1992, ApJ, 389, 635

van der Hucht, K. A. 2001, New Astronomy Review, 45, 135

Van Loo, 2005, Ph.D. Thesis, Royal Observatory of Belgium

van Loo, S., Runacres, M. C., & Blomme, R. 2006, A&A, 452, 1011

White, R. L. 1985, ApJ, 289, 698

Williams, P. M., van der Hucht, K. A., & The, P. S. 1987, A&A, 182, 91

Williams, P. M., van der Hucht, K. A., Pollock, A. M. T., Florkowski, D. R., van der Woerd, H., & Wamsteker, W. M. 1990, MNRAS, 243, 662

Williams, P. M., van der Hucht, K. A., Pollock, A. M. T., et al. 1990, MNRAS, 243, 662

Willis, A. J., Schild, H., & Stevens, I. R. 1995, A&A, 298, 549

Williams, P. M., Dougherty, S. M., Davis, R. J., van der Hucht, K. A., Bode, M. F., & Setia Gunawan, D. Y. A. 1997, MNRAS, 289, 10

Williams, P. M. 2008, Revista Mexicana de Astronomia y Astrofisica Conference Series, 33, 71

Wilkin, F. P. 1996, ApJ, 459, L31

Wilkin, F. P. 1997, Ph.D. Thesis, University of California, Berkeley

Wilkin, F. P. 2000, ApJ, 532, 400

Williams, P. M., Dougherty, S. M., Davis, R. J., van der Hucht, K. A., Bode, M. F., & Setia Gunawan, D. Y. A. 1997, MNRAS, 289, 10

Wright, A. E., & Barlow, M. J. 1975, MNRAS, 170, 41